Journal of Chemistry

Metal and Metal Oxide Nanomaterials for the Environment and Engineering Applications

Lead Guest Editor: BR Ramesh Bapu
Guest Editors: Palanisami Thavamani and Hak Yong Kim

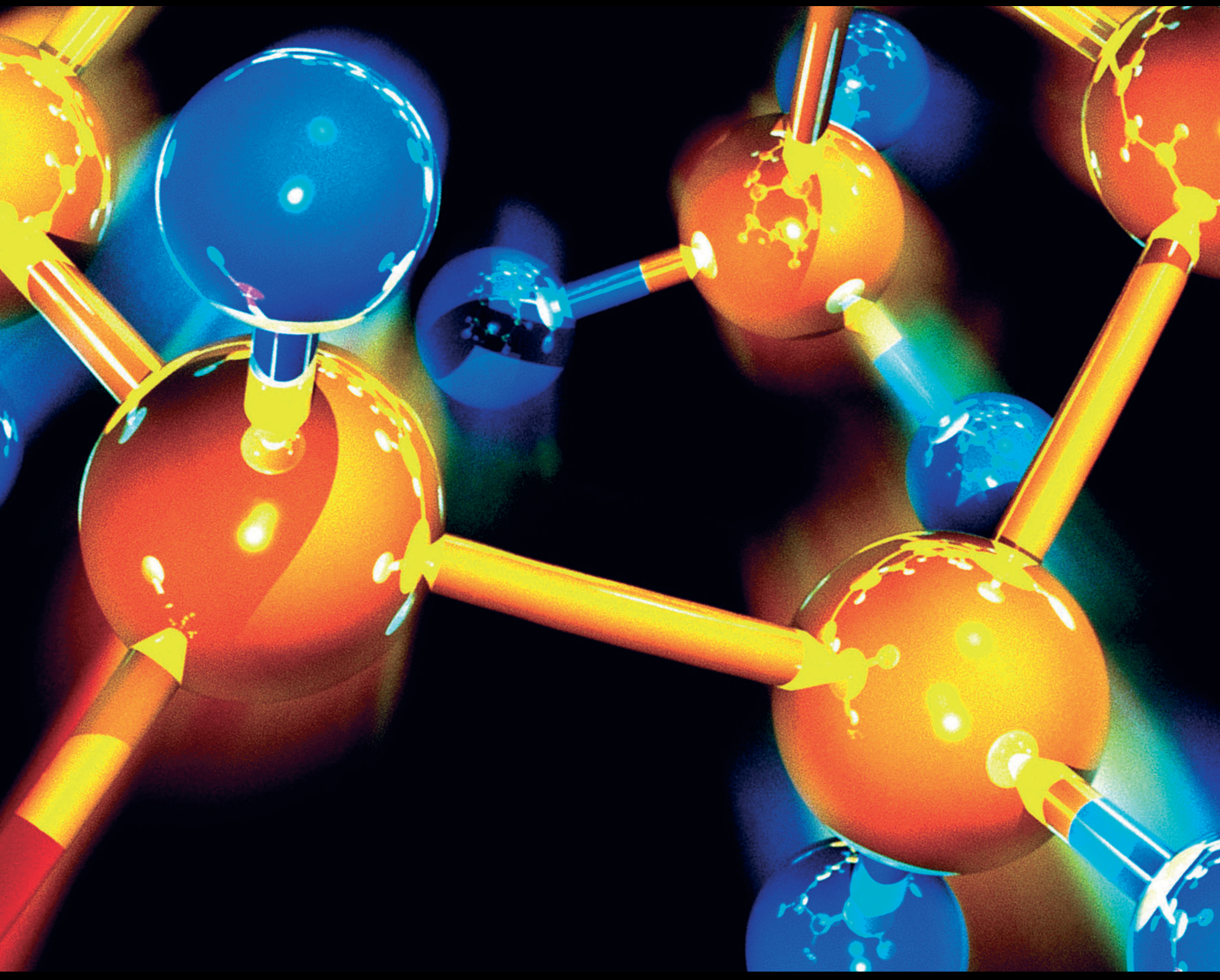

Metal and Metal Oxide Nanomaterials for the Environment and Engineering Applications

Journal of Chemistry

Metal and Metal Oxide Nanomaterials for the Environment and Engineering Applications

Lead Guest Editor: BR Ramesh Bapu
Guest Editors: Palanisami Thavamani and Hak Yong Kim

Contents

Bioconvection Flow in the Presence of Casson Nanoparticles on a Stretching/Shrinking Vertical Sheet with Chemical Reaction
B. Arun, M. Deivanayaki, and Selvakumar Kuppusamy Vaithilingam
Research Article (9 pages), Article ID 6199200, Volume 2023 (2023)

Investigation of the Wear Behavior of AA6063/Zirconium Oxide Nanocomposites Using Hybrid Machine Learning Algorithms
R. Reena Roy, Leninisha Shanmugam, A. Vinothini, Nirmala Venkatachalam, G. Sumathy, Bhavadharini Murugeshan, P. Mercy Rajaselvi Beaulah, and Gizachew Assefa Kerga
Research Article (16 pages), Article ID 7571588, Volume 2023 (2023)

Green Synthesis by Microwave Irradiation of TiO_2 Using *Cinnamomum verum* and the Application in Photocatalysis
Dante E. González-Anota, Silvia P. Paredes-Carrera, Rosa M. Pérez-Gutierrez, Brandon Arciniega-Caballero, Raul Borja-Urby, Jesús C. Sánchez-Ochoa, and Elizabeth Rojas-García
Research Article (17 pages), Article ID 2245685, Volume 2023 (2023)

Biologically Reduced Zinc Oxide Nanosheets Using *Phyllanthus emblica* Plant Extract for Antibacterial and Dye Degradation Studies
Awais Khalid, Pervaiz Ahmad, Mayeen Uddin Khandaker, Yosra Modafer, Hanadi A. Almukhlifi, Abdulrahman S. Bazaid, Abdu Aldarhami, Abdulaziz M. Alanazi, Ohoud A. Jefri, Md. Mohi Uddin, and Husam Qanash
Research Article (10 pages), Article ID 3971686, Volume 2023 (2023)

Study of Microstructure and Wear Resistance of AA5052/B_4C Nanocomposites as a Function of Volume Fraction Reinforcement to Particle Size Ratio by ANN
D. Dinesh Kumar, A. Balamurugan, K. C. Suresh, R. Suresh Kumar, N. Jayanthi, T. Ramakrishnan, S. K. Hasane Ahammad, S. Mayakannan, and S. Venkatesa Prabhu
Research Article (12 pages), Article ID 2554098, Volume 2023 (2023)

Hindawi
Journal of Chemistry
Volume 2023, Article ID 6199200, 9 pages
https://doi.org/10.1155/2023/6199200

Research Article

Bioconvection Flow in the Presence of Casson Nanoparticles on a Stretching/Shrinking Vertical Sheet with Chemical Reaction

B. Arun,[1] **M. Deivanayaki**,[2] **and Selvakumar Kuppusamy Vaithilingam**[3]

[1]*Department of Mathematics, Karpagam Academy of Higher Education, Coimbatore, Tamil Nadu, India*
[2]*Department of Science and Humanities, Karpagam Academy of Higher Education, Coimbatore, Tamilnadu, India*
[3]*Process, Energy and Environmental Engineering Chair, School of Chemical and Bioengineering, Dire Dawa University Institute of Technology, Dire Dawa University, Dire Dawa 1362, Ethiopia*

Correspondence should be addressed to Selvakumar Kuppusamy Vaithilingam; selvakumar.kuppusamy@ddu.edu.et

Received 3 November 2022; Revised 19 December 2022; Accepted 22 March 2023; Published 26 October 2023

Academic Editor: B. R. Ramesh Bapu

A Casson nanoparticle is used in this study to investigate the effects of toxic reactions, temperatures, and concentrations on convective heat transfer flow across a stretching/shrinking vertical sheet. The goal is to convert the control linear partial differential equations (PDEs) into an ordinary differential equations (ODEs) set and analyses them statistically using the Bvp4c technique in MATLAB software. It is necessary to look how various variables, such as the Casson nanofluid measurement, the chemical change constants and Prandtl numbers, the concentration-thermal-buoyancy ratio, the microorganism-to-thermal-buoyancy rate of return, the Lewis number, and other bioconvection-related parameters (such as the variation in micro-organism concentration and the buoyancy parameter), affect each other. The numerical results of the velocity, temperature, concentration, and bioconvection flow profiles are displayed.

1. Introduction

Due to various outstanding thermal conductivities, nanofluids are now used as working fluids instead of base fluids. Choi [1] was the first one to discover nanofluids, which are having a concentration of nanosized particles. According to Lee et al. [2], nanofluids have superior heat transmission properties as compared to basic fluids. Many industrial and technological applications exploit non-Newtonian nanofluids, such as embedded polymers, biological remedies, paints, asphalts, and glues. Nanofluids are manufactured by suspending nanoparticles which include nitrides, carbon nanotubes, and metal carbides in warm trading fluids; the lukewarm conductivity of these liquids is contingent on the sparkle trade coefficient between the vivacity trade intermediate and the sparkle trade shell. It is found that the non-Newtonian nanofluid has behaved differently on a vertical plate and truncated cone immersed in a porous media. The Casson fluid structure is a combination of non-Newtonian fluid involving applications in food encoding, smelting, excavating, and genetics. In order to mimic the flow properties of pigment oil suspensions, Casson created the Casson nanofluid flow in 1959 [3]. Studies of the Casson fluid or Casson nanofluid flowing in boundary layer thickness across different forms have been conducted by several authors [4–7]. Nanofluids may affect chemical processes, heat production, and MHD radiation across a stretched sheet, according to a number of researchers [8–10]. For many domains of management and innovation, chemical reaction effect is an essential consideration in the study of heat and mass mobility. A chemical reaction between the base liquid and nanoparticles can occur frequently either throughout a phase or at the phase's boundary. Afify [11] has revealed that in the presence of fluid motion and chain reaction, slip boundary conditions influence Casson nanofluid flow across a stretched plate. Bioconvection has demonstrated excellent prospects in the field of environmental sustainable and long-term fuel cell technology. The chemical sensitivity of magneto Casson nanofluids has been researched by Arun et al. [12].

Microorganisms are a generic description of organisms that are too tiny to be identified individually. Bacteria, yeast, viruses, protozoa, and green algae constitute characteristics of microorganisms. Microorganism colonies all ecological niches, in the unfavorable conditions such as engine fuel lines, coal mines, and hot springs where few other living things can persist. Bioconvection emerges when microorganisms migrate upstream in a fluid, culminating in instability and an amorphous pattern. The modular system of such systems required periodic computational geometry optimization in conjunction with laboratory and field testing. Kuznetsov and Avramenko [13] evaluated the bioconvection of gyrotactic microorganisms exploiting nanoparticles for the first time. Hill and Pedley [14] presented a research article on the hydrodynamics of bioconvection. According to Alloui et al. [15], the composition of gravitactic microbes in a cylinder is characterized. Using a dynamic stretching/shrinking sheet, Uddin et al. [16] have evaluated the Stefan blowing phenomena on bioconvection nanofluid flow. The spontaneous bioconvective flow of such a nanofluid containing gyrotactic microorganisms across a projected vertical plate is shown by Chamkha et al. [17]. Mallikarjuna et. al. [18] studied the combined bioconvective flow of nanofluid including gyrotactic microorganisms across a vertical and thin cylinder of nanofluid. The called peristalsis flow of non-Newtonian nanofluid further than the difference of the two infinite coaxial conduits containing swimming oxytactic microorganisms is studied by Abdelsalam and Bhatti [19]. The nondimensionalized governing partial differential equation model is constructed by calculating bioconvection flow and heat transfer in the porous annulus and performance capacity transformations. The results of this analysis demonstrate that after nondimensionalizing microbe guiding equations, the Peclet number initially increases. Ahmad et al. [20] evolved the nonlinear partial differential equations and converted them into dimensionless form using homotopic transformations. They were then analytically explained using the homotopic technique, and they came to the conclusion that the magnetic parameter is responsible for the transformation in both components of velocity. In the horizontal direction, the velocity tends to decrease while the bioconvected Rayleigh number and buoyancy ratio remain stable. It is also acknowledged that increasing the bioconvected Lewis and Peclet numbers results in a decrease in the dispersion of motile microorganisms, but the thermophoresis constant exhibits the opposite propensity.

The impact of major physical parameters discussed numerically in bioconvection flow was explained by Dhanai et al. [21] in their description of the numerical analysis of bioconvection boundary layer flow and heat transfer of electrically conducting nanofluid containing nanoparticles and gyrotactic microorganism over an inclined permeable sheet. The free convective heat transfer from a vertical plate in a porous media saturated with nanofluid under laminar circumstances was explained by Hady et al. [22] to the power-law non-Newtonian flow, and the effects of Brownian motion and thermophoresis are factored in the nanofluid model.

In the presence of bioconvection and chemical reaction effects, Shah et al. [23] illustrate method to quantify the heat transfer attributes of a magneto hydrodynamic Prandtl hybrid nanofluid covering a stretched surface. Across stretching sheets, this article evaluates the bioconvection, inclined magneto hydrodynamic radiations, thermal linear radiations, and chemical reaction of hybrid nanofluid. Additionally, the conclusions are contrasted with nanofluid flow. Also, emphasis is offered to the Prandtl fluid, a non-Newtonian fluid. A few illustrations of real-world implications for hybrid nanofluids encompass microfluidics, business, transportation, the military, and medicine.

The bioconvection effects in Walter's B nanofluid flow are currently explored by Alqarni [24] as a reaction of the stretchable surface, which culminates in important properties such as heat radiation, activation energy, motile microorganisms, and convective boundary restrictions. In graphical and tabular representations, the consequences of interesting parameters on the velocity field, heat field, species concentration, and microbe concentration are displayed. The present strategy is more practical in a variety of domains, including pharmaceutical delivery systems, recombinant proteins, synthetic biology, tissue engineering, and biofuel cells.

With swimming gyrotactic microorganisms in a conjugate mixed bioconvection flow of Carreaunanofluid via an inclined stretchable cylinder with variable magnetic field incidence and binary chemical reaction, Nabwey et al. [25] examine heat transmission. The assessment also considers nonuniform thermal conductivity and stochastic decrease or rise in the heat source. This nano-bioconvection flow example is estimated using a passively controlled nanofluid pattern, which is thought to be more physically accurate than the earlier actively controlled nanofluid typically used. The important discovery of the current study is that the activation energy constraint improves with increasing nanoparticle concentration in the nanofluid.

According to Dhlamini et al. [26], using nanofluids in place of traditional fluids and exploiting motile microorganisms are two methods for moderating the rates of heat and mass transmission. Activation energy, Brownian motion, and thermophoretic effects are only taken into account for the solute and not for the microorganisms in some recent studies of bioconvection flow. The dynamics of the microorganisms are extensively controlled by the activation energy, the thermophoretic force, and Brownian motion.

Different malignant cells can be completely cured with nanoparticles. The most similar therapeutic that sheds light in biomedical science is nanoparticles. Researchers have recently devoted a great deal of attention to the study of nanoparticles due to their structure, shape, low toxicity, and phenomenal compatibility with the human body. A special type of nanoparticle was used to obstruct and kill cancer

cells. The gold and Casson nanoparticles among them each had an intended role. Developed specifically nanoparticles were used to injure and kill cancer cells. The problem is tried to pick because it is motivated by this particular application.

2. Mathematical Formulation

Across a semi-infinite moving flat plate, a nanofluid flows in a stable boundary layer in a homogenous free stream. Normal to move, surface coordinates are used to measure the flow. Moreover, the fluid temperature and nanoparticle concentration in the flowing fluid would directly relate to the surface temperature and nanoparticle concentration. Schematic representation of the flow is represented in Figure 1.

The new systems of equations for bioconvection flow are then generated.

$$\frac{\partial u}{\partial x}+\frac{\partial v}{\partial y}=0, \tag{1}$$

$$\begin{aligned} u\frac{\partial u}{\partial x}+v\frac{\partial u}{\partial y} &= u_e\frac{\partial u_e}{\partial x}+\upsilon\left(1+\frac{1}{\beta}\right)\frac{\partial^2 u}{\partial y^2}+(\beta_T)(T-T_\infty)g \\ &\quad +(\beta_c)(C-C_\infty)g+(\beta_N)(N-N_\infty)g, \end{aligned} \tag{2}$$

$$u\frac{\partial T}{\partial x}+v\frac{\partial T}{\partial y}=\frac{k}{\rho c_p}\cdot\frac{\partial^2 T}{\partial y^2}+\left(1+\frac{1}{\beta}\right)\frac{\mu}{\rho c_p}\cdot\left(\frac{\partial u}{\partial y}\right)^2, \tag{3}$$

$$u\frac{\partial C}{\partial x}+v\frac{\partial C}{\partial y}=D_n\cdot\frac{\partial^2 C}{\partial y^2}-k_0(C-C_\infty), \tag{4}$$

$$u\frac{\partial N}{\partial x}+v\frac{\partial N}{\partial y}+\frac{bW_c}{\Delta C}\frac{\partial}{\partial y}\left(N\frac{\partial C}{\partial y}\right)=D_m\cdot\frac{\partial^2 N}{\partial y^2}, \tag{5}$$

where u is component velocity on the x-axis, v is along the y-axis component velocity, υ is kinematic viscosity, β_T is thermal expansion coefficient of temperature, β_c is thermal expansion coefficient of concentration of nanoparticles, β_N is thermal expansion coefficient of density of microorganism, g is buoyancy parameter, N is density motile of microorganism, N_∞ is constant ambient density of microorganism, k is thermal conductivity, (ρc_p) is heat capacity of nanofluid, β is Casson parameter, k_0 is chemical reaction of species with reaction rate constant, D_n is diffusivity of nanoparticles, D_m is diffusivity of microorganism, b is constant velocity of the plate, and W_c is maximum cell swimming speed.

The appropriate boundary conditions are applied to the governing equations (1)–(5):

$$\begin{aligned} &\left.\begin{aligned} v&=0\\ u&=u_w\\ T&=T_w\\ C&=C_w\\ N&=N_w \end{aligned}\right\}\text{at } y=0,\\ &\left.\begin{aligned} u&\longrightarrow u_e\\ T&\longrightarrow T_\infty\\ C&\longrightarrow C_\infty\\ N&\longrightarrow N_\infty \end{aligned}\right\}\text{as } y\longrightarrow\infty, \end{aligned} \tag{6}$$

where N_w is surface density of microorganism.

$$\left.\begin{aligned} u_w(x)&=be^{(x/L)}\\ T_w(x)&=T_\infty+T_0e^{(x/L)}\\ C_w(x)&=C_\infty+C_0e^{(x/L)}\\ N_w(x)&=N_\infty+N_0e^{(x/L)}\\ u_e(x)&=ae^{(x/L)} \end{aligned}\right\}. \tag{7}$$

Using the similarity transformation method, PDE governing equations are generated into ODEs. The followings are the similarity variables which are used as follows:

$$\begin{aligned} \eta &= \sqrt{\frac{a}{2\upsilon L}}be^{(x/2L)}y,\\ \psi &= \sqrt{2a\upsilon L}e^{(x/2L)}f(\eta),\\ u &= ae^{(x/L)}f'(\eta),\\ v &= -\sqrt{\frac{\upsilon a}{2L}}be^{(x/2L)}\left[f(\eta)+\eta f'(\eta)\right],\\ \theta(\eta) &= \frac{T-T_\infty}{T_w-T_\infty};\quad \text{where } T=\theta(\eta)T_0e^{(2x/L)}+T_\infty,\\ \phi(\eta) &= \frac{C-C_\infty}{C_w-C_\infty};\quad \text{where } C=\phi(\eta)C_0e^{(2x/L)}+C_\infty,\\ X(\eta) &= \frac{N-N_\infty}{N_w-N_\infty};\quad \text{where } N=X(\eta)N_0e^{(2x/L)}+N_\infty, \end{aligned} \tag{8}$$

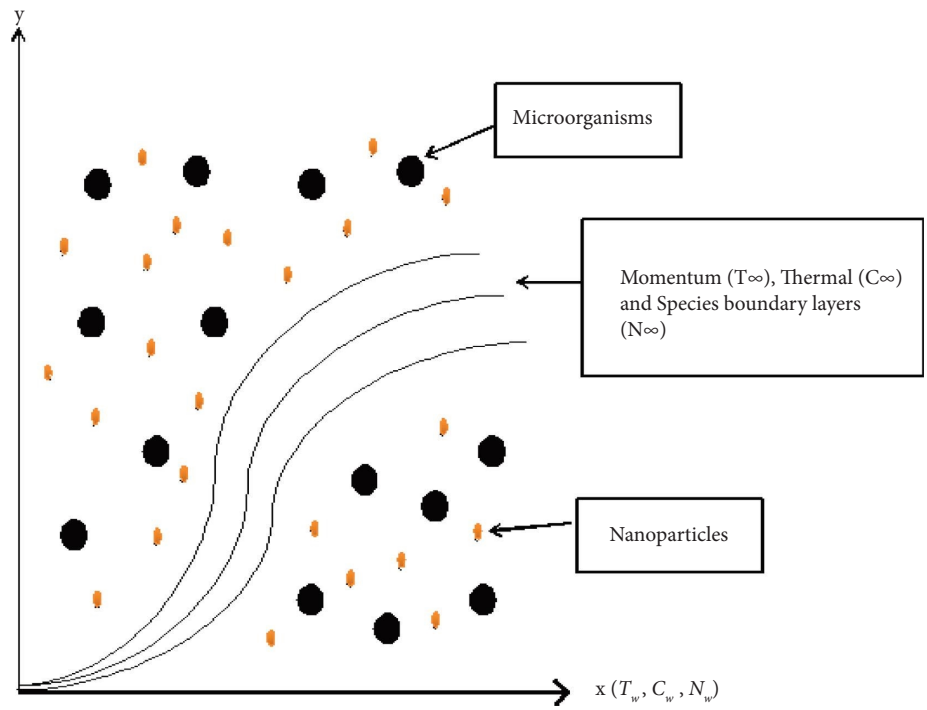

Figure 1: Characteristics of the problem.

where η is similarity variable, with $u = (\partial\psi/\partial y)$ and $v = -(\partial\psi/\partial x)$ symbolizes the stream function, ψ, θ is dimensionless temperature, L is sheet's characteristic length, ϕ is dimensionless nanoparticle fractional function, X is dimensionless microorganisms fractional function, a is constant velocity of stagnation flow, T_0 is constant velocity of temperature, C_0 is constant velocity of concentration, and N_0 is constant velocity of microorganism.

The PDEs are turned into ODEs as follows using the similarity transformation variables:

$$\left(1+\frac{1}{\beta}\right)f'''(\eta)+f(\eta)f''(\eta)-2\left(f'(\eta)\right)^2+2+2\lambda\left(\theta(\eta)+\phi(\eta)N_c+X(\eta)N_N\right)=0, \tag{9}$$

$$4f'(\eta)\theta(\eta)-f(\eta)\theta'(\eta)-\frac{\theta''(\eta)}{P_r}-\left(1+\frac{1}{\beta}\right)E_c\left(f''(\eta)\right)^2=0, \tag{10}$$

$$4f'(\eta)\phi(\eta)-f(\eta)\phi'(\eta)-\frac{1}{L_eP_r}\phi''(\eta)+K=0, \tag{11}$$

$$4f'(\eta)X(\eta)-f(\eta)X'(\eta)-\frac{P_e}{L_bP_r}\left(\phi''(\eta)X(\eta)+\Omega\phi''(\eta)+.X'(\eta)\phi'(\eta)\right)-\frac{1}{L_bP_r}X''(\eta)=0. \tag{12}$$

In contrast to the boundary constraints,

$$\begin{aligned} f(\eta) &= 0, \\ f'(\eta) &= \varepsilon, \\ \theta(\eta) &= 1, \\ \phi(\eta) &= 1, \\ X(\eta) &= 1 \text{ at } \eta = 0, \end{aligned} \tag{13}$$

$$\begin{aligned} f'(\eta) &= 1, \\ \theta(\eta) &= 0, \\ \phi(\eta) &= 0, \\ X(\eta) &= 0 \text{ as } \eta \longrightarrow \infty, \end{aligned} \tag{14}$$

where $\lambda = (g\beta T_0 L/a^2)$ is mixed convection parameter, $P_r = (\mu C_p/k) = (\upsilon/\alpha)$ is Prandtl number, $L_e = (\alpha/D_n)$ is Lewis number, $P_e = (bW_c/D_m)$ is bioconvection Peclet number, $L_b = (\alpha/D_m)$ is bioconvection Lewis number, $\Omega = (N_\infty/N_w - N_\infty)$ is microorganisms concentration difference parameter, $N_c = (C_0/T_0)$ is concentration to thermal buoyancy ratio parameter, $N_N = (N_0/T_0)$ is microorganism to thermal buoyancy ratio parameter, $E_c = (a^2/C_P T_0)$ is Eckert number, $K = (2k_0 L/a)$ is chemical reaction parameter, and ε is the stretching/shrinking parameter.

3. Results and Discussions

As it is much more feasible in many engineering applications, this study uses a specific BVP to estimate numerical solutions. The governing equations in this analysis are reduced to nonlinear ODEs and numerically solved using MATLAB's bvp4c mathematical solver. MATLAB's bvp4c is used to solve a system of nonlinear ODEs (9) to (12) having boundary conditions (13) and (14).

The obtained results are validated with the already existing results. The validation for physical parameters is given in following Table 1. Numerical values of $-\theta'(0)$ and $-\phi'(0)$ with E_c for $P_r = 4, L_e = 5, P_e = 1, L_b = 1, N_c = 0.1, N_N = 0.1, K = 1,$ and $\Omega = 0.2$.

The values obtained are in good agreement with the already existing work. This shows that the problem is well defined and the formulation of the problem is perfect.

Figure 2 depicts the impression of β on velocity profile, where the velocity profiles decrease for the rising values of β. So the fluid parameter has created on retarding force. This force elevates the viscosity of the fluid despite slowing rapid velocity. The influence β on temperature profile is polled in Figure 3. It is found from Figure 3 that the temperature reduces with an increase in β. Figure 4 depicts the effect of β on concentration profile. It can sight that the concentration decreases in $0 \le \eta \le 0.5$ and increases in $0.5 \le \eta \le 4$ for increasing values of β. Figure 5 illustrates the effect of β on bioconvection flow profile. The profile accelerates for increasing values of β. It is found from Figure 6 that the temperature profile is impeding with an increasing value in E_c. It is noticed from Figure 7 that the concentration profile increases with an increase in K. It is observed from Figure 8 that the concentration distribution amplifies with an increase in L_e. It is found from Figure 9 that the bioconvection flow profile decreases with an increase in L_b.

The bioconvection Peclet number P_e and cell swimming speed W_c are directly proportional with each other and inversely proportional to D_n (microorganism's diffusivity). The bioconvection Peclet number modulates the rates of advection and diffusion. Therefore, a rise in the amount of adventive transport leads to a higher bioconvection Peclet number, which in turn makes the flux of microorganisms to increase quickly. As a response, peak intensity of the bioconvection Peclet number degrades the profile of motile microbe density while increasing the flux of wall motile

Table 1: Comparison of results for $-\theta'(0)$ and $-\phi'(0)$.

E_c	Afify [11]		Present results	
	$-\theta'(0)$	$-\phi'(0)$	$-\theta'(0)$	$-\phi'(0)$
0.2	0.655854	1.19213	0.655882	1.19311
0	0.795783	1.113521	0.795698	1.113421
1	0.082093	1.515737	0.082088	1.515682
1.3	−0.139103	1.641030	−0.139179	1.641082

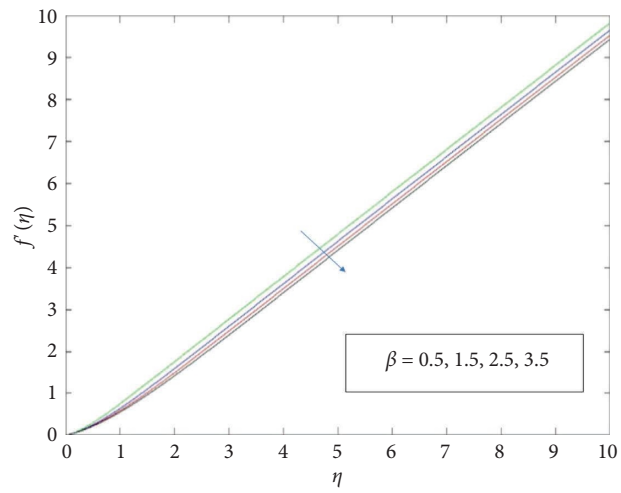

Figure 2: Effect of Casson fluid parameter on velocity profile.

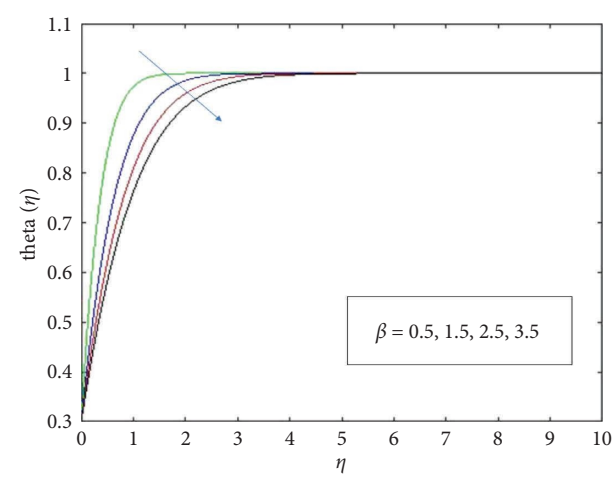

Figure 3: Effect of Casson fluid parameter on temperature profile.

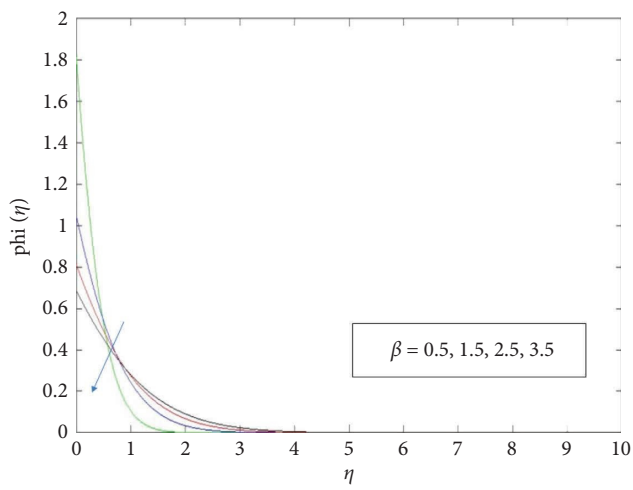

Figure 4: Concentration profile as a function of Casson fluid component.

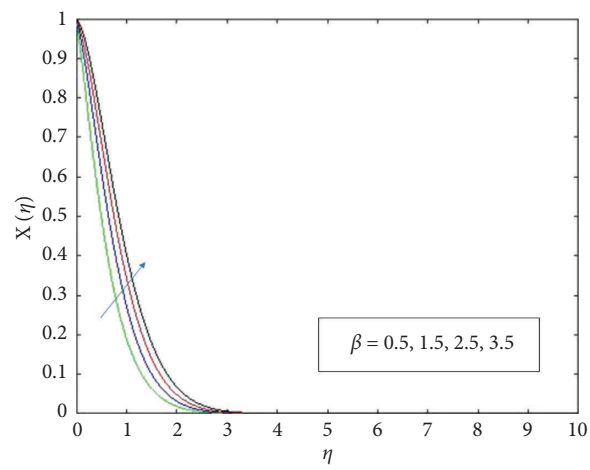

Figure 5: Bioconvection flow profile and the Casson fluid parameter.

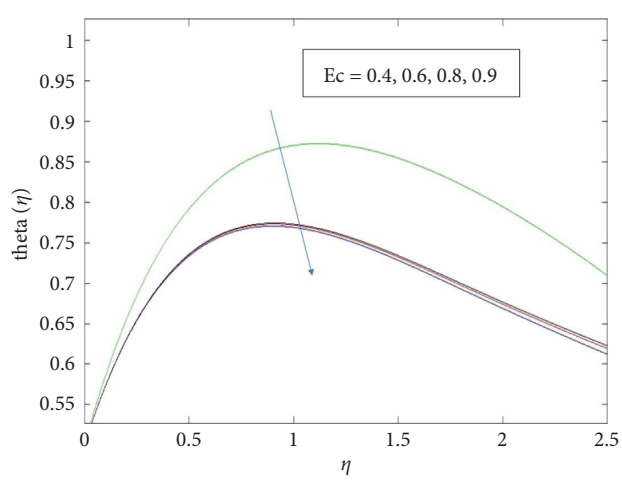

Figure 6: Temperature rise or fall depending on Eckert number.

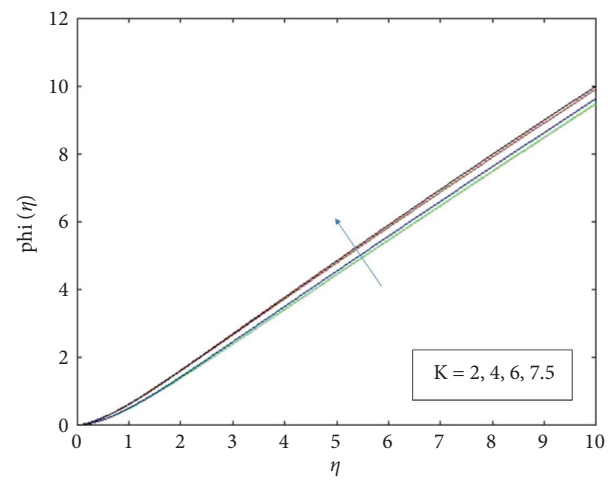

Figure 7: On the concentration profile of the chemical reaction parameter.

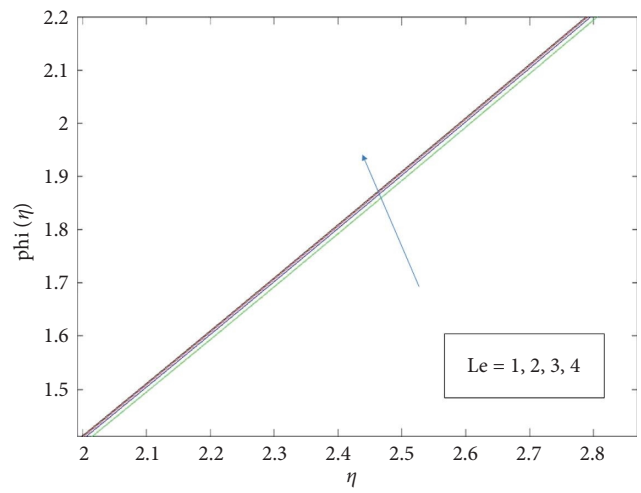

Figure 8: Concentration profile as a result of Lewis number.

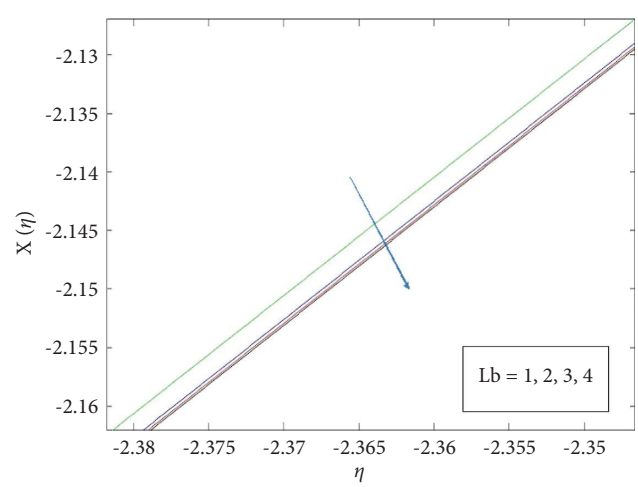

Figure 9: Effects of the bioconvection Lewis number on the bioconvection flow profiling.

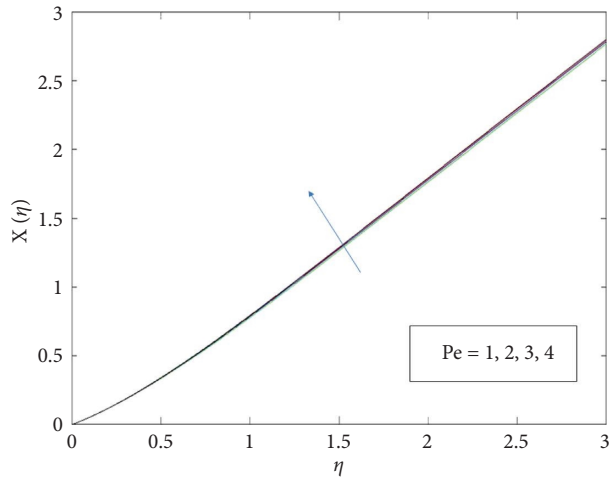

Figure 10: Bioconvection Peclet count affects flow profile.

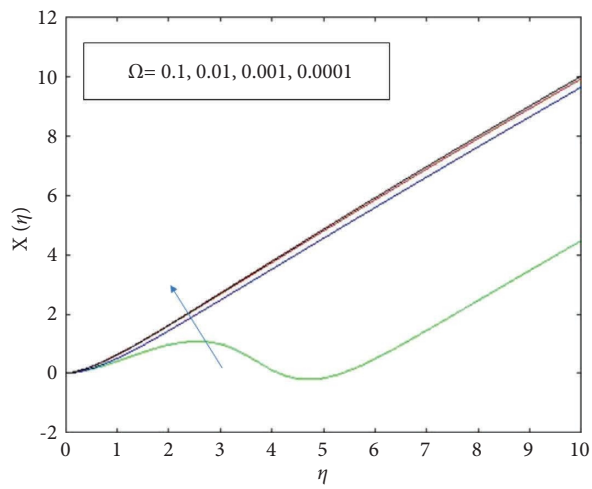

Figure 11: Bioconvection flow profile is affected by differences in the concentration of microorganisms.

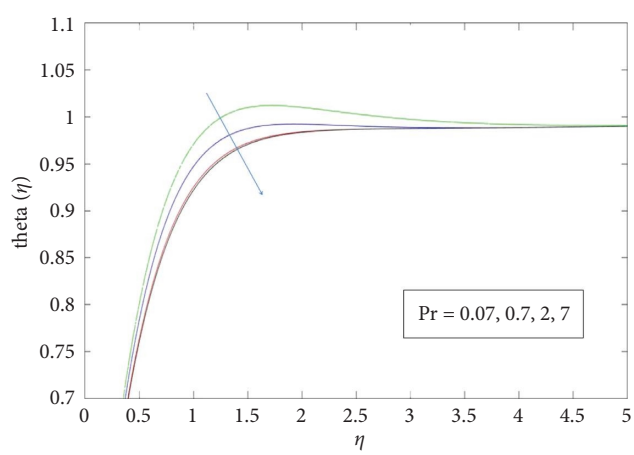

Figure 12: Prandtl number's influence on the temperature profile.

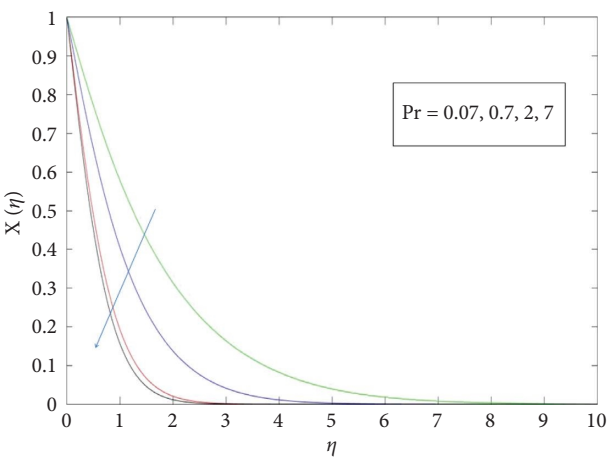

Figure 13: Prandtl number's significance on the bioconvection flow profile.

bacteria. The motile bacteria density profile degrades, and the flux of motile microorganisms on the wall increases as the bioconvection Peclet number values increase. Figure 10 elucidates the influence of P_e on bioconvection flow profile. The bioconvection flow profile amplifies with an increase in P_e. Figure 11 reflects the extent of said microorganism concentration discrepancy parameter on the bioconvection flow profile. Bioconvection flow profile is seen to improve with a decrease in Ω.

The Prandtl number is a dimensionless quantity that relates a fluid's viscosity to its thermal conductivity (Pr). Pr is the product of diffusivity and thermal conductivity. Consequently, a larger diffusivity is triggered by a higher Prandtl number, but the highest thermal diffusivity is characterized by a lower Prandtl value. Both the temperature and the thickness of the boundary layer tend to decrease due to this mechanism. Therefore, it is dependent solely on the fluid and is not dependent on the geometry of an object that is causing the issue. The Prandtl number is a trait of the fluid itself; hence, it has no bearing on the prevalence of bacteria in the flow. It is observed from Figure 12 that the temperature distribution amplifies with an increase in Prandtl number. It is found from Figure 13 that the bioconvection flow profile decreases with an increase in Prandtl number.

4. Conclusions

Over a stretching/shrinking vertical sheet, the influence of chemical reaction, temperature, and concentration in the presence of Casson nanoparticles in bioconvection flow is examined. The similarity transformation technique is being used to determine the concerns that have been resulted. From the results and discussion, it is clear that velocity profile decreases with increase in β. The effect of β and E_c decreases the temperature profile in both cases. The concentration profile increases with increasing values of β, K, and L_e. It is observed that bioconvection flow profile is enhanced with increase of β and decrease with increase of L_b, P_e, P_r, and Ω.

Data Availability

The data used to support the findings of the study are available from the corresponding author upon request.

Conflicts of Interest

The authors declare that they have no conflicts of interest.

References

[1] S. U. S. Choi, "Enhancing thermal conductivity of fluids with nanoparticles," in *Proceedings of the 1995 ASME International Mechanical Engineering Congress and Exposition*, pp. 99–105, San Francisco, CA, USA, October, 1995.

[2] S. Lee, S. U. S. Choi, S. Li, and J. A. Eastman, "Measuring thermal conductivity of fluids containing oxide nanoparticles," *Journal of Heat Transfer*, vol. 121, no. 2, pp. 280–289, 1999.

[3] N. Casson, *Reheology of Dispersed System*, Peragamon Press, Oxford, UK, 1959.

[4] T. Hayat, S. Asad, and A. Alsaedi, "Flow of Casson fluid with nanoparticles," *Applied Mathematics and Mechanics*, vol. 37, no. 4, pp. 459–470, 2016.

[5] G. Makanda, S. Shaw, and P. Sibanda, "Diffusion of chemically reactive species in Casson fluid flow over an unsteady stretching surface in porous medium in the presence of a magnetic field," *Mathematical Problems in Engineering*, vol. 2015, Article ID 724596, 10 pages, 2015.

[6] M. Mustafa, T. Hayat, I. Pop, and A. Aziz, "Unsteady boundary layer flow of a Casson fluid due to an impulsively started moving flat plate," *Heat Transfer - Asian Research*, vol. 40, no. 6, pp. 563–576, 2011.

[7] S. Nadeem, R. Mehmood, and N. S. Akbar, "Optimized analytical solution for oblique flow of a Casson nanofluid with convective boundary conditions," *International Journal of Thermal Sciences*, vol. 78, pp. 90–100, 2014.

[8] M. Abd El-Aziz, "Effect of time-dependent chemical reaction on stagnation point flow and heat transfer over a stretching sheet in a nanofluid," *Physica Scripta*, vol. 89, no. 8, Article ID 85205, 2014.

[9] K. Das, P. R. Duari, and P. K. Kundu, "Numerical simulation of nanofluid flow with convective boundary condition," *Journal of the Egyptian Mathematical Society*, vol. 23, no. 2, pp. 435–439, 2015.

[10] N. T. M. El-Dabe, A. A. Shaaban, M. Y. Abou-Zeid, and H. A. Ali, "Magneto hydrodynamic non-Newtonian nanofluid flow over a stretching sheet through a non-Darcy porous medium with radiation and chemical reaction," *Journal of Computational and Theoretical Nanoscience*, vol. 12, no. 12, pp. 5363–5371, 2015.

[11] A. A. Afify, "The influence of slip boundary condition on casson nanofluid flow over a stretching sheet in the presence of viscous dissipation and chemical reaction," *Mathematical Problems in Engineering*, vol. 2017, Article ID 3804751, 12 pages, 2017.

[12] B. Arun, M. J. Begam, M. Deivanayak, and A. H. Shenofer, "Analysis of magneto casson nanofluid with chemical reaction," *Third International Conference on Material Science, Smart Structures and Applications*, vol. 2327, Article ID 20056, 2021.

[13] A. V. Kuznetsov and A. A. Avramenko, "Effect of small particles on this stability of bioconvection in a suspension of gyrotactic microorganisms in a layer of finite depth,"

International Communications in Heat and Mass Transfer, vol. 31, no. 1, pp. 1–10, 2004.

[14] N. A. Hill and T. J. Pedley, "Bioconvection," *Fluid Dynamics Research*, vol. 37, no. 1-2, pp. 1–20, 2005.

[15] Z. Alloui, T. H. Nguyen, and E. Bilgen, "Bioconvection of gravitactic microorganisms in a vertical cylinder," *International Communications in Heat and Mass Transfer*, vol. 32, no. 6, pp. 739–747, 2005.

[16] M. J. Uddin, Y. Alginahi, O. A. Bég, and M. N. Kabir, "Numerical solutions for gyrotactic bioconvection in nanofluid-saturated porous media with Stefan blowing and multiple slip effects," *Computers & Mathematics with Applications*, vol. 72, no. 10, pp. 2562–2581, 2016.

[17] A. J. Chamkha, A. M. Rashad, P. K. Kameswaran, and M. M. M. Abdou, "Radiation effects on natural bioconvection flow of a nanofluid containing gyrotactic microorganisms past a vertical plate with streamwise temperature variation," *Journal of Nanofluids*, vol. 6, no. 3, pp. 587–595, 2017.

[18] B. Mallikarjuna, A. Saggurthi, M. J. B. Reddy, and D. K. Mohanta, "PMU Based Distance Protection Methodology to Avert Malfunction Due to FACTS Controllers," in *Proceedings of the 2018 20th National Power Systems Conference (NPSC)*, pp. 1–6, IEEE, Tiruchirappalli, India, December, 2018.

[19] S. I. Abdelsalam and M. M. Bhatti, "Anomalous reactivity of thermo bioconvective nanofluid towards oxytactic microorganisms," *Applied Mathematics and Mechanics*, vol. 41, no. 5, pp. 711–724, 2020.

[20] I. Ahmad, S. Aziz, N. Ali et al., "Thermally developed Cattaneo-Christov Maxwell nanofluid over bidirectional periodically accelerated surface with gyrotactic microorganisms and activation energy," *Alexandria Engineering Journal*, vol. 59, no. 6, pp. 4865–4878, 2020.

[21] R. Dhanai, P. Rana, and L. Kumar, "Lie group analysis for bioconvection MHD slip flow and heat transfer of nanofluid over an inclined sheet: multiple solutions," *Journal of the Taiwan Institute of Chemical Engineers*, vol. 66, pp. 283–291, 2016.

[22] F. M. Hady, F. S. Ibrahim, S. M. Abdel-Gaied, and M. R. Eid, "Boundary-layer non-Newtonian flow over vertical plate in porous medium saturated with nanofluid," *Applied Mathematics and Mechanics*, vol. 32, no. 12, pp. 1577–1586, 2011.

[23] S. A. A. Shah, N. A. Ahammad, E. M. T. E. Din, F. Gamaoun, A. U. Awan, and B. Ali, "Bio-convection effects on Prandtl hybrid nanofluid flow with chemical reaction and motile microorganism over a stretching sheet," *Nanomaterials*, vol. 12, no. 13, p. 2174, 2022.

[24] M. S. Alqarni, "Thermo-bioconvection flow of Walter's B nanofluid over a Riga plate involving swimming motile microorganisms," *AIMS Mathematics*, vol. 7, no. 9, 16248 pages, Article ID 16231, 2022.

[25] H. A. Nabwey, S. I. Alshber, A. M. Rashad, and A. E. N. Mahdy, "Influence of bioconvection and chemical reaction on magneto—carreau nanofluid flow through an inclined cylinder," *Mathematics*, vol. 10, no. 3, p. 504, 2022.

[26] M. Dhlamini, H. Mondal, P. Sibanda, S. S. Mosta, and S. Shaw, "A mathematical model for bioconvection flow with activation energy for chemical reaction and microbial activity," *Pramana - Journal of Physics*, vol. 96, no. 2, p. 112, 2022.

Hindawi
Journal of Chemistry
Volume 2023, Article ID 7571588, 16 pages
https://doi.org/10.1155/2023/7571588

Research Article

Investigation of the Wear Behavior of AA6063/Zirconium Oxide Nanocomposites Using Hybrid Machine Learning Algorithms

R. Reena Roy,[1] Leninisha Shanmugam,[1] A. Vinothini,[1] Nirmala Venkatachalam,[2] G. Sumathy,[3] Bhavadharini Murugeshan,[1] P. Mercy Rajaselvi Beaulah,[1] and Gizachew Assefa Kerga[4]

[1]*School of Computer Science and Engineering, Vellore Institute of Technology, Chennai, Tamilnadu, India*
[2]*Department of Artificial Intelligence and Data Science, Easwari Engineering College, Chennai, Tamilnadu, India*
[3]*Department of Computational Intelligence, Faculty of Engineering and Technology, SRM Institute of Science and Technology, Kattankulathur, Chennai, Tamilnadu, India*
[4]*Department of Chemical Engineering, College of Biological and Chemical Engineering, Addis Ababa Science and Technology University, Addis Ababa, Ethiopia*

Correspondence should be addressed to Gizachew Assefa Kerga; gizachew.assefa@aastu.edu.et

Received 5 November 2022; Revised 24 March 2023; Accepted 26 April 2023; Published 18 May 2023

Academic Editor: B. R. Ramesh Bapu

This research created hot-pressed composites of the AA6063 matrix with varying concentrations of ZrO_2 (0.25, 0.5, and 1 wt %). At sliding speeds of 80, 120, and 150 mm/s, the wear performance of the specimen was studied at loads of 10 N, 15 N, 20 N, and 25 N. The authors analyzed the counter-face material, the wear debris, and the worn surfaces to learn about the wear mechanisms. Developing these three machine learning (ML) algorithms was to evaluate the ability to predict wear behavior using the same small dataset collected using varying test processes. A thorough examination of each model hyperparameter tuning phase was performed. The predictive performance was analyzed using several statistical tools. The most effective decision-making algorithms for this data collection were those based on trees. Predictions made by the decision tree algorithm for the test and validation measurements have an accuracy of 86% and 99.7%, respectively. The best model was picked out based on the results of the predictions.

1. Introduction

Aluminum (Al) has considerable potential to be utilized in the aviation and automation industries to minimize emissions owing to its less density, well machinability, damping capability, and recyclability. Al has a less elastic modulus, minimal wear resistance, and a maximum corrosion rate, which are all significant problems. Various particle reinforcements have been reported to be added to the Al alloy matrix to solve these issues [1].

Unfortunately, weak tribological characteristics are a drawback of Al alloys. Compared to pure Al alloys, AMMCs (aluminum metal matrix composites) perform better in strength, stiffness, and wear [2]. AMMCs incorporate Al alloys with various reinforcements, including SiC, Al_2O_3, B_4C, TiB_2, CNT, and GNPs [3]. Due to its outstanding thermal stability, Al_2O_3 is widely used in many applications. As a result, the metal matrix and the reinforcement elements do not go through the brittle phase. So, because of its exceptional characteristics, Al_2O_3 is frequently used in the manufacturing of AMMCs [4].

Aerospace applications for the high-strength AA6063 include fasteners, shafts, and gears. The natural deterioration of these parts through rubbing is important [5]. Therefore, significant breakdowns in industrial operations may result from material loss due to wearing [6]. For this reason, investigating how AMMCs behave tribologically is essential. It is common knowledge that running trials to determine wear behavior is time consuming and costly. Machine learning strategies are used to cut down on the cost and duration of

probes. By analyzing past wear patterns, these techniques allow for accurate predictions of future behavior [7]. The surface roughness and wear loss of materials are predicted using a variety of machine learning techniques, including artificial neural networks (ANNs) [8], support vector regression (SVR), and extreme learning machines (ELMs) [9]. In addition, the effect of several wear factors (sliding speed, load, and sliding distance) was investigated using analysis of variance (ANOVA).

Most industrial procedures can be classified as either solid-state or liquid-state processes. The mechanical properties of solid-state processes are far superior to those of their liquid-state counterparts. Improved mechanical properties are linked to decreased segregation and intermetallic phase formation [10].

Machine learning (ML) was the only available method to solve the computational problems of big data science. Glasses and alloys have intricate and disordered microstructures and have benefitted from ML approaches in comprehending composition-engineering property relationships [11]. Mechanical property predictions can also be made with reasonable accuracy using ML methods based on atomistic descriptors. For instance, an ANN can be trained to estimate organic structure composites based on structural or topological properties [12].

Pumps, bearings, propellers, engineering tools, and dies all benefit from copper alloys' excellent strength, hardness, wear resistance, and abrasive resistance [13]. The material's high tensile strength and hardness exemplify the mechanical properties of aluminum bronze. Right now, we must resort to destructive testing methods that are both expensive and time consuming to evaluate the mechanical parts made of aluminum bronze. Therefore, there is an immediate need for a reliable means of evaluating aluminum bronze's mechanical qualities.

Predicting the mechanical properties of materials using machine learning techniques has grown increasingly popular in recent years. The author found that the back-propagation artificial neural network (BP-ANN) model could reliably forecast AMC's bending toughness and hardness [14]. The strength of aluminum-copper-magnesium-silver alloys was predicted using support vector regression (SVR) [15]. This research showed that, compared to BP-ANN, SVR models performed better under controlled conditions. The author developed a high-precision ANN model to forecast the UTS of niobium-silicon alloy [16]. The model was essential in facilitating their mission of improving specimen strength by modifying its microstructure. The authors [17] employed an ANN model to predict the mechanical properties of A357 alloy, and their results show that the back-propagation model is very accurate. Using an artificial neural network model, the authors [18] could predict the HB of 18-5PH and fine-tune a temperature treatment protocol to achieve maximum HB.

Since its inception over 20 years ago, the field of artificial intelligence, known as machine learning, has been an indispensable and foundational part of many businesses. Although ML was initially researched in the field of computer science and mathematics, it is often preferred by researchers to use low-content nano-reinforcement particles rather than high-range microsupplements [19]. Nano-reinforcements improve particular strength and flexibility without compromising density, in contrast to microreinforcements.

Only a few investigations on Al/ZrO_2 composites were found when searching the academic literature. The authors investigated the corrosion and mechanical performance of powder metallurgy-produced nanocomposite Al-0.5 Zn/1.0 ZrO_2 [20]. Composite materials, they said, have greater compressive strength than pure aluminum. Al/1 ZrO_2 composite has also been reported to have the highest corrosion resistance [21]. Disintegrated melt deposition of Al yields mechanical and flammability qualities, which were studied by the authors [22], who looked at the impact of ZrO_2 particle size (submicron, micron, and nano) on these characteristics.

The exceptional success of machine learning in forecasting the outcomes of expensive and time-consuming trials makes it a crucial tool for predicting the wear performance of Al matrix composites [23]. No research was found in the literature studies that indicated the wear behavior of AA6063/ZrO_2 composites.

This research examines the various machine learning models (support vector regressor, random forest, and decision tree) that can forecast how the AA6063/ZrO_2 composites will perform under wear conditions. Powder metallurgy was used to create 0.25 wt%, 0.5 wt%, and 1 wt% AA6063/ZrO_2 composites. Sliding at 80 mm/s, 120 mm/s, and 150 mm/s while applying 10 N, 15 N, 20 N, and 25 N was used to assess the *s* wear performance samples. It was determined that three-machine learning algorithms could be used to forecast the wear performance of the sample.

2. Experimental Density

The matrix and reinforcing materials are AA6063 and ZrO_2 powders, respectively. The matrix material has an even distribution of the elements Zn (0.1 wt %), Cu (0.1 wt %), Si (0.6 wt %), and Al (0.1 wt %) in its chemical composition. The average particle size of AA6063 powder is 40 μm, while 99.35% ZrO_2 comes in at 78 nm. Methanol is used as an etching solution to clean the specimen before SEM analysis. Powdered AA6063 and ZrO_2 are depicted in Figures 1(a) and 1(b) using scanning electron microscopy (Carl Zeiss MA15/EVO 18).

The composites were made with ZrO_2 in three distinct weight percent fractions: 0.25%, 0.5%, and 1%. ZrO_2 nanoparticles were found to have a vol% of 0.25%, 0.5%, and 1%. It took 12.5 grams of powder per output unit to achieve this blend. After subjecting the ZrO_2 nanopowders to ultrasonic vibration treatment, the AA6063 matrix powders were added. The composites were blended at a temperature of 190°C using a void distillation technique. Due to its low boiling point of 78.3°C, alcohol quickly evaporated from the mixture. Once the powder was well mixed, it was put into the graphite mold. A hot-pressing furnace with a controlled environment was used in the manufacturing process. The time spent hot pressing was 1 hour, the temperature was

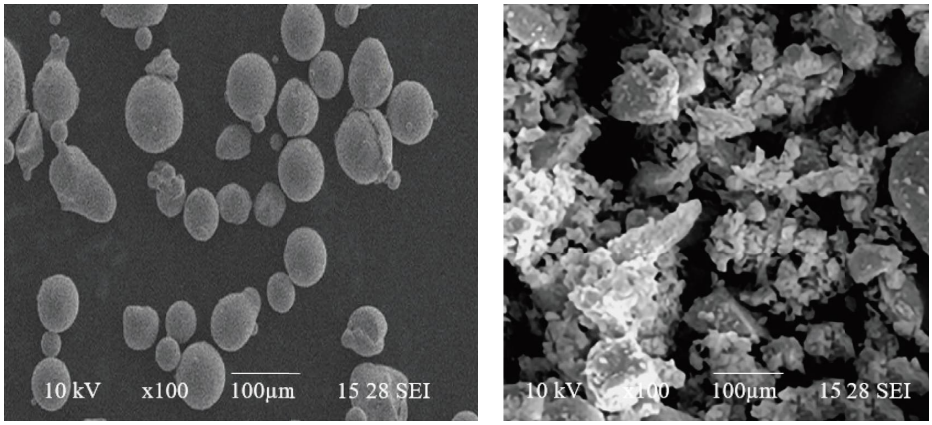

(a) (b)

Figure 1: Scanning electron microscope of (a) AA6063 and (b) ZrO_2 powders.

525°C, and the pressure was 45 MPa. Creating everything was carried out in an argon-filled environment.

The manufactured composite specimen has a radius of about 16 mm and an altitude of about 8 mm. Tests for measuring hardness were conducted using Vickers hardness test equipment (FIE, VM50) with a 1 kg load. The authors took seven readings from each sample and calculated the hardness based on the mean value.

When calculating density, a 0.1 mg resolution Kern electronic balance was used. Archimedes' principle was used to calculate the actual and relative densities of the specimen. Both air and distilled water were used to make accurate weight measurements of the samples. The applicable formula used in the calculation is as follows:

$$\rho = \frac{m_a}{m_a - m_w}\rho_{w,} \quad (1)$$

where ρ is the de nsity of the sample (g/cm^3), m_a is the mass of sample in the air, m_w is the mass of the sample in water, and ρ_w is the density of the water.

X-ray diffraction (XRD) was used to identify the phases generated during the manufacturing of AA6063 matrix composites. The microstructure was inspected using scanning electron microscopy (SEM) coupled with an energy dispersive spectrometer (EDS).

Under dry sliding conditions, the wear behavior of Al/ZrO_2 nanocomposites was investigated using a reciprocating tribometer device. Ten, fifteen, twenty, and twenty-five-newton loads at speeds of 80, 120, and 150 mm/s are used in wear tests. One hundred meters was the slide distance. The authors used AISI 420 stainless steel balls for the countertops. The wear cross-section of the specimen was calculated precisely after the abrasion tests were completed. Multiplying the cross-sectional area by the stroke distance yields the lost volume (ml).

3. Results and Discussion

3.1. Density and Microstructural Properties. Table 1 displays the outcome of density testing on AA6063 and AA6063/ZrO_2 composites. The theoretical and actual densities of the samples show a remarkable degree of agreement. This demonstrates that AA6063/ZrO_2 composites may be produced using hot pressing. To achieve the highest relative density, the AA6063 alloy was used. Increasing the percentage of ZrO_2 in the samples causes them to become less dense in comparison [24]. A high melting temperature of ceramic nanoparticles hinders compressibility and impairs consolidation, leading to a lower relative density and hence greater porosity [25]. The authors [26] found that as the ZrO_2 content of the composites with an Al matrix increased, the porosity of the composites also increased. The reports show less than 1.5% overall porosity [27]. The density findings of this investigation are found to be compatible with the literature.

SEM micrographs with magnification of 500X, 1000X, and 2000X of the samples, displayed in Figures 2(a)–2(d), reveal that neither defects nor microporosity are present. The intermetallic phase and the nanoparticles are shown to be in motion. It is easy to see the intermetallic stages in Figure 2(a). The authors [28] reported that AA6063 alloys could generate Al-Zr intermetallics. ZrO_2 nanoparticle aggregation is observed for all composite materials irrespective of ZrO_2 concentration. The increased surface area of nanoparticles is evidence of their accumulation in the composite structure [29]. Nanoparticle aggregation was reported for AA6063/2ZrO_2 composite.

The EDS results for the AA6063 alloy are shown in Figure 3. A high concentration of Al and a relatively low Zr content were found in the first analytical zone. It is good to know that the AA6063 alloy's chemical arrangement has been confirmed [30]. The high concentrations of Al and Zr found in the white particles (area 2) study identify them as Al-Zr intermetallic complexes. High O content in the structure also allows for the production of Al_2O_3. In the literature [31], Al matrix composites with Al_2O_3 were mentioned. Oxide production is linked to increased chemical action among Al and O.

These graphs display Al, O, and Zr abundance within the mapped region. The analysis conclusively demonstrated that Al makes up a large percentage of the area. High O

Table 1: Specimen's density.

Specimens Units	Theoretical density (g/cm^3)	Experimental density (g/cm^3)	Relative density (%)
AA6063 alloy	2.70	2.68	99.25
AA6063/0.25 ZrO_2	2.71	2.69	99.26
AA6063/0.5 ZrO_2	2.72	2.70	99.26
AA6063/1 ZrO_2	2.73	2.72	98.63

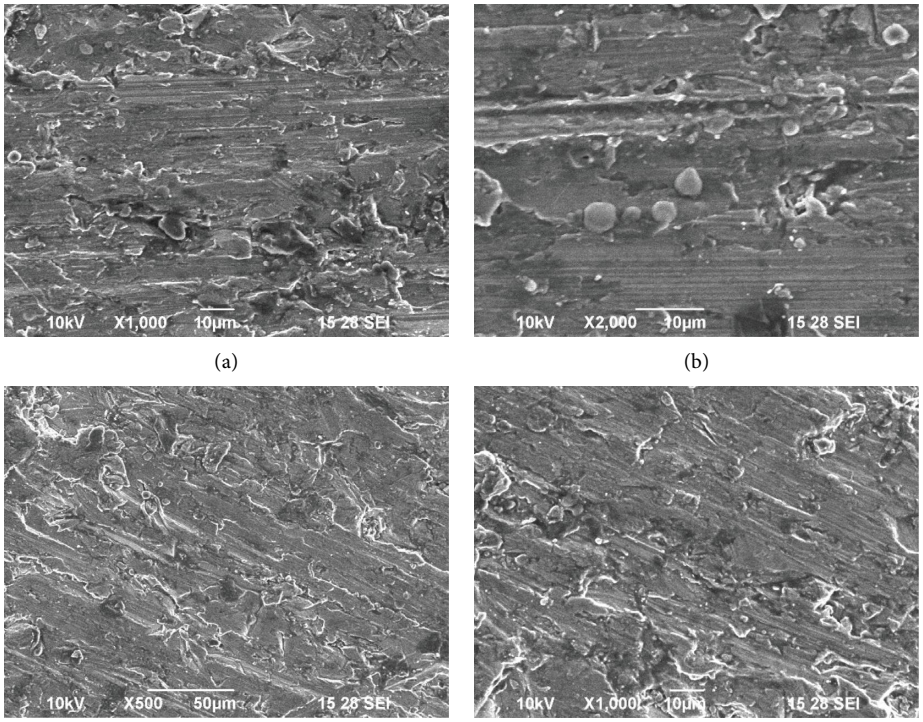

Figure 2: SEM photograph of the specimens: (a) AA6063, (b) AA6063/0.25 ZrO_2, (c) AA6063/0.5 ZrO_2, and (d) AA6063/1 ZrO_2.

distribution is also observed near grain borders. Zr was also found to be present in some locations.

The XRD patterns of AA6063, AA6063/0.25 ZrO_2, AA6063/0.5 ZrO_2, and AA6063/ZrO_2 composites are presented in Figures 4(a)–4(d). The analysis confirmed the Al phase present in the samples. The peak of the Al-Zr phase can also be seen for unreinforced alloy and composite materials [32]. Evidence of Al-Zr intermetallic compounds was verified by EDS and XRD investigation. For composites, there was no ZrO_2 peak observed. As a result of the minimal ZrO_2 in the composites, ZrO_2 peaks cannot be kept in complete constant perusing [33]. X-ray diffraction (XRD) examination of an Al/2 ZrO_2 composite was claimed to show no ZrO_2 peaks authors [24]. The test was held at a constant of between 2 and the square root of 2 or between 28.5 and 30.5. It was possible to determine both the step size (0.05) and the counting period (60 s). The inset of Figure 5 provides the value of 2 equal to 29.6, at which the ZrO_2 peak was observed.

3.2. Wear Test and Hardness Results. Table 2 displays the range of the hardness produced in the specimen. The results show that as the ZrO_2 level of the samples rises, hardness increases. This study found that the AA6063/1 ZrO_2 sample had the highest hardness (83 HV). Hardness increased from 6.2% for AA6063/0.25 ZrO_2 to 9.5% for AA6063/0.5 ZrO_2 and 14.5% for AA6063/1 ZrO_2. ZrO_2 nanoparticle indentation resistance is linked to hardness improvement in composite materials. In addition to preventing dislocation movement, the reinforcing particles are responsible for the hardness increase.

A plot of volume loss versus load for variant sliding speeds is indicated in Figure 6. It is clear from the plots that for every sliding speed and load, volume loss declines with rising ZrO_2 content. In terms of volume loss, the AA6063/1 ZrO_2 sample showed the highest durability over time. Furthermore, with a load of 25 N and a sliding speed of 80 mm/s, for instance, the volume loss of the AA6063 was recorded to be 1.56 (mm^3), but it fell to 1.13 (mm^3) for the AA6063/1 ZrO_2. The volume loss of AA6063/1 ZrO_2 was 18.6% less than that of unreinforced AA6063 when sliding at 150 mm/s while under a stress of 25 N. Increased wear behavior for MMC materials has been attributed to several distinct causes in the published literature. One of the crucial wear-increasing mechanisms [34] involves the resistance of

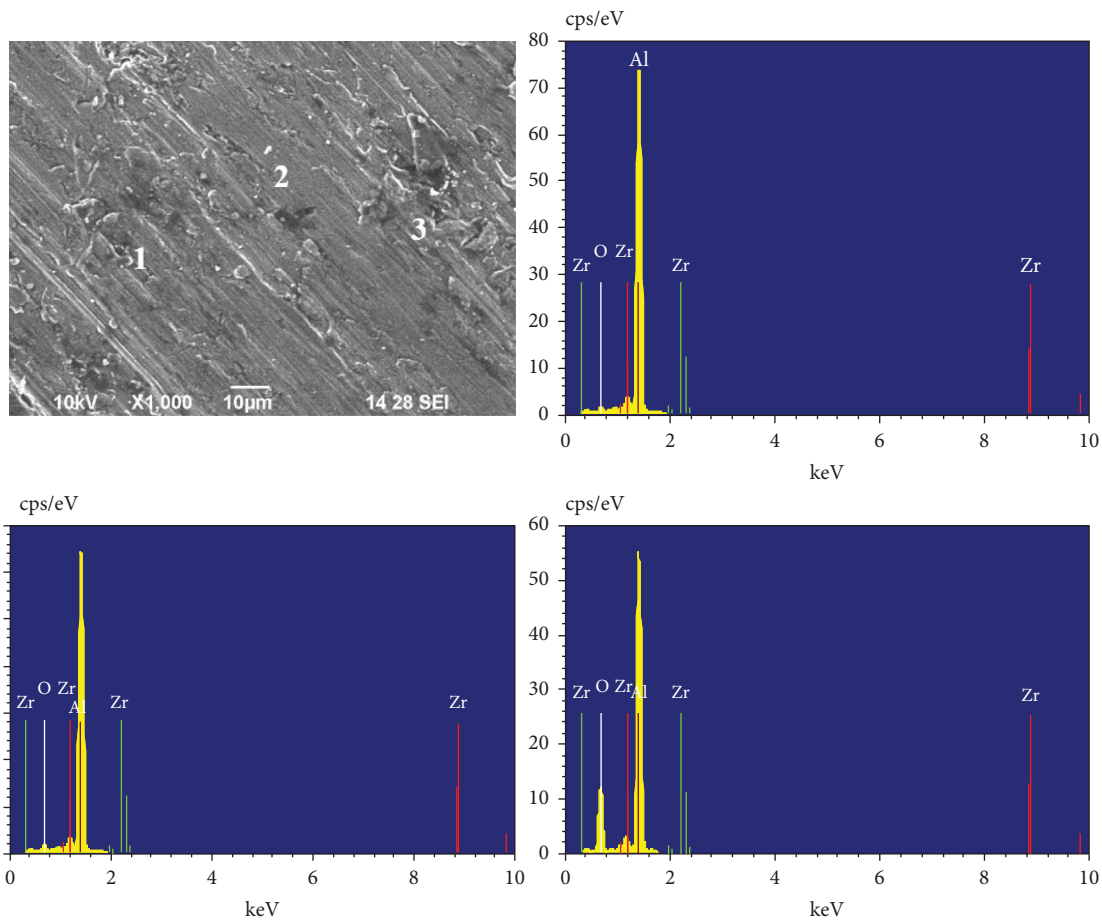

Figure 3: AA6063 analysis by EDS.

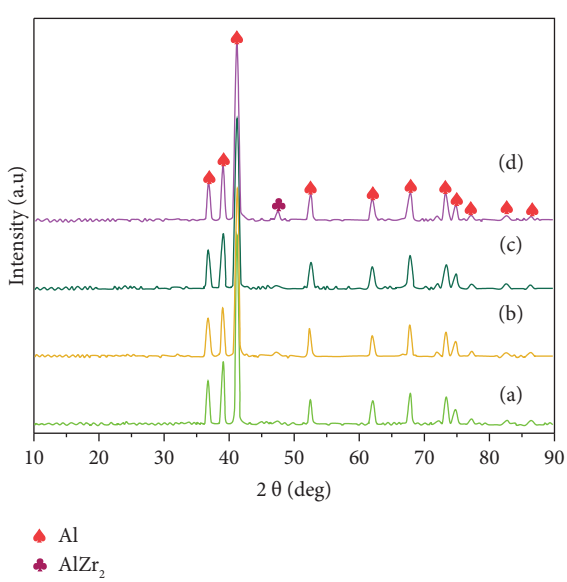

Figure 4: X-ray diffraction of (a) AA6063, (b) AA6063/0.25 ZrO_2, (c) AA6063/0.5 ZrO_2, and (d) AA6063/1 ZrO_2.

high-hardness reinforcement elements in the composite material's structure to wear degradation. The particles of reinforcement are said to bear the weight of the structure [35]. Reducing the surface area of contact between the MMC and the steel counterpart is crucial for better tribological behavior. In Figure 6, it is evident that an increase in the applied load results in a noticeable rise in the wear rate for both samples, as measured by volume loss. The wear rate of Al/ZrO_2 nanocomposites (0.3 and 0.6 wt%) increases with rising loads(from 5 N to 30 N), as observed by a researcher [36].

A plot of volume loss vs. sliding speeds for various loads is shown in Figures 5(a)–5(d). The authors saw that increasing the sliding speed reduces the volume loss across the board for all materials for a given weight. For instance, it was measured that the volume loss of AA6063/ZrO_2 under a load of 25 N varied from 1.13 (mm^3) for a sliding speed of 80 mm/s to 0.91 (mm^3) for a speed of 120 mm/s and 0.78 (mm^3) for a speed of 150 mm/s. The volume loss rises in the limits of 80 to 120 mm/s, then falls in the range of 110 mm/s and above (except for AA6063 under the load of 15 N). Surface hardness enhances wear behavior by decreasing contact area, and strain rate and surface hardness increase with increased sliding speed [37].

The authors found the wear rate of the Al/BN nanocomposite to lessen as the sliding speed was increased (from 80 to 180 mm/s) [38]. Researchers [39] analyzed a varied wear behavior for the Al alloy under minimal load and variable sliding speed, in contrast to the literature above

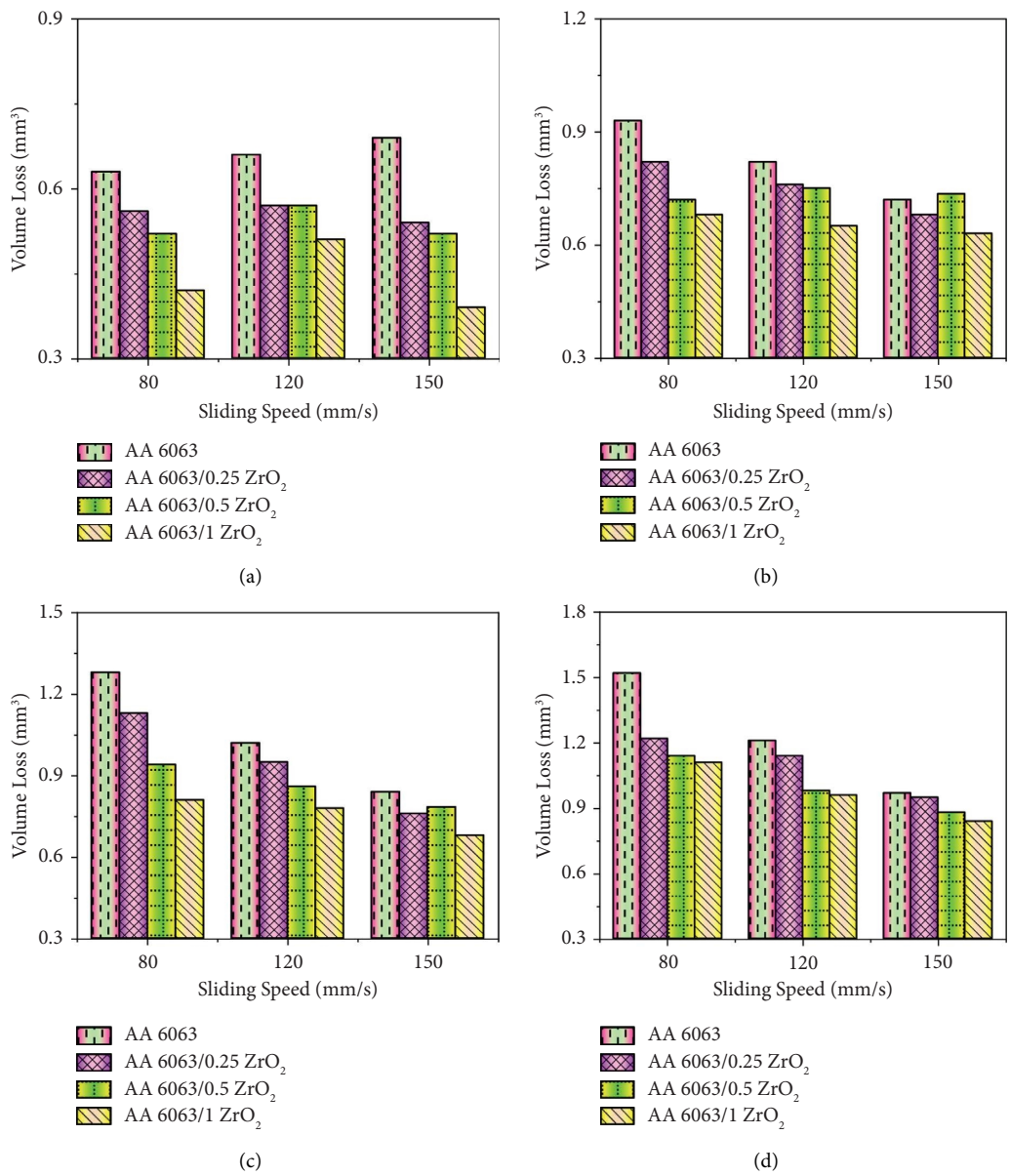

Figure 5: Variation of volume loss and sliding speed at variant loads: (a) 10, (b) 15, (c) 20, and (d) 25 N.

Table 2: Specimen's hardness.

Materials	Hardness (HV1)
AA6063	83.2 ± 1.3
AA6063/0.25 ZrO_2	84.7 ± 1.7
AA6063/0.5 ZrO_2	89.6 ± 1.8
AA6063/1 ZrO_2	91.9 ± 2.1

investigations. A higher wear rate was seen up to a sliding speed of 0.1 mm/s, after which it was observed to decrease. The authors concluded that this was because the frictional heat produced among the matrix and the counter material significantly impacted the wear process. The contact temperature and surface oxidation both rise as sliding velocity increases. Because the surface is being oxidized, friction and wear are reduced. The outcome of the low-load wear test for this investigation agrees with the study's findings [40].

In addition, Figure 5 shows wear behavior as a function of the ZrO_2 level. The volume loss diminishes with rising ZrO_2 for all weights and sliding speeds. Compared to AA6063 alloy, the volume loss of the AA6063/1 ZrO_2 composite was 44.6% less under a load of 10 N and a sliding speed of 80 mm/s. The volume loss of an AA6063 alloy decreased from 1.44 (mm^3) to 1.01 (mm^3) when loaded with 25 N while sliding at 80 mm/s, with the addition of 1 wt % ZrO_2. ZrO_2 nanoparticle incorporation significantly increased wear resistance under both low and high loads. Incorporating nano-sized ZrO_2 particles into composites results in a material with a much

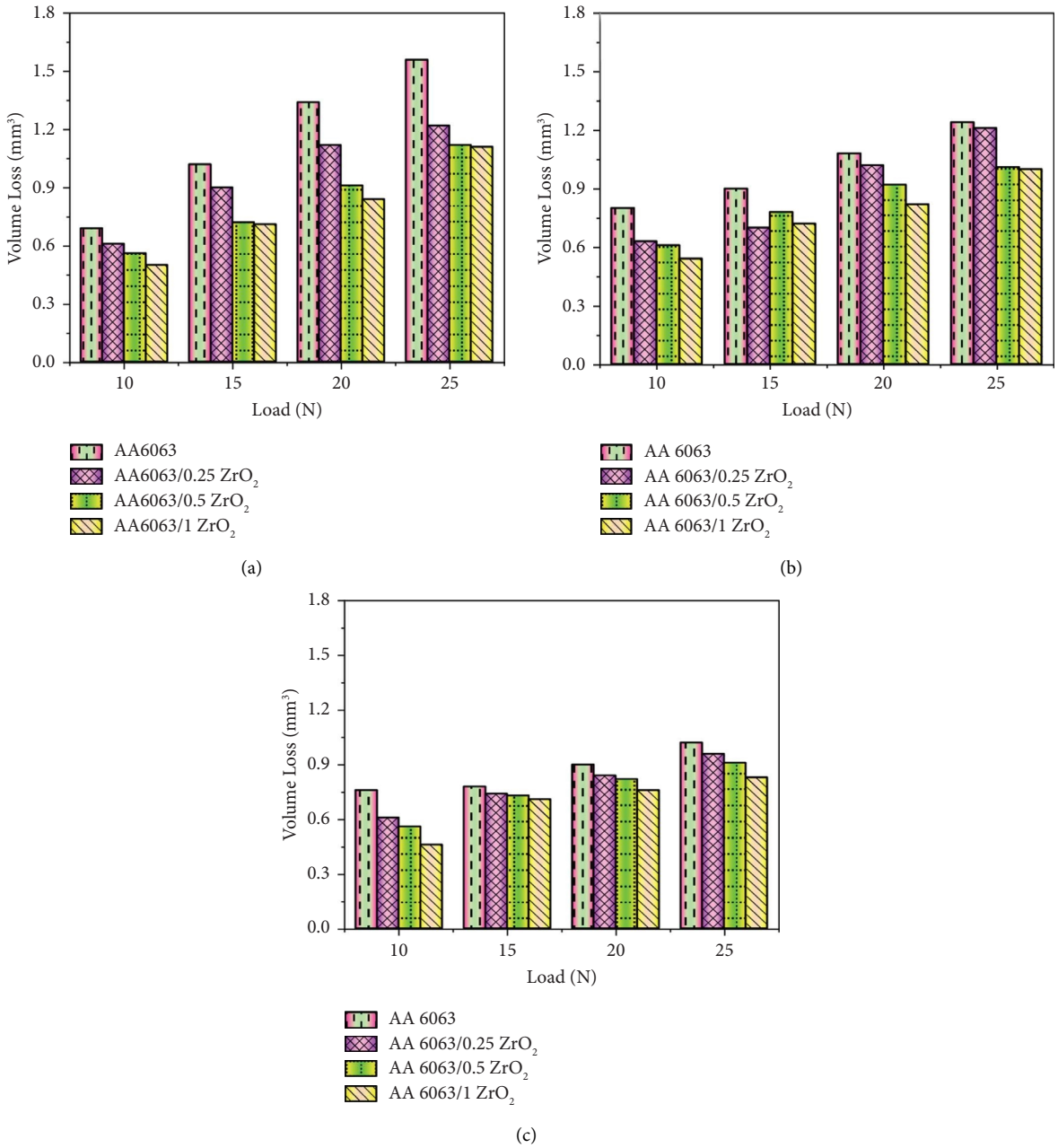

Figure 6: Variation of volume loss and load at variant sliding speeds: (a) 80, (b) 120, and (c) 150 mm/s.

higher hardness, which contributes to the material's exceptional wear resistance [41]. Results from this study on wear are consistent with Archard's law. There was a claim that more rigid materials have better tribological performance. Researchers have shown that incorporating nano-reinforcements into an Al matrix composite improves the wear resistance of the material.

Graphs of the coefficients of friction (COF) under wear conditions (80 mm/s and 150 mm/s) are presented in Figures 7(a)–7(h). In particular, it was found that the mean COF of AA6063, AA6063/0.25 ZrO_2, AA6063/0.5 ZrO_2, and AA6063/1 ZrO_2 at loads of 10 and 25 N at sliding speeds of 80 mm/s was 0.363–0.391, 0.307–0.316, 0.245–0.267, and 0.214–0.224, respectively. With a sliding speed of 150 mm/s and weights of 10 and 25 N, the mean COF of AA6063, AA6063/0.25 ZrO_2, AA6063/0.5 ZrO_2, and AA6063/1 ZrO_2 was calculated to be 0.335–0.367, 0.292–0.317, 0.231–0.253, and 0.213–0.226, respectively. The correlation between COF values and volume reduction was negative (Figures 5 and 6). Growing the strengthening in a structure improves its load-bearing volume and reduces the stress on the Al matrix. Shearing the reinforcement particles requires more energy. Hence, the composite surface has a lower friction coefficient [42].

Particles on the worn surface further reduce friction by delaying strain hardening and plastic deformation [43]. Multiple studies have found that when reinforcement content increases, COF levels fall.

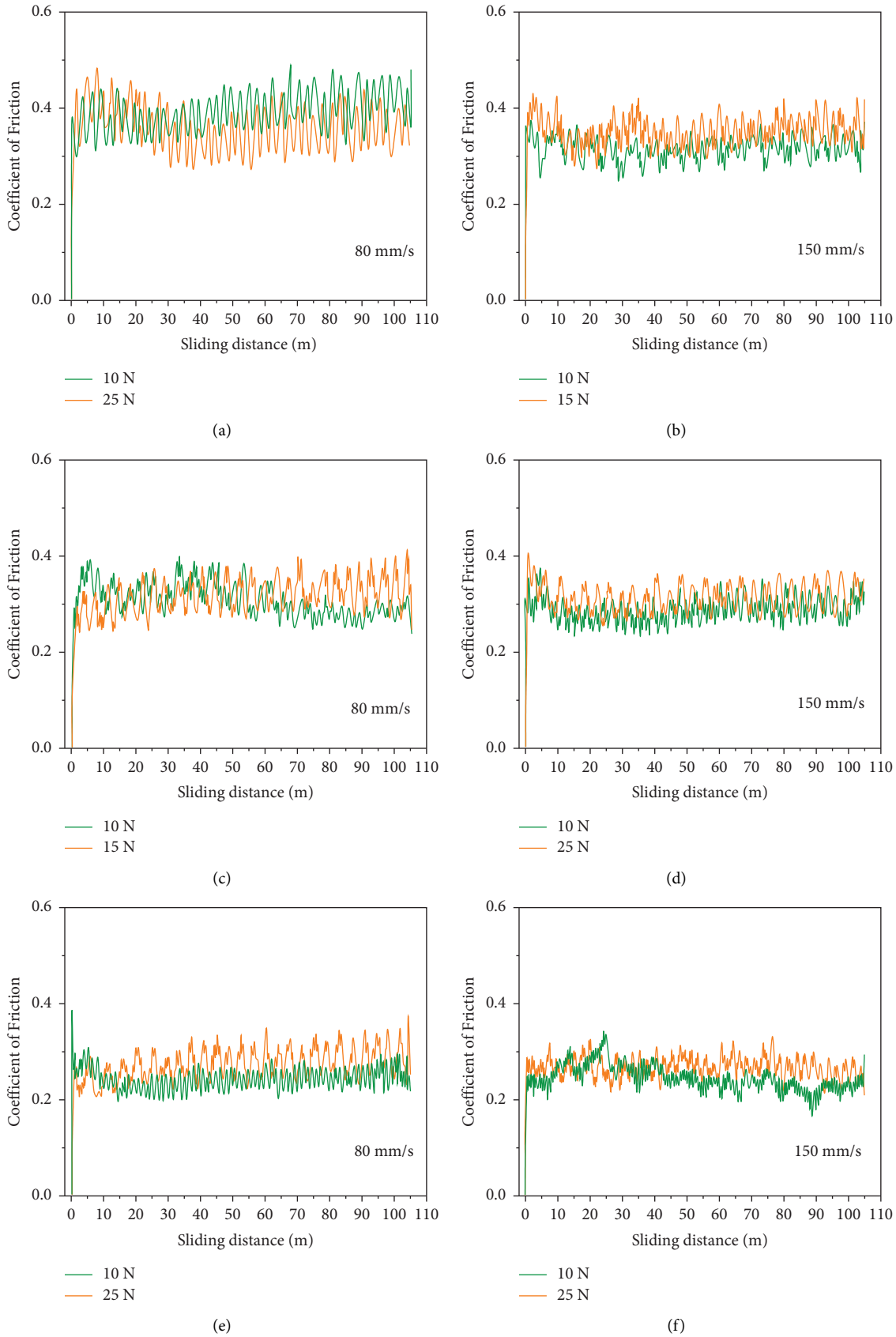

Figure 7: Continued.

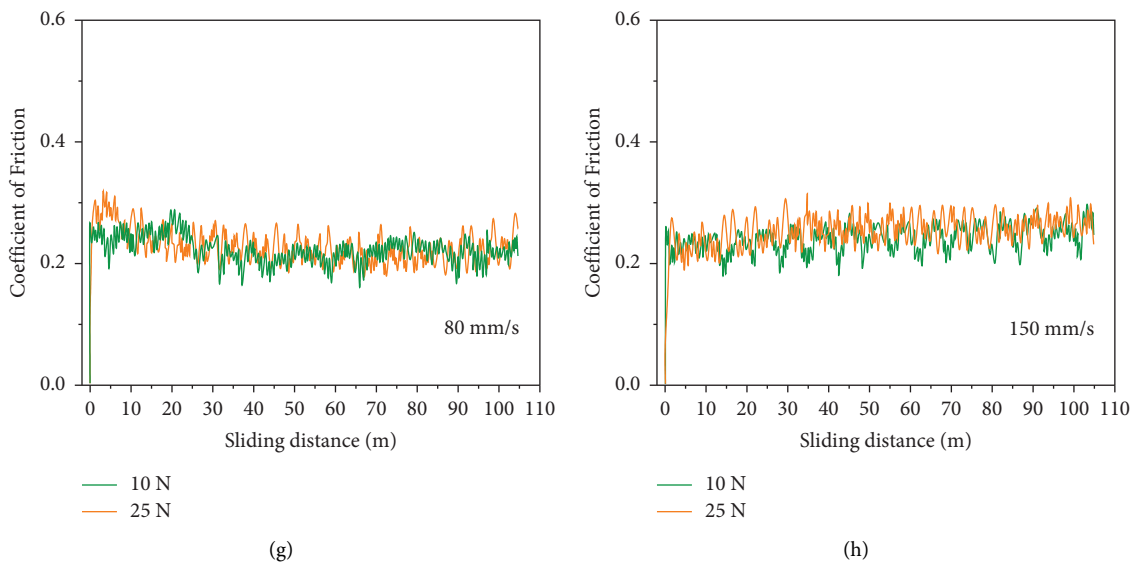

Figure 7: Evaluation of the coefficient of friction (a)-(b) AA6063, (c)-(d) AA6063/0.25 ZrO_2, (e)-(f) AA6063/0.5 ZrO_2, and (g)-(h) AA6063/1 ZrO_2.

Figure 7 shows that the COF increases with load, independent of material type, or sliding velocity. More plastic deformation occurred with a higher load, leading to a higher COF [44]. High loads cause plastic deformation and wear damage, as evidenced in the worn surface studies. Sliding faster results in a drop in the samples' COF levels, as observed in this research. According to the study, the COF drops as the wear rate rises because the oxides generated on the surface are constantly delaminating. Increased wear surface separation and larger delamination result from high speeds and contribute to a lower COF. The friction coefficient decreases due to oxygen entering metallic surfaces and forming an oxide coating on the surface.

3.3. Analysis of Worn Surface. Scanning electron microscope images of wear on the samples, taken at 80 mm/s, are shown in Figure 8(a). Even under a light 10 N load, there was evidence of deep grooves and worn detritus (Figure 8(b)). Wear caused by abrasion can be identified by grooves running perpendicular to the direction of sliding. Researchers have found that AA6063 alloy and its composites are susceptible to abrasion at low stresses [45]. When the load is increased, AA6063 alloy shows a significant delaminated region and some cracks. A large load causes shear deformation, which results in breaks during delamination wear. Under high load (25 N), the primary wear mechanism for AA6063/ZrO_2 hybrid composites was observed to be delamination and oxidation. Some grooves may be seen on the AA6063/0.25 ZrO_2 composite's worn surface.

At greater stress, the cracks and wear debris become apparent. Under a load of 10 N, the AA6063/0.5 ZrO_2 and AA6063/1 ZrO_2 surfaces show signs of wear in the form of scratches. As the load rises from 10 N to 25 N, craters and cracks appear on the AA6063/0.5 ZrO_2 and AA6063/1 ZrO_2 wear surfaces. Delamination wear leads to the creation of craters. In the images of the worn surfaces of the samples, the transition from depth grooves to scrapes indicates that the character has experienced reduced wear damage as the ZrO_2 content increases during the sliding test at 80 mm/s and a force of 10 N. A 25 N load caused a vast section of the composite material to delaminate, creating a crater. This confirms the findings of the volume loss graph, which showed that AA6063/1 ZrO_2 showed the least amount of wear damage out of all the samples.

Figure 9 displays the EDS analyses of AA6063/0.25 ZrO_2 at 25 N and a sliding speed of 80 mm/s. As seen in an EDS study, both the first and second zones are rich in Al and O. This is because, at extreme friction (25 N), Al_2O_3 is formed. Because of this, authors might say that oxidized patches cover worn surfaces.

Figure 10 displays the outcomes of an EDS analysis conducted on the samples at a sliding speed of 150 mm/s. Several studies using the EDS analysis confirmed the existence of elevated O on worn surfaces for Al matrix composites. The energy dispersive spectroscopy analysis reveals exceptionally high concentrations of Al and Zr in the structure, indicating that these areas interact with compounds containing Al and Zr.

Moreover, the research revealed an amount of Zr within the specimen. After the wear test, the ZrO_2 nanoparticles were still present in the structure, proving their durability. Analysis by EDS revealed a high percentage (68.42%) of aluminum. Increases in sliding speed and ZrO_2 concentration are readily seen to reduce the material area moved into the counter-face ball. This is because the steel counter-face makes less contact with the Al matrix due to the presence of reinforcing particles (ZrO_2). It has been established through chemical analysis that the second section contains a high concentration of steel counter-face material, as evidenced by the presence of iron (55.7%), chromium (10.5%), and carbon (5.3%).

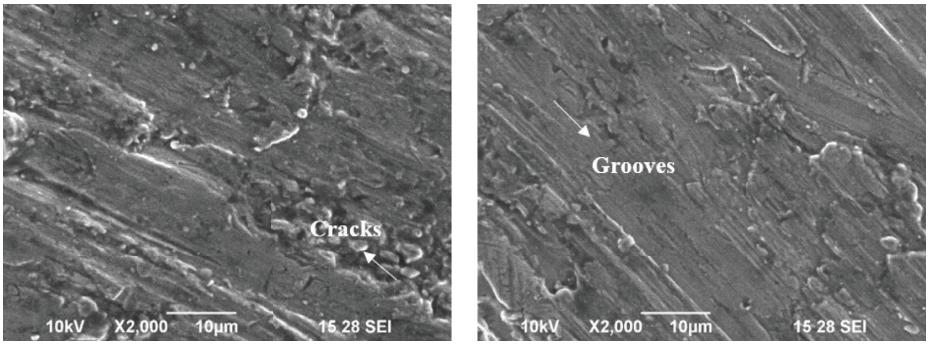

(a) (b)

Figure 8: (a) AA6063 alloy and (b) AA6063/0.25 ZrO_2 for 10 N and worn surface of the specimen at 80 mm/s sliding speed.

4. The Methods of Machine Learning Models

Many supervised machine learning regression models have been developed to create a mapping function between the input characteristics (sliding speed, ZrO_2 content, and load) and the desired output feature (accuracy).

Before being fed into ML algorithms, data from actual experiments must be cleaned, sorted, and prepared. The information is then divided randomly into two groups: training data (75%) and validation data (25%). All three ML models are set up and educated on data sets. At the end of the training process, the stability of each ML model is evaluated using cross-validation. When assessing the efficiency of the training phase, the authors used 3-folds cross-validation, which involved splitting the training data into five sets and analyzing each group separately.

However, experimentation is necessary for determining the optimal settings for the machine learning model. The grid search method is utilized, with multiple variations of each model. The models were cross-validated against one another, and the optimal settings were identified using the training set. Therefore, the top estimators were applied to validation data, and the outcomes are shown here. The data must be cleaned and normalized for the ML model to have a high degree of accuracy. The data have been preprocessed using a standard scaling method for this application. To improve the ability to forecast the ML models, preprocessing normalizes all input and output features to the same scale.

4.1. ML Models. The support vector regressor (SVR), random forest (RF), and decision tree (DT) models, three of the most widespread and effective models in recent literature [46], have been chosen for a head-to-head performance comparison on the current dataset. Volume loss is a constant real value, and a regression can be used to predict its value. Python was used for all code implementations, and all the source code is available on the GitHub platform1. The machine learning was accomplished with the help of the sci-kit learn libraries, and the visualization was performed using the seaborn libraries. This section briefly describes the theoretical foundations upon which algorithms are built. Readers interested in further exploring the topic of algorithms are directed to recent literature surveys of individual algorithms, which cover topics such as the algorithm's mathematical foundations and current uses.

4.1.1. Support Vector Regressor (SVR). For regression, SVR is a particular case of the original support vector machine. In support vector regressor, high-order hyperplanes are set up to establish a correlation between the input and the intended output measurement within predetermined limits. These hyperplanes are built using kernel functions, like radial basis and linear functions, to reduce the generalized error bound to a minimum. The regularization parameter and gamma are two primary parameters influencing the model's accuracy while constructing the hyperplanes. While SVR models can function with a small dataset, research in machine learning and tribology suggests that accuracy can be improved by providing high-dimensional data.

4.1.2. Decision Tree (DT). The DT technique constructs a tree-like structure with nodes and leaves to make predictions about the output data based on learning choice rules from the input dataset. The nodes make binary judgments dependent on the values of the input features, while the leaf displays a numerical goal. Splitting nodes can be done with the aid of mean squared error (MSE) and mean absolute error (MAE) functions. Even though increasing the tree's depth adds complexity to the model, doing so runs the risk of overfitting, wherein the model performs well on the training data because it has memorized the input but poorly on the testing data.

4.1.3. Random Forest (RF). The supervised machine learning model random forest is still another option. Classification problems shine the brightest although it also excels in regression. The random forest algorithm is called the ensemble technique that uses decision trees that have been randomly generated. It uses random data sampling from the training set to train various decision trees. The parameter n estimators, which represent the total number of trees in the forest, control how many trees will be created through the training phase. Inheritance from the DT model is used for the remaining model parameters.

4.2. Hyperparameter Tuning. The process of fine-tuning each parameter of ML model values has begun. Table 3 shows the various models and their respective setup parameters. For this reason, the factor subset combinations have been put up independently for each model due to their unique tuning parameters.

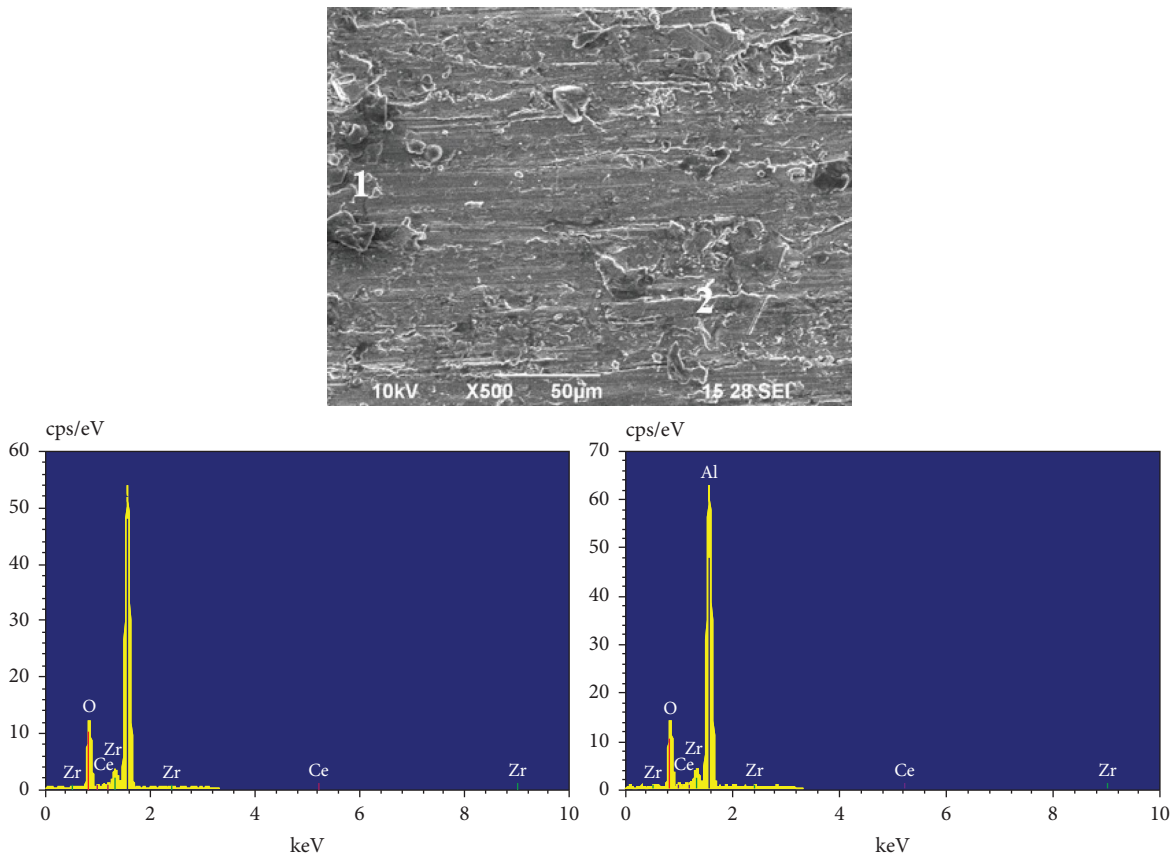

Figure 9: AA6063/0.25 ZrO_2 at 25 N for 80 mm/s analysis on EDS.

After finishing the hyperparameter tuning process, the optimal settings for each model may be identified. Results from experiments show that the optimal settings for SVR are as follows: regularization parameter $C = 100$, rbf kernel, and coefficient gamma = 0.001. The optimal settings for RF include a maximum of two features per split (MF), one leaf node (MSL), and 100 decision trees (NE). Assuming a maximum depth of 8, the optimal splitting criterion for DT is absolute error and the minimum splitting level is set at 1.

A total of four measures (R^2, RMSE, MSE, and MAE) were employed to evaluate the results of ML models. For scoring regression functions, authors utilize a statistic called R^2, which is determined by the following formula:

$$R^2 = \frac{\sum_{i=1}^{n}(y_i - \hat{y}_i)^2}{\sum_{i=1}^{n}(y_i - \overline{y})^2}, \tag{2}$$

where n is the no. of tests, y_i is the real measuring output value, $\hat{y}_i$ is the predicting output value, and $\overline{y}$ is the mean value of y_i.

$$\text{RMSE} = \sqrt{\frac{\sum_{i=1}^{n}(y_i - \hat{y}_i)^2}{n}}. \tag{3}$$

Mean squared error (MSE) is the average squared deviation from the projected values.

$$\text{MSE} = \frac{\sum_{i=1}^{n}(y_i - \hat{y}_i)^2}{n}. \tag{4}$$

Mean absolute error (MAE) is the difference between the actual and expected values.

$$MAE = \frac{\sum_{i=1}^{n}|y_i - \hat{y}_i|}{n}. \tag{5}$$

The R^2 value of the model will be 1, and the others will be 0 if it is a perfect match for the data, as is evident from equation (2). R^2 provides more insight into the data's variability than the other three measures. Due to their monotonically connected representation of the squared errors among observed and predicted output values, RMSE and MSE are of interest. More resilient to outlier data, MAE also displays the mean value of the absolute error among the actual and predicted output values.

Models with optimal settings had the best R^2, RMSE, MSE, and MAE values, shown in Table 4. Cross-validated training has allowed us to give mean and standard deviation. Table 4 indicates that DT is the most precise and reliable model, with a mean R^2 of 0.8580 and a standard deviation of 0.0220. Results on the test dataset showed that RF was competitive with DT.

The regression, root mean squared error, mean squared error, and mean absolute error for each algorithm volume loss validations are shown in Table 5. It has been claimed that

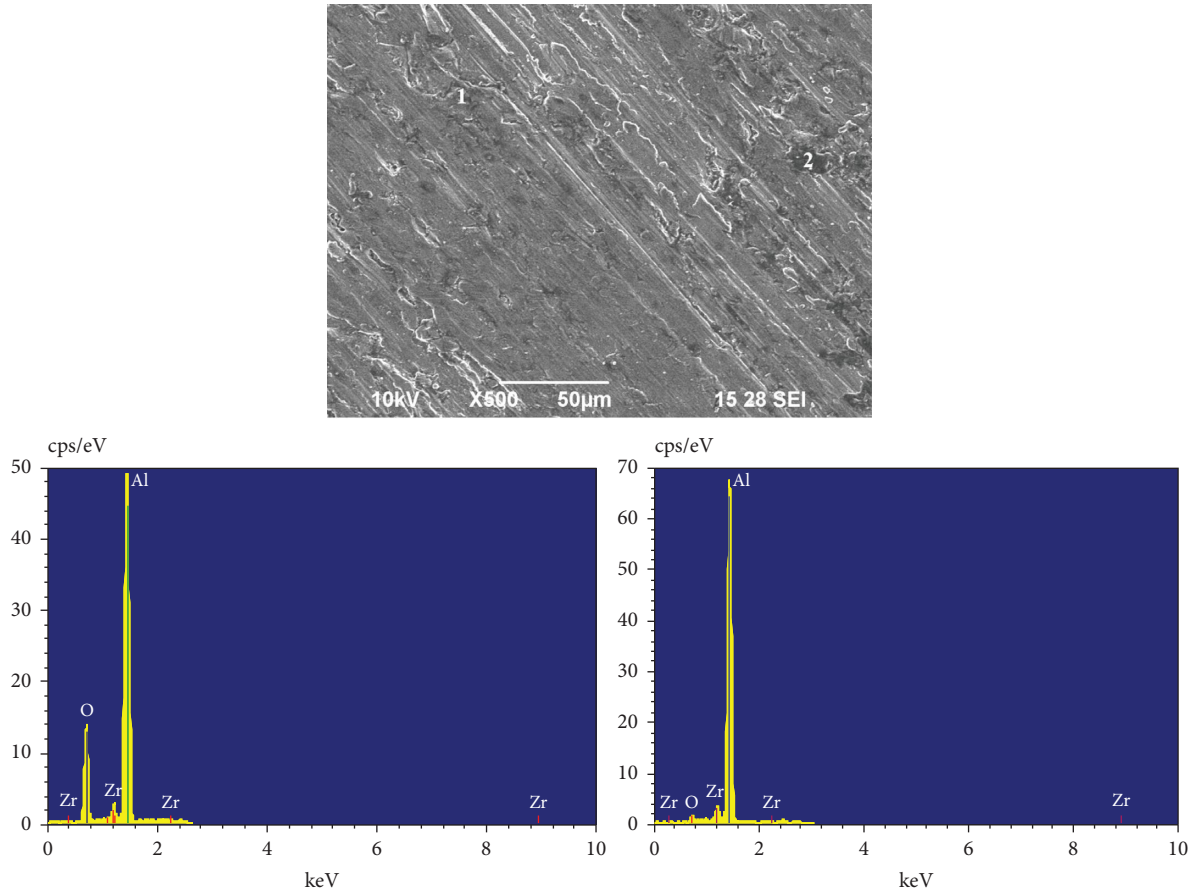

Figure 10: EDS specimen at 150 mm/s and AA6063/0.5 ZrO_2 (10 N).

Table 3: Models with a certain class of hypertuned parameters.

ML algorithms	Factors
RF	MF = {3, 4}, MSL = {4, 5, 6}, NE = {15, 25, 55, 100}
DT	S = {MSE, MAE}, MD = {1, 5, 7, 10}, MSL = {4, 5, 6}, MWFL = {0.1, 0.2, 0.5}
SVR	kernel = {rbf, linear}, gamma = {$1e-4$, $1e-5$}, C = {1, 10, 100}

Table 4: Relative results of machine learning algorithms on testing data.

Metrics	Regression		Root mean squared error		Mean squared error		Mean absolute error	
Machine learning algorithm	Mean	STD	Mean	STD	Mean	STD	Mean	STD
Support vector regression	0.8186	0.0949	0.3774	0.1908	0.1788	0.1873	0.3055	0.1766
Random forest	0.8504	0.0599	0.3523	0.1502	0.1467	0.1381	0.2896	0.1126
Decision tree	0.8587	0.0226	0.3481	0.1114	0.1337	0.0917	0.2696	0.0924

values of R^2 for a model between 0.7 and 0.9 are acceptable. A model is deemed high quality if its R^2 value is more than 0.9. The R^2 value on the validation dataset ranged from 0.8078 to 0.9973 (Table 5). Tree-based ML models (RF and DT) outperformed higher-order models (SVR), which is an exciting finding. Therefore, the overfitting problem associated with limited data and the inability to generalize could be a contributing factor. The fundamental disadvantage of tree-based approaches is that they need to be recreated and recalculated whenever new data is introduced to the current model because this impacts all prior iterations.

Figure 11 displays the predicted and observed volume decrease from each regressor. Volume loss was successfully expected by both RF(b) and DT(c). However, SVR (a) fared

Table 5: Relative results on machine learning algorithm on validating data.

Machine learning algorithms	Regression	Root mean squared error	Mean squared error	Mean absolute error
Support vector regression	0.8084	0.3922	0.1539	0.2578
Random forest	0.9784	0.1326	0.0183	0.0937
Decision tree	0.9926	0.0814	0.0071	0.0214

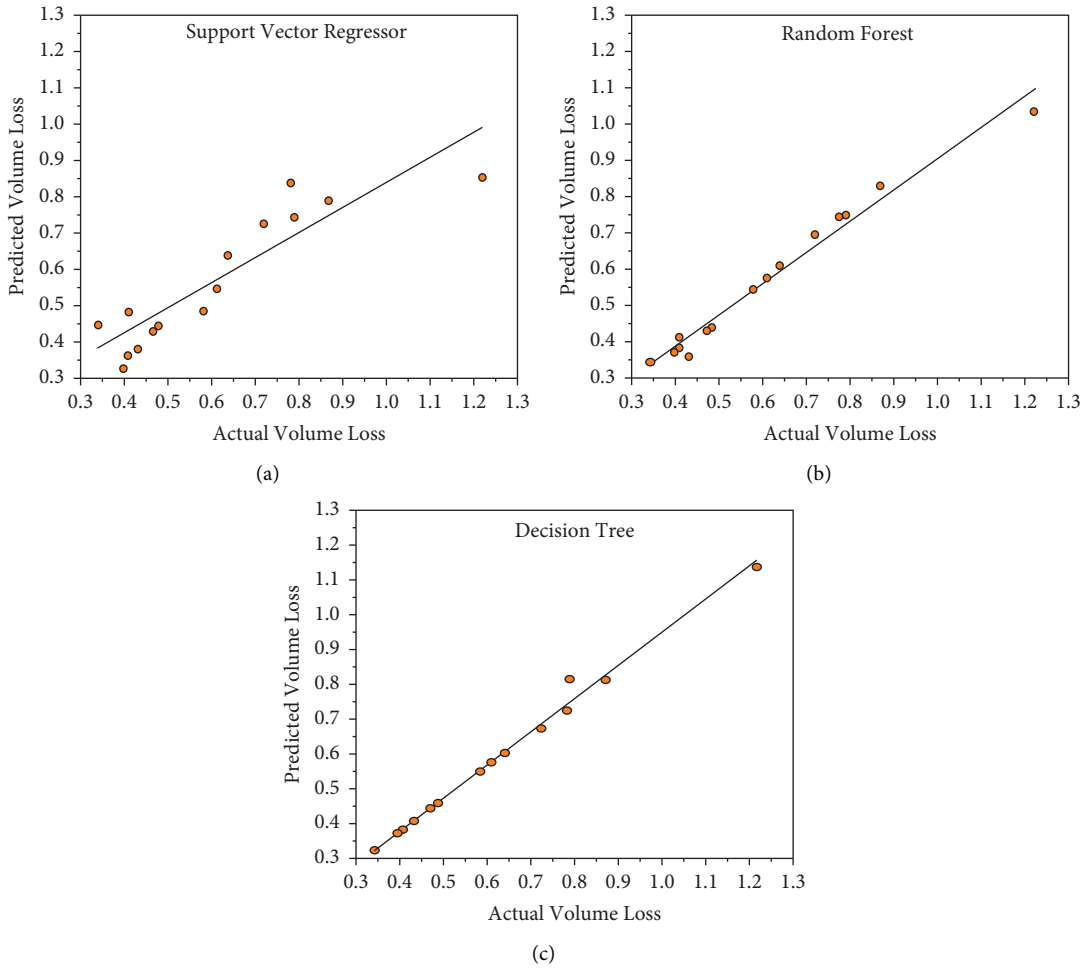

Figure 11: Evaluation of the actual volume loss and predicted volume loss by the machine learning algorithm.

poorly on the validation data set. SVR has a more significant margin of error compared to RF and DT.

As shown in Figure 12, the load, ZrO_2 content, and sliding speed are three of the most important input variables used by various ML models to estimate volume loss. Each variable affects the predicted volume loss, as shown in Figure 12. The load was the primary factor in determining the outcome. According to various reports in the research literature, the load is the most critical factor when using machine learning to estimate wear rate. In contrast, the percentage of ZrO_2 and the sliding velocity were determined to be other crucial factors.

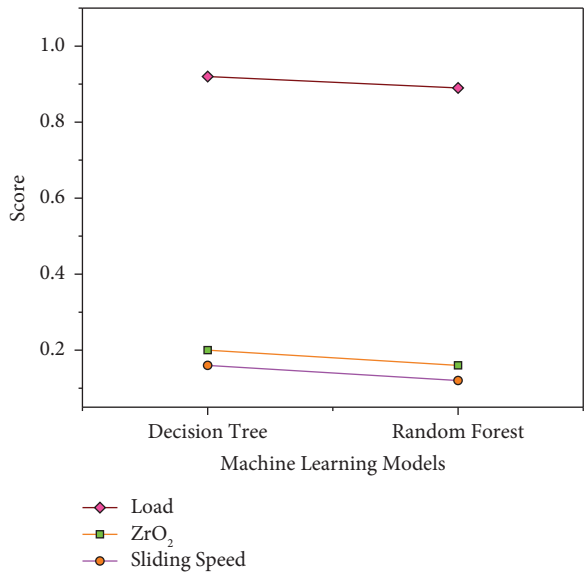

Figure 12: The significance of features in predicting volume loss.

5. Conclusions

In this research, the wear behavior and wear mechanism of a specimen made from an AA6063 matrix composite strengthened by ZrO_2 (0.25, 0.5, and 1 wt %) nanocomposites were examined after successful hot pressing. Wear resistance was predicted using three distinct machine learning methods. Here, the following are the most important findings:

(i) By adding more ZrO_2, the resulting specimens were found to have a somewhat lower relative density. For the highest porosity (1.44%), the AA6063/1 ZrO_2 composite was used. A 1 wt% ZrO_2 component enhanced the hardness of the AA6063 alloy from a measured 66.1 to a measured 74.9.

(ii) A study of the composite materials' microstructure reveals that the ZrO_2 nanoparticles aggregate into larger particles. X-ray diffraction testing confirms the existence of the Al, Al-Zr, and ZrO_2 phases.

(iii) With the same load and sliding speeds, an increase in ZrO_2 content reduced volume loss.

(iv) Abrasion was found to be a wear mechanism at 10 N, while abrasion and delamination were present at 25 N. Wear graphs showed that surfaces with higher ZrO_2 content showed reduced wear and damage.

(v) Three machine learning algorithms were evaluated for their predictive abilities on a substantial experimental dataset.

(vi) On this data set, tree-based decision algorithms performed the best. The accuracy of the decision tree algorithm's predictions for the test and validation measurements was 86% and 99.7%, respectively.

(vii) Three ML techniques were used to state the relative weights of the input features explicitly. It has been found that the load parameter has the most significant impact on the prediction of volume loss measurement.

Data Availability

The data used to support the findings of the study are included in the paper.

Ethical Approval

All procedures performed in this study involving human participants were by the ethical standards of the institutional and/or national research committee and its later amendments or comparable ethical standards.

Conflicts of Interest

The authors declare no that there are no conflicts of interest.

References

[1] J. Arockia Dhanraj, B. Lingampalli, M. Prabhakar, A. Sivakumar, B. Krishnamurthy, and K. C. Ramanathan, "A credal decision tree classifier approach for surface condition monitoring of friction stir weldment through vibration patterns," *Materials Today Proceedings*, vol. 46, pp. 1127–1133, 2021.

[2] U. Ali, W. Muhammad, A. Brahme, O. Skiba, and K. Inal, "Application of artificial neural networks in micromechanics for polycrystalline metals," *International Journal of Plasticity*, vol. 120, pp. 205–219, 2019.

[3] Z. Zaidi, N. Maiti, M. I. Ali et al., "Fabrication, characteristics, and therapeutic applications of carbon-based nanodots," *Journal of Nanomaterials*, vol. 2022, Article ID 8031495, 12 pages, 2022.

[4] I. Guagliardi, A. M. Astel, and D. Cicchella, "Exploring soil pollution patterns using self-organizing maps," *Toxics*, vol. 10, no. 8, p. 416, 2022.

[5] T. A. Amibo, S. M. Beyan, M. Mustefa, V. P. Sundramurthy, and A. B. Bayu, "Development of nanocomposite based antimicrobial cotton fabrics impregnated by nano SiO2 loaded AgNPs derived from eragrostis teff straw," *Materials Research Innovations*, vol. 26, no. 7, pp. 405–414, 2021.

[6] A. Vasylenko, J. Gamon, B. B. Duff et al., "Element selection for crystalline inorganic solid discovery guided by unsupervised machine learning of experimentally explored chemistry," *Nature Communications*, vol. 12, no. 1, p. 5561, 2021.

[7] Y. Wu and D. L. Irving, "Prediction of chemical ordering in refractory high-entropy superalloys," *Applied Physics Letters*, vol. 119, no. 11, Article ID 111901, 2021.

[8] E. Varol Altay, E. Gurgenc, O. Altay, and A. Dikici, "Hybrid artificial neural network based on a metaheuristic optimization algorithm for the prediction of reservoir temperature using hydrogeochemical data of different geothermal areas in Anatolia (Turkey)," *Geothermics*, vol. 104, Article ID 102476, 2022.

[9] K. Parkavi and P. Vivekanandan, "A novel cluster based energy efficient protocol for wireless networks," in *Proceedings of the IEEE-International Conference On Advances In Engineering, Science And Management (ICAESM-2012)*, pp. 645–650, Nagapattinam, India, March 2012.

[10] P. Singh, D. Sauceda, and R. Arroyave, "High temperature oxidation behavior of disordered (Ti0.5Zr0.5)2AlC MAX phase via a Machine Learning-Augmented DFT approach," *Materials Letters X*, vol. 10, Article ID 100062, 2021.

[11] A. Mariappan, "The application of energetic materials genome approach for development of the solid propellants through the space debris recycling at the space platform," in *Proceedings of the AIAA Propulsion and Energy 2020 Forum*, pp. 1–18, August 2020.

[12] N. Sizochenko, M. Syzochenko, N. Fjodorova, B. Rasulev, and J. Leszczynski, "Evaluating genotoxicity of metal oxide nanoparticles: application of advanced supervised and unsupervised machine learning techniques," *Ecotoxicology and Environmental Safety*, vol. 185, Article ID 109733, 2019.

[13] L. Shanmugam, K. Gunasekaran, A. Natarajan, and V. Kaliaperumal, "Quantitative growth analysis of pulp necrotic tooth (post op) using modified region growing active contour model," *IET Image Processing*, vol. 11, no. 11, pp. 1015–1019, 2017.

[14] N. Venkatachalam, L. Shanmugam, G. C. Heltin, G. Govindarajan, and P. Sasipriya, "Enhanced segmentation of inflamed ROI to improve the accuracy of identifying benign and malignant cases in breast thermogram," *Journal of Oncology*, vol. 2021, Article ID 5566853, 17 pages, 2021.

[15] R. Reena Roy and G. S Anandha Mala, "Early detection of pancreatic cancer using jaundiced eye images," *Computer Systems Science and Engineering*, vol. 41, no. 2, pp. 677–688, 2022.

[16] A. Jaiswal and Y. Zhang, "Robustness of dynamical cluster analysis in a glass-forming metallic liquid using an unsupervised machine learning algorithm," *MRS Advances*, vol. 1, no. 26, pp. 1929–1934, 2016.

[17] C. Li, S. C. Yang, Q. S. Guo et al., "Determining the geographical origin of the medicinal plant Marsdenia tenacissima with multi-element analysis and data mining techniques," *Chemometrics and Intelligent Laboratory Systems*, vol. 136, pp. 115–120, 2014.

[18] S. Kar, K. Pathakoti, P. B. Tchounwou, D. Leszczynska, and J. Leszczynski, "Evaluating the cytotoxicity of a large pool of metal oxide nanoparticles to *Escherichia coli*: mechanistic understanding through in Vitro and in Silico studies," *Chemosphere*, vol. 264, Article ID 128428, 2021.

[19] T. Gurgenc, O. Altay, M. Ulas, and C. Ozel, "Extreme learning machine and support vector regression wear loss predictions for magnesium alloys coated using various spray coating methods," *Journal of Applied Physics*, vol. 127, no. 18, Article ID 185103, 2020.

[20] O. A. Mohamed, S. H. Masood, and J. L. Bhowmik, "Experimental study of the wear performance of fused deposition modeling printed polycarbonate-acrylonitrile butadiene styrene parts using definitive screening design and machine learning-genetic algorithm," *Journal of Materials Engineering and Performance*, vol. 31, no. 4, pp. 2967–2977, 2022.

[21] O. Altay, T. Gurgenc, M. Ulas, and C. Özel, "Prediction of wear loss quantities of ferro-alloy coating using different machine learning algorithms," *Friction*, vol. 8, no. 1, pp. 107–114, 2020.

[22] A. M. Sadoun, I. Najjar, A. Fathy et al., "An enhanced Dendritic Neural Algorithm to predict the wear behavior of alumina coated silver reinforced copper nanocomposites," *Alexandria Engineering Journal*, vol. 65, pp. 809–823, 2023.

[23] P. M. John, V. Periyasamy, and S. Arulnandhisivam, "Secure friend-based approach for ad-hoc routing using fuzzy random variables," *Int Inf Inst (Tokyo) Inf*, vol. 18, no. 2, p. 689, 2015.

[24] V. Algur, P. Hulipalled, V. Lokesha, M. Nagaral, and V. Auradi, "Machine learning algorithms to predict wear behavior of modified ZA-27 alloy under varying operating parameters," *Journal of Bio- and Tribo-Corrosion*, vol. 8, no. 1, p. 7, 2022.

[25] T. Gurgenc and O. Altay, "Surface roughness prediction of wire electric discharge machining (WEDM)-machined AZ91D magnesium alloy using multilayer perceptron, ensemble neural network, and evolving product-unit neural network," *Materials Testing*, vol. 64, no. 3, pp. 350–362, 2022.

[26] J. Singh and S. Singh, "Neural network supported study on erosive wear performance analysis of Y2O3/WC-10Co4Cr HVOF coating," *Journal of King Saud University - Engineering Sciences*, vol. 35, 2022.

[27] I. S. N. V. R. Prasanth, P. Jeevanandam, P. Selvaraju et al., "Study of friction and wear behavior of graphene-reinforced AA7075 nanocomposites by machine learning," *Journal of Nanomaterials*, vol. 2023, Article ID 5723730, 15 pages, 2023.

[28] Y. Zhang, K. Mao, S. Leigh, A. Shah, Z. Chao, and G. Ma, "A parametric study of 3D printed polymer gears," *International Journal of Advanced Manufacturing Technology*, vol. 107, no. 11–12, pp. 4481–4492, 2020.

[29] M. G. Shirangi, E. Furlong, and K. S. Sims, "Digital twins for well planning and bit dull grade prediction," 2020, https://www.scopus.com/inward/record.uri?eid=2-s2.0-85086241879&partnerID=40&md5=5f6f37353a421844eaa263245179a32b.

[30] S. Mayakannan, R. Rathinam, R. Saminathan et al., "Analysis of spectroscopic, morphological characterization and interaction of dye molecules for the surface modification of TiB2Nanoparticles," *Journal of Nanomaterials*, vol. 2022, Article ID 1033216, 9 pages, 2022.

[31] M. Ulas, O. Aydur, T. Gurgenc, and C. Ozel, "Surface roughness prediction of machined aluminum alloy with wire electrical discharge machining by different machine learning algorithms," *Journal of Materials Research and Technology*, vol. 9, no. 6, pp. 12512–12524, 2020.

[32] G. Sathiaraj, R. Mani, M. Muthuraj, and S. Mayakannan, "The mechanical behavior of Nano sized Al2O3 -reinforced Al-Si7-Mg alloy fabricated by powder metallurgy and forging," *ARPN Journal of Engineering and Applied Sciences*, vol. 11, no. 9, pp. 6056–6061, 2016.

[33] P. Esch and F. Werner-Jäger, "Anwendung eines künstlichen Neuronalen Netzes zur Verschleißbestimmung von Zerspanwerkzeugen: KI-gerechte Datenaufbereitung zum Anlernen eines Neuronalen Netzwerks," *At-Automatisierungstechnik*, vol. 70, no. 7, pp. 635–645, 2022.

[34] F. Aydin, "The investigation of the effect of particle size on wear performance of AA7075/Al2O3 composites using statistical analysis and different machine learning methods," *Advanced Powder Technology*, vol. 32, no. 2, pp. 445–463, 2021.

[35] S. Thangaraj, G. M. Pradeep, M. S. Heaven Dani, S. Mayakannan, and A. Benham, "Experimental investigations on tensile and compressive properties of nano alumina and arecanut shell powder reinforced polypropylene hybrid composites," *Materials Today: Proceedings*, vol. 68, pp. 2243–2248, 2022.

[36] F. Aydin and R. Durgut, "Estimation of wear performance of AZ91 alloy under dry sliding conditions using machine learning methods," *Transactions of Nonferrous Metals Society of China*, vol. 31, no. 1, pp. 125–137, 2021.

[37] A. P. Sekhar and D. Das, "Influence of artificial aging on mechanical properties and high stress abrasive wear

behaviour of Al–Mg–Si alloy," *Metals and Materials International*, vol. 27, no. 2, pp. 337–351, 2021.

[38] B. Stalin, P. Ramesh Kumar, M. Ravichandran, M. Siva Kumar, and M. Meignanamoorthy, "Optimization of wear parameters using Taguchi grey relational analysis and ANN-TLBO algorithm for silicon nitride filled AA6063 matrix composites," *Materials Research Express*, vol. 6, no. 10, Article ID 106590, 2019.

[39] G. N. K. G Naveen Kumar etal, V. Mahidhar Reddy, M. Sunil Kumar, K. Hemachandra Reddy, and Y. V. Mohana Reddy, "Slurry erosive wear behavior of AA 6063/TIC particles in situ composites," *International Journal of Mechanical and Production Engineering Research and Development*, vol. 7, no. 3, pp. 223–232, 2017.

[40] S. Ilangovan, A. Shanmugasundaram, and S. Arul, "Influence of specimen temperature on wear characteristics of aa6063 aluminium alloy," *Journal of Surface Science and Technology*, vol. 32, no. 3–4, pp. 93–98, 2017.

[41] P. A. Sylajakumari, R. Ramakrishnasamy, and G. Palaniappan, "Taguchi grey relational analysis for multi-response optimization of wear in co-continuous composite," *Materials*, vol. 11, 9 pages, 2018.

[42] N. Kaushik and S. Singhal, "Examination of wear properties in dry-sliding states of SIC strengthened al-alloy metal matrix composites by using taguchi optimization approach," *International Journal of Applied Engineering Research*, vol. 12, no. 20, pp. 9708–9716, 2017.

[43] P. Kiss, D. Fonyo, and T. Horvath, "BlaBoO: a lightweight black box optimizer framework," in *Proceedings of the DISA 2018 - IEEE World Symposium on Digital Intelligence for Systems and Machines*, pp. 213–218, Slovakia, August 2018.

[44] T. M. Deist, F. J. W. M. Dankers, G. Valdes et al., "Machine learning algorithms for outcome prediction in (chemo)radiotherapy: an empirical comparison of classifiers," *Medical Physics*, vol. 45, no. 7, pp. 3449–3459, 2018.

[45] J. Gao, D. Nuyttens, P. Lootens, Y. He, and J. G. Pieters, "Recognising weeds in a maize crop using a random forest machine-learning algorithm and near-infrared snapshot mosaic hyperspectral imagery," *Biosystems Engineering*, vol. 170, pp. 39–50, 2018.

[46] W. Brendel, J. Rauber, and M. Bethge, "Decision-based adversarial attacks: reliable attacks against black-box machine learning models," 2018, https://www.scopus.com/inward/record.uri?eid=2-s2.0-85083954048&partnerID=40&md5=d2646cdf5c872ab2eaf5119b5338131f.

Hindawi
Journal of Chemistry
Volume 2023, Article ID 2245685, 17 pages
https://doi.org/10.1155/2023/2245685

Research Article

Green Synthesis by Microwave Irradiation of TiO_2 Using *Cinnamomum verum* and the Application in Photocatalysis

Dante E. González-Anota,[1] Silvia P. Paredes-Carrera,[1] Rosa M. Pérez-Gutierrez,[2] Brandon Arciniega-Caballero,[1] Raul Borja-Urby,[3] Jesús C. Sánchez-Ochoa,[1] and Elizabeth Rojas-García[4]

[1]*Laboratorio de Nanomateriales Sustentables, Escuela Superior de Ingeniería Química e Industrias Extractivas (ESIQIE), Instituto Politécnico Nacional (IPN), Unidad Profesional Adolfo López Mateos, Av. Instituto Politécnico Nacional S/N, Ciudad de México, CP 07708, Mexico*
[2]*Laboratorio de Productos Naturales, Escuela Superior de Ingeniería Química e Industrias Extractivas (ESIQIE), Instituto Politécnico Nacional (IPN), Unidad Profesional Adolfo López Mateos, Av. Instituto Politécnico Nacional S/N, Ciudad de México, CP 07708, Mexico*
[3]*Centro de Nanociencias y Micro y Nanotecnologías (CNMN), Instituto Politécnico Nacional (IPN), Unidad Profesional Adolfo López Mateos, Av. Luis Enbrique Erro S/N, Ciudad de México, CP 07708, Mexico*
[4]*Area de Ingeniería Química, Departamento de Ingeniería de Procesos e Hidráulica, Universidad Autónoma Metropolitana (UAM), Campus Iztapalapa, Ciudad de México, CP 09310, Mexico*

Correspondence should be addressed to Silvia P. Paredes-Carrera; silviappcar@gmail.com

Received 14 October 2022; Revised 21 November 2022; Accepted 3 April 2023; Published 12 May 2023

Academic Editor: B. R. Ramesh Bapu

The extraction process of bioactives from the aqueous extract of cinnamon (*Cinnamomum verum*) was optimized using the Design Expert 11 program and analysis of variance (ANOVA) by considering the following parameters: cinnamon weight (g), power (W), and time (s) of microwave irradiation. The optimal conditions are cinnamon weight of 4.5 grams, time of 600 seconds, and power of 150 watts of microwave irradiation. With *Cinnamomum verum* extract under optimal conditions and titanium (IV) tetrachloride as a precursor, TiO_2 nanostructures were synthesized using the sol-gel method assisted by microwave irradiation in the crystallization stage with a power and irradiation time of 150 W and 600 sec, respectively. Similarly, a sample without extract was synthesized under the same conditions. The following techniques characterized the materials: X-ray diffraction (XRD), Fourier transform infrared (FTIR) spectroscopy, UV-vis diffuse reflectance, Raman spectrometry, and high-resolution transmission electron microscopy (HRTEM). It was feasible to obtain nanocrystalline solids of TiO_2 anatase phase with and without cinnamon extract; the particle size and the crystallinity were influenced by the bioactive agents during the synthesis (aqueous extract of *Cinnamomum verum*) and the synthesis method (microwave irradiation); a smaller crystal size, a smaller particle size, a higher crystalline order, and a lower band gap were achieved for the material synthesized with cinnamon extract compared to the material synthesized without extract and other methods. The synthesized materials were evaluated in the photodegradation of methyl orange (as a model of photodegradation), employing as reference parameters the commercial TiO_2 brand Sigma-Aldrich phase anatase and the photolysis of the system. The amount of dye adsorbed in the tested materials was quantified, finding an equilibrium time of 15 min, where the TiO_2 synthesized with *Cinnamomum verum* extract was the material that most adsorbed methyl orange at 7.5%. In the case of photodegradation, the TiO_2 synthesized with cinnamon extract apparently promoted the total mineralization of methyl orange in 40 minutes of reaction, making it the best material of those evaluated in the photodegradation. In all cases, the degradation models were adjusted to a first-order kinetic model, where it was confirmed that the highest reaction rate corresponded to TiO_2 synthesized with *Cinnamomum verum*.

1. Introduction

The generation of nanomaterials through green synthesis uses low-cost sustainable methodologies with low or zero emission of waste and toxic by-products [1, 2] as an alternative to existing synthesis methods such as coprecipitation, solvothermal, and the sol-gel method, among others, that require a high energy expenditure and purification and generate toxic by-products and waste for the environment [3].

In green synthesis, natural sources such as microorganisms (bacteria, fungi, and yeasts), extracts of plants (flowers, stems, and leaves), or products of metabolism or parts of them (enzymes) are used [4, 5]. Natural extracts contain bioactive compounds present in plants, such as alkaloids, polyphenols, terpenoids, antioxidants, sugars, flavonoids, organic acids, and quinones, together with low molecular weight proteins [6] which can be used in the reduction of precursor agents for the synthesis of nanomaterials [4, 7] because they act as electron donors [8], stabilizers, and capping agents [9–11]. Coating agents prevent coagulation and spontaneous flocculation of the precursors and intermediate products during the synthesis processes through electrostatic interaction [12].

A viable biological material for the green synthesis of nanomaterials is cinnamon (*Cinnamomum verum*) due to its high content of bioactive compounds such as aldehydes, alcohols, esters, acids, monoterpenes, diterpenes, sesquiterpenes, benzopyrenes, hydrocarbons, flavonoids (procyanidin dimers type A and B), and phenolic compounds (eugenol and pyrogallol). Previous studies have shown that the aqueous extract of *Cinnamomum veru*m has high antioxidant activity [13, 14], which suggests its application in the synthesis of nanomaterials as an effective reducing agent for metallic particles and promoting chemical processes such as hydrolysis [15]; in addition, no reported applications for the synthesis of nanomaterials were found for this compound.

The nanomaterial employed in this work was titanium dioxide (TiO_2), with high photocatalytic activity (>50–80% in 2 H) [16, 17] and can be found in three crystalline structures: anatase, rutile, and brookite [18]. The anatase phase is the one with the highest photoactivity [19]. However, although TiO_2 is an excellent photocatalytic material, it also has some drawbacks since it has a limited absorption in the visible spectrum with a band gap of 3.2 eV [20], mainly absorbing UV radiation, with a high recombination rate of electron-hole pairs and presenting photo corrosion which decreases its photocatalytic efficiency. For this reason, various works [21–23] have sought to generate a change in the band pap, morphology, texture, and/or particle size [20, 24]. This is through doping (with noble metals such as silver and gold), coupling it to other semiconductors and/or materials such as graphene (composites and hybrid materials), with morphosynthesis (polymeric templates), and/or obtaining with different synthesis methodologies and precursors [25, 26]. This is where microwave-assisted green synthesis provides a viable and novel technology.

Microwave irradiation has been implemented in the search for methodologies that represent a lower energy expenditure and allows the manipulation of properties such as the texture and morphology of nanoparticles [27]. Microwaves are a type of electromagnetic radiation between 0.3 and 300 GHz; the heating mechanism involves two main processes: dipolar polarization and ionic conduction. Irradiation of a sample with microwaves results in the alignment of the dipoles or ions in the electric field. Because electromagnetic radiation produces an oscillating field, the dipoles or ions continually try to realign themselves in the electric field. Depending on the oscillation phenomena in relation to the frequency of the irradiation, different amounts of heat are produced through molecular friction and dielectric loss [28, 29]; this superheat allows a fast reaction speed, reproducibility, and control of the morphology and texture depending on the parameters of power and irradiation time [28, 30], which makes it a suitable irradiation source both for the extraction of bioactive compounds and for the synthesis of nanomaterials [30–32].

Methyl orange was used as a photodegradation model for the synthesized materials [33, 34], belonging to the azo dyes, and these constitute between 60 and 70% of the dyes used in the industry, being one of the most important contaminants that reproduce in the environment [35–37]. It is worth mentioning that the objective of this research is focused on the properties of TiO_2 synthesized by green synthesis by microwave irradiation of TiO_2 using *Cinnamomum verum* and its potential application, constituting a starting point for future work. The quantification of the percentage of methyl orange degradation was evaluated by UV-vis spectroscopy (467 nm).

On the other hand, the optimization of the aqueous extract of *Cinnamomun verum* was carried out using the Box–Behnken Design (BBD) model, which is one of the methods for predicting response surface methodologies (RSMs). This model has its origin from the graphic perspective and an adjustment through empirical models. The response surface methodology (RSM), introduced by George E. P. Box and K. B. Wilson in the early 1950s, consists of the collection of statistical and mathematical techniques useful for modeling and analyzing experimental data, which determine the effects and response of quantitative variables to identify the optimal point. The advantage is the decrease in the number of experiments to evaluate their independent variables, and the disadvantage is the inability to provide a global optimal point. The RSM largely uses the BBD response surface, which is suitable for fitting quadratic and cubic models and is feasible to investigate and optimize variables in the experimental space with the fewest number of experiments without being an expert in statistics. The central composite design (CCD) is based on the same criteria as BBD; however, the main difference between them is the number of star points or center points in the experimental space, which gives CCD more points and, therefore, more experiments. Compared to the "one-variable-at-a-time" approach and the full factorial design, the BBD has more advantages due to the reduced number of experiments [38–46].

In this work, we sought to obtain photocatalytic nanomaterials such as TiO_2 via green synthesis by the sol-gel method assisted with microwave irradiation of the TiO_2 type through the use of bioactive compounds from the aqueous extract of *Cinnamomum verum,* which were optimized using the RSM statistical technique, with the premise of obtaining efficient and economically sustainable nanomaterials that improve the photocatalytic processes.

2. Experimental

2.1. Chemicals. The reagents used for the preparation of the precursor solutions for the extraction of bioactives from cinnamon and TiO_2 synthesis were as follows: $TiCl_4$Sigma-Aldrich 99.9%, $C_{14}H_{14}N_3O_3SNa$ Sigma-Aldrich 99.9%, C_2H_5OH Sigma-Aldrich 98%, TiO_2Sigma-Aldrich 99.5%, and Caledon brand bidistilled, tridistilled, and deionized water.

2.2. Cinnamomum verum Aqueous Extract Optimization. Cinnamomum verum aqueous extract optimization by microwave irradiation was performed with the use of Design Expert software (Version 8.0.6, Stat-Ease Inc., Minneapolis, MN, USA). It employs the BBD as an algorithm, which is one of the methods for predicting response surface methodologies (RSMs) to examine the relationship between one or more response variables and a set of quantitative experimental parameters. The optimization was made using three independent variables and one response variable, with 17 runs to optimize the extraction conditions of bioactive (Table 1). Aqueous extracts of *Cinnamomum verum* were obtained in an SBL CW-2000A microwave reactor. The three independent variables were as follows: the weight of *Cinnamomum verum* (1.5, 3.0, and 4.5 g) with deionized water, microwave irradiation time (300, 600, and 900 s), and microwave irradiation power (150, 250, and 350 W); the response variable was the weight of the *Cinnamomum verum* extract. Regression analysis was made according to the experimental data, and the second-order polynomial model (equation (1)) was fitted to express the amount of extract obtained through the **AN**alysis **O**f **VA**riance (ANOVA) [47].

$$Y = a_0 + \sum_{i=1}^{3} a_i X_i + \sum_{i=1}^{3} a_{ii} X_i^2 + \sum_{i \neq J=1}^{3} a_{ij} X_i X_j, \qquad (1)$$

where Y is the amount of *Cinnamomum verum* extract, a_0 is the intersection (constant), $?_1X_1$ to $?_3X_3$ are linear coefficients, $a_{11}X_1^2$ to $a_{33}X_3^2$ are quadratic coefficients and interaction coefficients, X_1 is the weight of the *Cinnamomum verum* (g), X_2 is microwave irradiation power (W) y, and X_3 is the microwave irradiation time (s).

2.3. Green Synthesis of TiO_2 Nanoparticles by the Sol-Gel Method Assisted by Microwave Irradiation and Cinnamomum verum Extract as Reductant. In the synthesis of TiO_2 nanoparticles (a code **C-TiO$_2$** was assigned) using the sol-gel method assisted by microwave irradiation, 100 ml of *Cinnamomum verum* extract (prepared according to optimal results) was added to a flanged reactor, and the equivalent of 5% $TiCl_4$ was added dropwise, keeping the system under constant agitation for 40 minutes in a cryogenic bath at 4°C. Finally, the mixture was introduced into the SBL CW-2000A microwave reactor and irradiated for 10 minutes at 150 W. Washes were performed by centrifugation with a 1: 1 ethanol-water mixture at 15 000 rpm at room temperature for 15 minutes. The precipitate was dried in a convection oven for 5 hours at 70°C, and the resulting material was calcined for 4 hours at 450°C with a heating ramp of 30 minutes at 10°C·min^{-1}. The procedure was repeated without extract, and the code **CO-TiO$_2$** was assigned to this sample. It is worth mentioning that in the evaluation, Sigma-Aldrich brand TiO_2 was used as a reference, which was identified as **A-TiO$_2$**.

2.4. Characterization of the Samples. The synthesized compounds were characterized by X-ray diffraction (XRD), Fourier transform infrared spectroscopy (FTIR), UV-vis diffuse reflectance spectroscopy (UV-vis), Raman spectroscopy, and High-resolution transmission electron microscopy (HRTEM). The XRD spectra were obtained on a PANalytical model X'Pert PRO diffractometer for thin films or crystalline coatings ($\lambda = 1541$ Å), and the infrared spectra were obtained on a Nicolet Magna-IR 550 spectrometer in a range of 4000 – 650 cm. UV-vis spectra were obtained via a Cary 100 UV-vis spectrophotometer, with an integrating sphere (Labsphere DRA-CA-30) and was operated over a wavelength interval between 200 and 800 nm. Raman spectra were recorded at ambient temperature on a Raman Thermo Nicolet Almaga between 100 cm^{-1} and 1000 cm^{-1} with an exposure time of 1 s; the emission wavelength was 532 nm, and a nominal power of 25 mW was applied with a Nd: YVO4 laser. HRTEM and BFTEM micrograms were obtained in a transmission electron microscope JEOL brand JEM-ARM200CF model at 200 kV.

2.5. Evaluation of the Adsorption-Photodegradation of Methyl Orange

2.5.1. Adsorption of Methyl Orange. The materials were left in the dark in contact with the 3 ppm solution of methyl orange and found that the equilibrium time was 15 min. The adsorption of methyl orange was quantified in a Perkin Elmer brand UV-vis Lambda XLS spectrophotometer at a wavelength of 467 nm. After the adsorption, the materials were subjected to the photodegradation process.

2.5.2. Photodegradation of Methyl Orange. The process was carried out in 15 ml vials in triplicate for each point. 10 ml of methyl orange at 3 ppm and 0.1 g of C-TiO_2 were added to each vial; the resulting suspensions were subjected to UV light irradiation in a Luz Chem brand photoreactor equipped with 2 Philips 125 W UV lamps and an agitation system. Every 10 minutes, 5 ml aliquots were taken in triplicate until reaching equilibrium (100 minutes of reaction), and each aliquot was filtered with a 45 μ hydrophobic membrane. The concentration of degraded methyl

Table 1: Optimization by Design Expert software of aqueous extracts of *Cinnamomum verum*.

Runs	Independent variables			Response variable
	X_1 Weight of *Cinnamomum verum* (g)	X_2 Microwave irradiation power (W)	X_3 Microwave irradiation time *(s)*	Weight of *Cinnamomum verum* extract (g)
1	3.0	350	300	0.0582
2	1.5	150	600	0.0617
3	4.5	150	600	0.0902
4	3.0	350	900	0.0453
5	1.5	350	600	0.0406
6	1.5	250	300	0.0610
7	3.0	250	600	0.0535
8	3.0	250	600	0.0521
9	4.5	350	600	0.0706
10	3.0	250	600	0.0558
11	3.0	150	300	0.0511
12	1.5	250	900	0.0440
13	4.5	250	300	0.0673
14	3.0	150	900	0.0607
15	3.0	250	600	0.0542
16	4.5	250	900	0.0596
17	3.0	250	600	0.0533

orange was quantified in a Perkin Elmer brand UV-vis Lambda XLS spectrophotometer at a wavelength of 467 nm. The above procedure was repeated for the CO-TiO_2 and A-TiO_2 photocatalysts and the photolysis.

3. Results and Discussion

3.1. Cinnamomum verum Aqueous Extract Optimization. According to Table 1, the highest amount of extracts was obtained for run number 3 with 0.0902 g of bioactive, with 4.5 g of ground cinnamon, power of 150 W, and microwave irradiation time of 600 s, followed by runs 9 and 13, and the one that obtained the least amount of cinnamon extract was run 5. ANOVA results considering the second-order polynomial model of the 17 runs are shown in Tables 2 and 3.

ANOVA results predicted a quadratic model (equation (2)) for the three independent variables (weight of *Cinnamomum verum*, microwave irradiation time, and microwave irradiation power). The results in Table 2 suggested that the generated model had a high value of the coefficient of determination R squared (0.8283). The results in Table 3 indicate that the model had a high F value (3.75) and a low p value (0.0476) for the response indicating that the quadratic model is significant. This suggests that the model could predict 82% of the variations in the experimental data. In this sense, the quadratic model is significant during microwave extraction.

The analysis of variance (ANOVA) determined the following second-order polynomial model:

$$\begin{aligned} Y = {} & 0.08 - 0.018X_1 - 1.52E10^{-4}X_2 + 0.71EX_3 \\ & + 2.5E10^{-6}X_1X_2 + 5.16E10^{-6}X_1X_3 - 1.87EX_2X_3 \\ & + 3.58E10^{-3}X_1^2 + 3.92E10^{-7}X_2^2 - 4.30EX_3^2. \end{aligned} \quad (2)$$

Table 2: Predicted and experimental values of the responses were obtained under optimal extra extraction conditions.

Predicted model	Sum of squares	Df	R^2
Quadratic	0.0018	9	0.8283

Df: degree of freedom and R^2: coefficient of determination.

The analysis of the response surface and contour is shown in Figure 1. 3D dimensional graphs were obtained by the ANOVA for the 17 runs, and the relationship of the independent and dependent variables was studied for getting the *Cinnamomum verum* extract.

The analysis of the response surface and contour of the weight of the *Cinnamomum verum* extract shows the effect of these independent variables. It can be seen in the response surface graphs that the best results for the weight of the *Cinnamomum verum* extract tend to be red color, that is, lower microwave irradiation powers produce higher cinnamon extract weights, and the lowest value on the blue scale with higher irradiation power and lower *Cinnamomum verum* weights produces the lowest cinnamon extract weights (Figures 1(a)–1(c)).

When comparing the same weight of cinnamon and microwave irradiation power at different irradiation times at (A) 300 sec, it can be seen that the best results in terms of the greater amount of extract obtained tend to have higher cinnamon weights (4.5 g) and low microwave irradiation powers (150 W). In the case of (B) 600 sec and (C) 900 sec, the same trend can be observed. In general, the increase of the microwave irradiation time during the extraction of the bioactives promotes a decrease in the amount of extract obtained due to the degradation effect.

Preferably, when comparing the same weight of cinnamon and microwave irradiation power, the degradation of the resulting bioactives is promoted as the irradiation time increases.

Table 3: ANOVA statistics of quadratic models for the extraction yields of the weight of the *Cinnamomum verum* extract.

Source	Mean square	*F*-value	*p* value	*Significant
Model (quadratic)	0.0018	3.75	0.0476	Significant

F-value: Fisher-Snedecor distribution value, *p* value: probability value, *significant ($p < 0.05$).

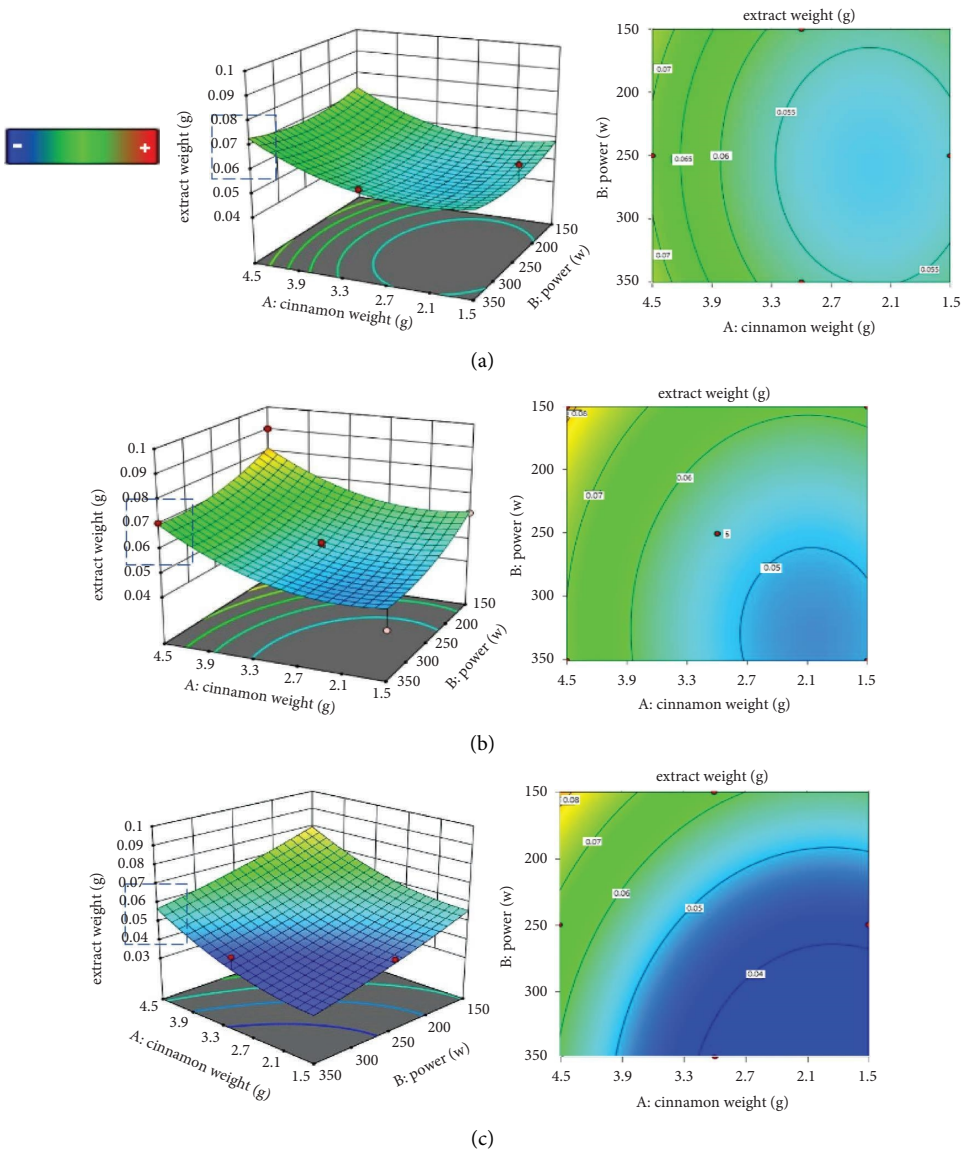

Figure 1: Analysis of response surface (ARS) and analysis of response contour, respectively: weight of *Cinnamomum verum*, microwave irradiation power vs. weight of *Cinnamomum verum* extract: (a) 300 sec, (b) 600 sec and (c) 900 sec of microwave irradiation.

Figure 2 shows the Pareto diagram, prepared with the variables X_1, X_2, and X_3 and the frequency of the response variable (amount of the *Cinnamomum verum* extract) for the 17 experiments proposed by the Design Expert program.

Based on the 80/20 Pareto principle to establish priorities in obtaining the greatest amount of the *Cinnamomum verum* extract, it corroborates the trend of the ARS graphs; that is, the greatest amount of the extract is obtained towards

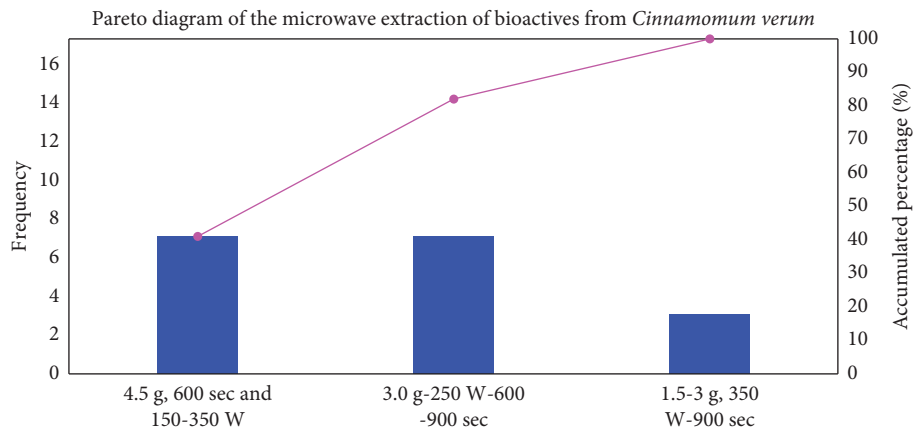

Figure 2: The Pareto diagram of the microwave extraction of bioactives from *Cinnamomum verum*.

greater weights of cinnamon (4.5 g), at low microwave irradiation powers (150 W) and an irradiation time of 600 sec [48–51].

3.2. X-Ray Diffraction (XRD). Figure 3 shows the normalized X-ray diffraction patterns of the C-TiO_2 and CO-TiO_2 samples.

Based on the JCPDS (Joint Committee on Powder Diffraction Standards) library, it can be seen that in all cases, the characteristic reflections of the anatase phase were obtained at $2\theta = 25.3$, 38.5, 48.03, 55.0, 62.11, 68.76, 75.05, and 82.16° (JCPD letter 00-021-1272) corresponding to a tetragonal unit cell. The CO-TiO_2 sample synthesized without the extract has a reflection attributed to the brookite phase (JCPD letter 01-075-2548) at $2\theta = 31°$ (B), and for the C-TiO_2 sample, two reflections are observed at $2\theta = 28$ and 42° (R) identified for the rutile crystallographic phase (JCPD letter 00-021-1276), where the commercial sample A-TiO_2 is the lowest crystallinity. Comparing the intensity of the reflections (1 0 1), (1 0 3), (2 0 0), and (1 0 5) shows that the CO-TiO_2 sample is more ordered than the C-TiO_2 sample. The crystal size was determined by the Debye–Scherrer equation. The sample synthesized by microwave and the aqueous extract of *Cinnamomum verum* (C-TiO_2) presented a smaller crystal size (1.96 nm) than the one synthesized without extract CO-TiO_2 (2.35 nm), which indicates that the phenolic and flavonoid compounds contained in the cinnamon extract promote a smaller crystal size and improve the crystallinity since both samples were synthesized under the same microwave irradiation conditions [52]. Also, the reaction time is reduced from hours to minutes (10 minutes) during the synthesis of materials with the use of microwaves.

3.3. Fourier Transform Infrared (FTIR) Spectroscopy. Figure 4 shows the absorption bands of the functional groups present in TiO_2, obtained by Fourier transform infrared (FTIR) spectroscopy for samples A-TiO_2, C-TiO_2, CO-TiO_2, and the aqueous extract of cinnamon.

In the cinnamon extract, it is possible to observe the signal corresponding to the ⁻OH bonds of the phenolic compounds of the extract at 3244 cm^{-1}. At 2922 cm^{-1}, the

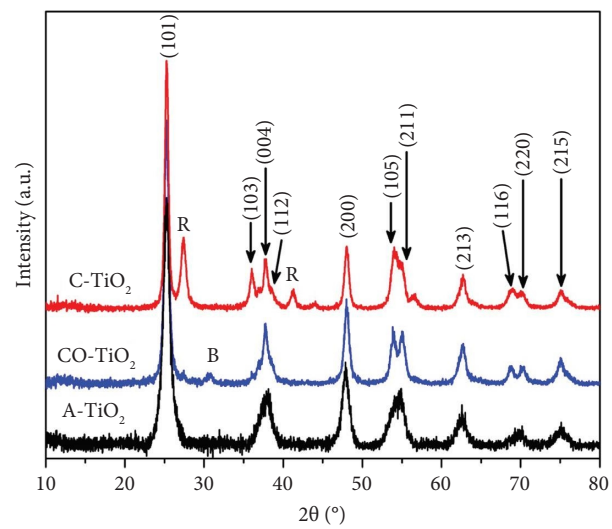

Figure 3: X-ray diffraction patterns of the C-TiO_2 and CO-TiO_2 samples. Rutile (R), and brookite (B) phases.

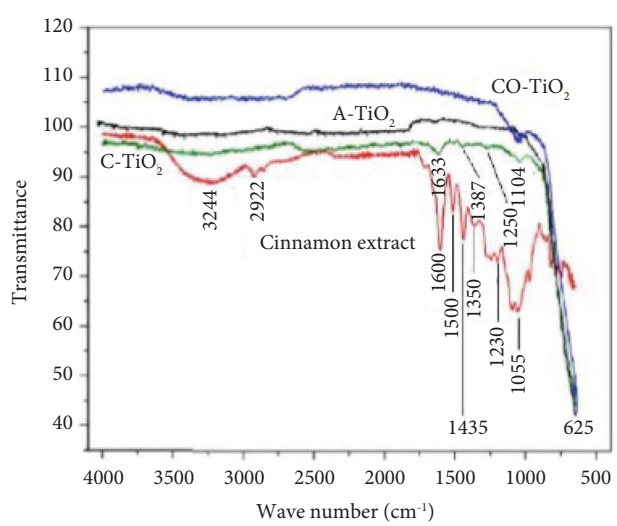

Figure 4: FTIR spectra of the samples A-TiO_2, C-TiO_2, CO-TiO_2, and the aqueous extract of cinnamon.

signal for the C-H bond of the methylene group corresponds to terpenes. The phenolic compounds appear with the absorption bands for $^{-}$COOH bonds at 1350 cm^{-1}, for C-O at 1230 and 1055 cm^{-1}, and for the flavonoids, the signals for aromatic C=O bonds are presented at 1600 cm^{-1} with its harmonics at 1500 and 1435 cm^{-1}. This indicates that the extract of *Cinnamomum verum* is composed of phenolic compounds, terpenes, and flavonoids, which have been reported to be able to promote the synthesis of TiO_2 [53].

In the case of the C-TiO_2 and CO-TiO_2 samples, the signal at 1104 cm^{-1} indicates the distribution of TiO_2 nanoparticles in the anatase phase; this has already been reported by Raghunandan et al. [54]. The additional signals that appear in the C-TiO_2 sample at 1633, 1387, and 1250 cm^{-1} could correspond to remnants of the extract.

3.4. High-Resolution Transmission Electron Microscopy. Figure 5 shows the images by bright-field micrographs (BFTEM) at different magnifications for the commercial samples A-TiO_2 (A and D) and the samples synthesized by microwave irradiation in 10 min: CO-TiO_2 (B and E) and C-TiO_2 (C and F).

At 20 and 10 nm scales, it can be seen that the sample synthesized with the *Cinnamomum verum* extract C-TiO_2 (C and F) is the one with the smallest particle size and with regular hemispherical shapes with an approximate size of 15 nm, followed by the synthesized sample without the extract CO-TiO_2 (B and E) with semielliptical irregular shapes and sizes from 20 to 40 nm and the commercial A-TiO_2 (A and D) with the least uniform shape and particle size ranging from 20 to 50 nm. At magnifications of 10 nm, it can be seen that the samples synthesized with microwaves CO-TiO_2 (E) and C-TiO_2 (F) planes of atoms with preferential orientation are observed.

Figure 6 shows the images by high-resolution transmission electron microscopy (HRTEM) at different magnifications of the C-TiO_2 sample: (A) 5 nm, (B) 1.5x, and (C) 5x. Additionally, the diffraction pattern obtained by TEM is shown in (D).

The digital enlargement of the microgram of a C-TiO_2 nanoparticle is shown (Figure 5(b)), in which the crystal lattice of this material can be observed, and the top view of the unit cell can be seen (Figure 5(c)), which corresponds to the tetragonal crystal system (marked in yellow) corresponding to the anatase phase for TiO_2, according to what was found by XRD. Therefore, the use of the aqueous extract of *Cinnamomum verum* during the synthesis assisted by microwave irradiation with titanium precursor ($TiCl_4$) promoted nanoparticles of uniform nanometric size (approximately 15 nm in diameter) with a high degree of crystallinity and preferential anatase phase. The diffraction pattern of the C-TiO_2 sample (Figure 5(d)) indicates that a polycrystalline sample of TiO_2 nanoparticles was obtained, confirming the polycrystalline nature of the material as shown in the HRTEM images (Figure (A)) [55–57].

3.5. UV-Vis Diffuse Reflectance Spectroscopy. Based on the diffuse reflectance data, it is possible to determine the optical band gap (Eg) of the A-TiO_2, C-TiO_2, and CO-TiO_2 samples using the Kubelka–Munk equation and the Tauc graphs following the formula: $\alpha h\nu = A\ (h\nu - \mathrm{Eg})^{n/2}$ for semiconductors [58–60]; these values are represented in Figure 7.

The samples synthesized by microwave irradiation with C-TiO_2 and without the CO-TiO_2 extract have a band-gap value of 3.42 and 3.67 eV, respectively, both being higher than the commercial sample A-TiO_2 brand Sigma-Aldrich (3.19 eV), which would indicate in the theory that to photoactivate the C-TiO_2 and CO-TiO_2 samples with UV light, more energy will be required, whereas the commercial sample (A-TiO_2) needs less energy to be photoactivated by UV light.

The TEM images show that the CO-TiO_2 sample has sizes between 20 and 40 nm (Figures 5(b) and 5(e)) with a band gap equal to 3.67 eV. In the case of the sample synthesized by cinnamon C-TiO_2 of 15 nm (Figures 5(c) and 5(f)), its band-gap value decreases to 3.42 eV, which indicates that there is a correspondence between the particle size and the band-gap value. This is attributed to the effect of quantum confinement of the material promoted by miniaturization, having a greater uptake of UV light absorption for the sample synthesized with the *Cinnamomum verum* extract.

3.6. Raman Spectroscopy. In Figure 8, the Raman spectra of the C-TiO_2 and CO-TiO_2 samples are presented.

In all cases, the vibrations that characterize the typical tetragonal structure of the anatase phase can be seen; the signal that appears at 450 cm^{-1} can be attributed to traces of the rutile crystallographic phase with a face-centered cubic structure, according to what is indicated in the X-ray diffraction spectra in the reflections at 28 and 42° (Figure 1) [61, 62]. The vibrations at 144 and 639 cm^{-1} are generated by the symmetric stretching of the O-Ti-O bond; the vibration at 399 cm^{-1} is caused by the symmetric bending of the O-Ti-O bonds; the vibration at 519 cm^{-1} was generated by the asymmetric bending in the O-Ti-O bond, sending signals that confirm the anatase phase as predominant in all cases [63, 64].

In Figure 9, we present a reaction proposal for the synthesis of TiO_2 using the *Cinnamomum verum* extract, based on what was proposed for the sol-gel method by Rojas et al. [65].

The synthesis of TiO_2 needs an abundance of $^{-}$OH ions; on the other hand [66], the bioactives contained in the *Cinnamomum verum* extract (mainly flavonoids and phenolic compounds) contain numerous $^{-}$OH groups in their structure [67–69], which efficiently promote a nonstable polymeric structure by hydrolysis generating $Ti(OH)_4$ and HCl, where the use of the aqueous extract of cinnamon contributes to the nucleation and growth of the polymeric phase. The resulting mixture was washed to remove HCl and

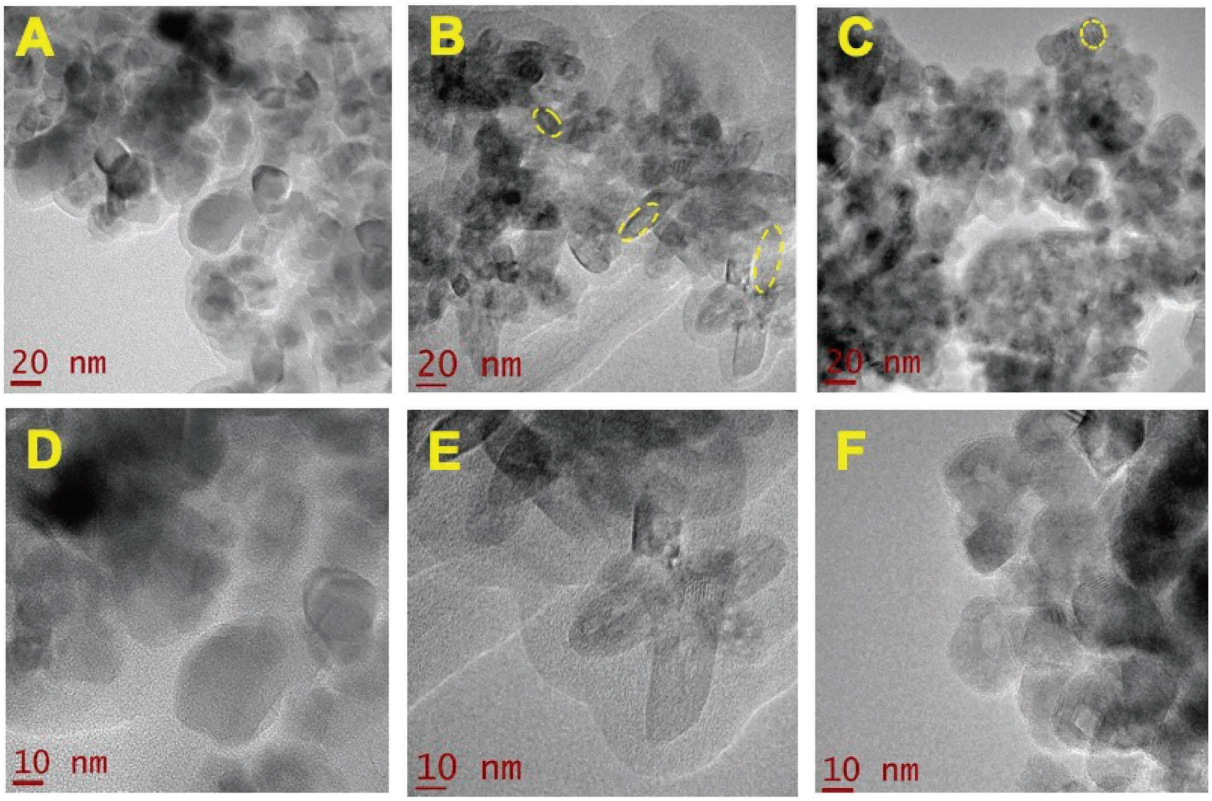

Figure 5: Bright-field transmission electron microscopy (BFTEM) micrograms for the samples: A-TiO_2 (a, d), CO-TiO_2 (b, e), and C-TiO_2 (c, f).

calcined (450°C for 4 h); after calcination, the tetragonal crystallographic structure was generated, and that corresponds to the anatase phase for the nanometric TiO_2 (Figure 7), which has a smaller particle size, more uniform size, and crystallinity than the rest of the materials evaluated (CO-TiO_2 and A-TiO_2).

3.7. Evaluation of the Adsorption-Photodegradation of Methyl Orange. Figure 10 shows the profile with the adsorption-photodegraded percentages of methyl orange at the optimal conditions for the samples C-TiO_2, CO-TiO_2, and A-TiO_2 and the photolysis (without catalyst) of the system at 3 ppm of contaminant with adsorption (15 min (a)) and degradation (100 min (b)) time of equilibrium, respectively, using a ratio of 1 g of catalyst per liter of methyl orange.

According to Figure 10(a), the sample synthesized with the *Cinnamomum verum* extract (C-TiO_2) is the one with the highest percentage of adsorption (7.5%), reaching equilibrium time experimentally in 15 min, followed by the C-TiO_2 sample (4.7%) and A-TiO_2 (1.76%). 10(b) The percentages of photodegradation for photolysis and samples A-TiO_2, CO-TiO_2, and C-TiO_2 with 100 min of UV irradiation resulted in 34.22, 81.42, 95.56, and 100%, respectively. The C-TiO_2 sample, synthesized with an aqueous extract of cinnamon (*Cinnamomum verum*), completely photodegraded methyl orange (100%) in just 40 minutes, reaching equilibrium at this time, unlike the rest of the experiments.

Figure 11 shows a comparison of the percentages of adsorption-photodegradation with all the materials evaluated with an exposure of 40 min.

The photolysis after 40 minutes only reaches up to photodegradation of 12.95%, followed by the A-TiO_2 sample (commercial) with 36.97%. For the samples synthesized with $TiCl_4$, with the aqueous extract of *Cinnamomun verum* and microwave irradiation (C-TiO_2), there is an improvement of 52.22% of methyl orange photodegradation when compared with CO-TiO_2. This can be attributed primarily to the fact that the band gap for the C-TiO_2 sample (Eg = 3.42 eV) is lower than that for the CO-TiO_2 sample (Eg = 3.67 eV), indicating that less energy is required to pass electrons from the valence band to the conduction band. In addition, the particle size was smaller, and the crystallinity was higher than the synthesized sample without extract; therefore, the active sites of the catalyst were better exposed than the sample synthesized without the extract. Other authors have found that there could be traces of the bioactives used as precursors (corroborated by FTIR, Figure 3), which could additionally have a photochromic effect and facilitate the photoreaction [66]. Additionally, when quantifying the adsorption of the dye, it can be seen that the resulting

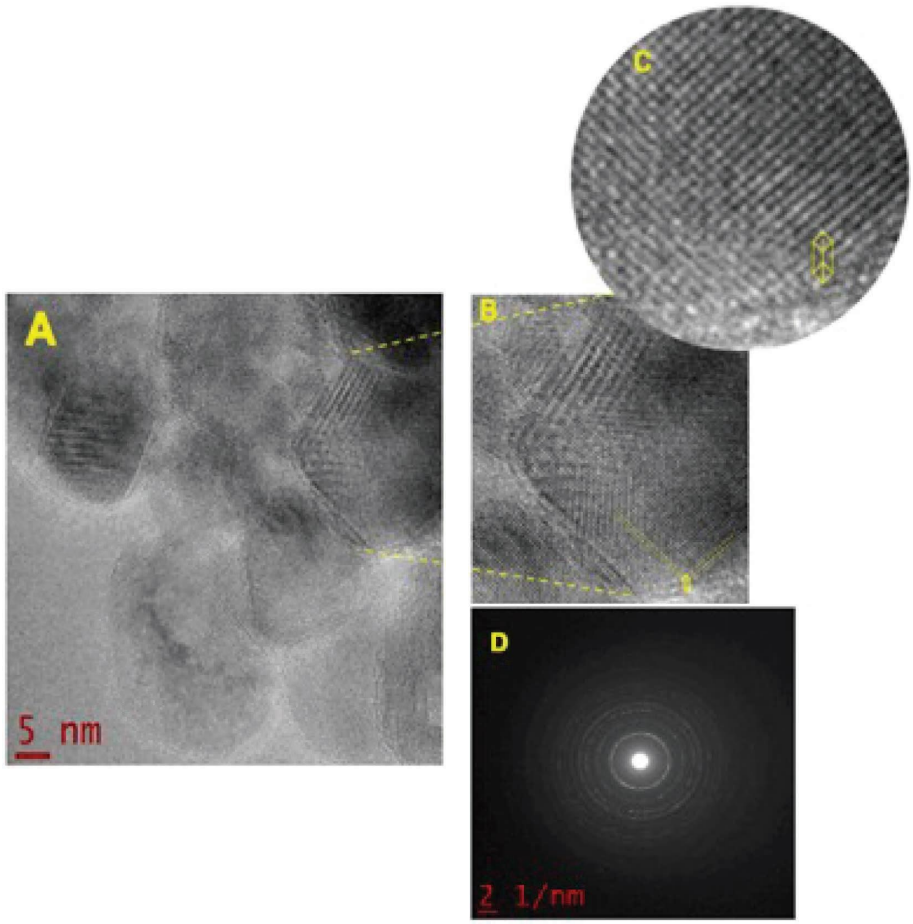

Figure 6: Micrograms by high-resolution transmission electron microscopy (HRTEM) for the C-TiO_2 sample at (a) 5 nm, (b) 1.5x, and (c) 5x. (d) Diffraction pattern obtained by TEM.

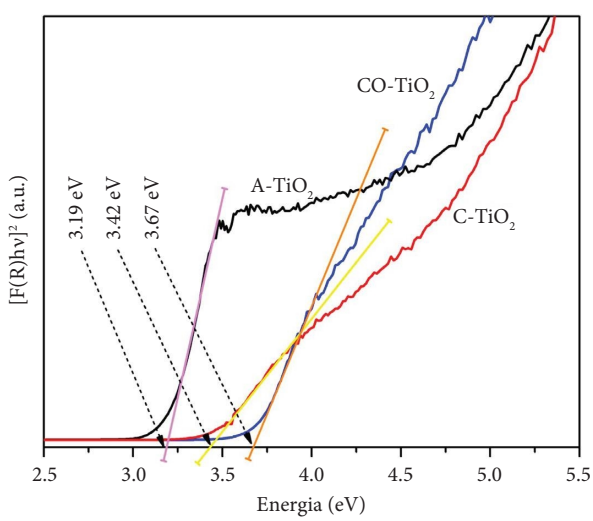

Figure 7: Diffuse reflectance spectra for A-TiO_2 photocatalysts, C-TiO_2, and CO-TiO_2.

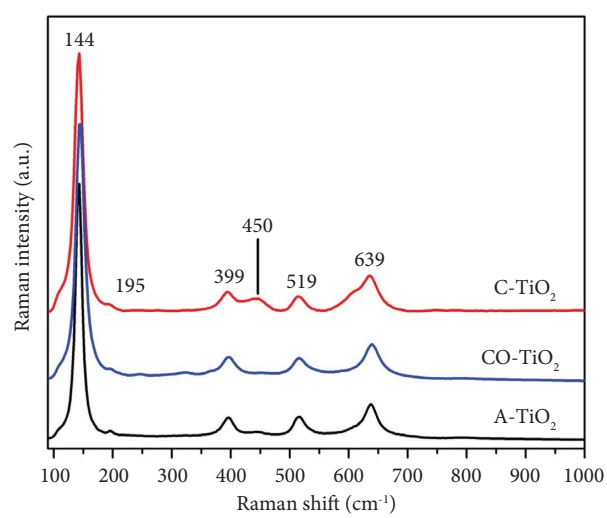

Figure 8: Raman spectra of the C-TiO_2 and CO-TiO_2 samples.

morphology for the C-TiO_2 sample allowed a better interaction of the catalyst with the reaction medium, contributing to the photodegradation (Figure 5(f)).

In the comparison of the C-TiO_2 (15 nm) and A-TiO_2 (50 nm) samples, the smaller particle size of the sample prepared with extract allowed for the exposure of a greater number of active sites in photodegradation, in addition to

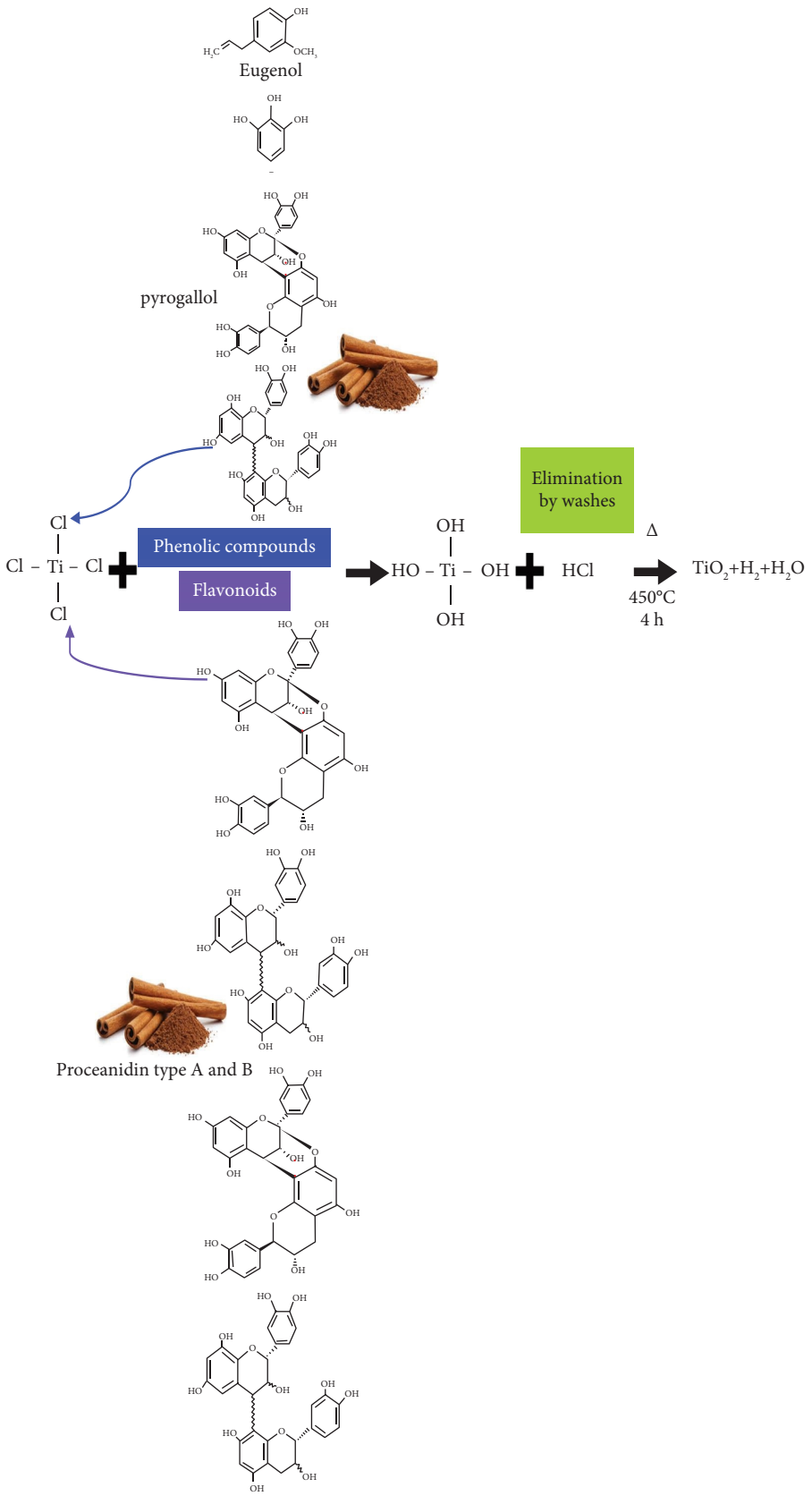

Figure 9: Reaction proposal to obtain nanometric TiO_2 using the *Cinnamomum verum* extract.

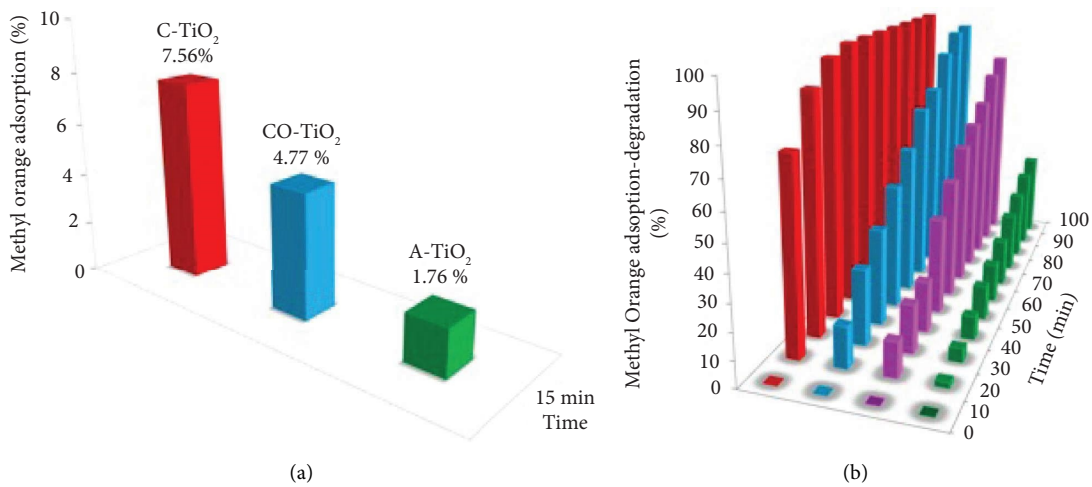

Figure 10: Methyl orange adsorption-photodegradation profiles, with 15 minutes (a) of adsorption and 100 minutes (b) of photodegradation for the samples CO-TiO_2, C-TiO_2, A-TiO_2, and the photolysis of the system.

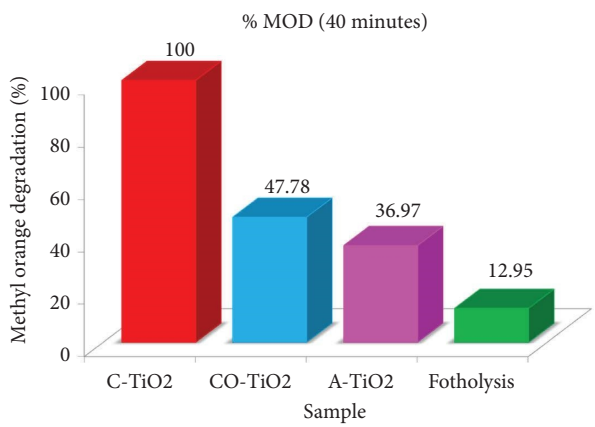

Figure 11: Percentage of adsorption-photodegradation of methyl orange (% MOD) at 40 minutes of reaction for the samples CO-TiO_2, C-TiO_2, A-TiO_2, and the photolysis of the system.

the already mentioned photochromic effect. Therefore, the sample synthesized with the aqueous cinnamon extract, despite having a higher band gap (Eg = 3.42 eV), was more photoactive than the commercial sample (Eg = 3.19 eV).

Figure 12, (A) shows the values obtained for the constant rate (k (min^{-1})) and the order (n) of the reaction calculated for the adsorption-degradation of methyl orange. Sections (B) to (C) present the speed profiles ($-r_{\text{methyl orange adsorption-degradation}}$) for the evaluated samples.

In all cases, the adjustment of the speed model (ppm methyl orange/min) corresponds to order one ($n = 1$), where the speed constants (k) resulted in values of $k = 0.89$, 0.021, 0.012, and 0.003 min^{-1} for the samples C-TiO_2, CO-TiO_2, A-TiO_2, and the photolysis of the system, respectively, with R^2 settings between 0.89 and 0.99 (Figure 12(a)). These values can be corroborated in the speed profiles (Figures 12(b) and 12(c)), where the sample synthesized with the *Cinnamomum verum* extract is the one with the highest speed according to the highest value of k of the tested materials, which shows the excellent interaction of TiO_2 with the reaction medium, attributable to the higher adsorption of methyl orange in the C-TiO_2 sample; therefore, the C-TiO_2 sample has smaller crystal size, smaller particle size, higher crystallinity, and smaller band gap than the one synthesized without cinnamon.

Figure 13 shows the UV-vis spectra obtained for the remnants of the sorption photodegradation of methyl orange to identify intermediate products, using the semiconductor CO-TiO_2 (%MOD = 95.56), that did not reach total mineralization after 40 and 100 min of photodegradation.

In the spectrum at the beginning of the reaction (0 min), two signals are presented. The first is located at $\lambda = 466$ nm, which is indicative of the chromophore group -N=N- (azo); the second signal at $\lambda = 269$ nm is associated with the benzene rings in the methyl orange structure. After 40 min of irradiation with UV light, the signal at 466 nm reduces its intensity, and after 100 min of irradiation, it disappears; this indicates the breaking of the -N=N group bond [70, 71]. In the case of the signal at 269 nm, it can be observed that after 40 min of irradiation it decreased, and at 100 min, a displacement of the signal is observed at approximately 253 nm, which indicates that the aromatic group was not fractionated, generating by-products derived from the aromatic ring which can be attributed to N,N-dimethyl-p-phenylenediamine, as reported by Lide and Col. [72] and sulfanilic acid in [73]. It is worth mentioning that the C-TiO_2 sample does not show any signal after photodegradation, and it is likely that it has reached mineralization.

Table 4 shows a comparison of studies where TiO_2 was used for the degradation of methyl orange compared to TiO_2 synthesized with the *Cinnamomum verum* extract.

Fortunately, the C-TiO_2 sample being a pristine material shows a very good percentage of degradation in a short time compared to binary and ternary materials (Table 4). So, the green synthesis of nanostructures such as C-TiO_2 represents an area of opportunity for the synthesis of more efficient materials since it can be coupled with other semiconductors and graphitic materials and decorated or doped with metals.

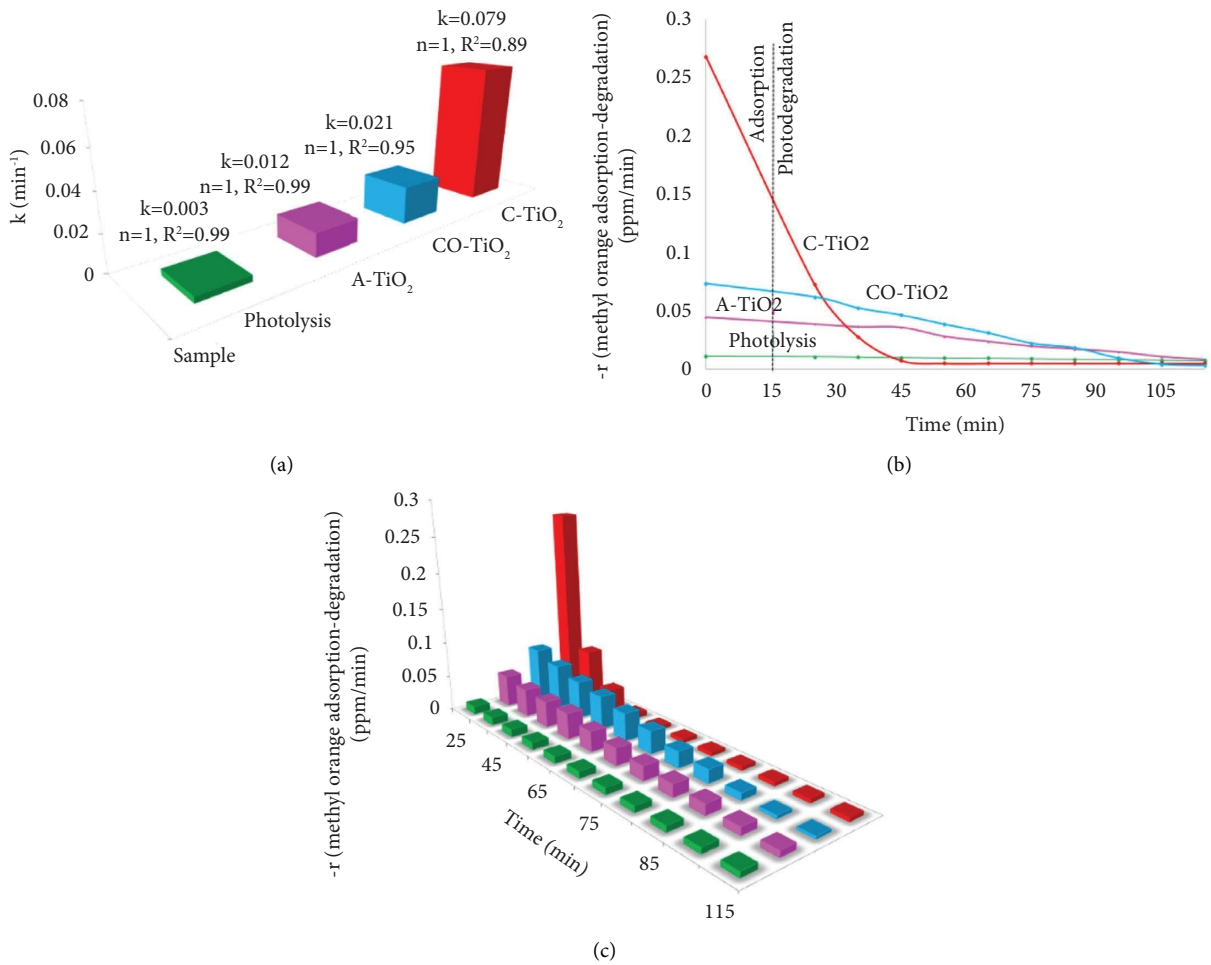

Figure 12: (a) Values obtained for the constant rate (k/min^{-1}) and order of the reaction ($n = 1$). (b, c) Rate profiles ($-r_{\text{methyl orange adsorption-degradation}}$) for the samples CO-$TiO_2$, C-$TiO_2$, A-$TiO_2$, and the photolysis of the system.

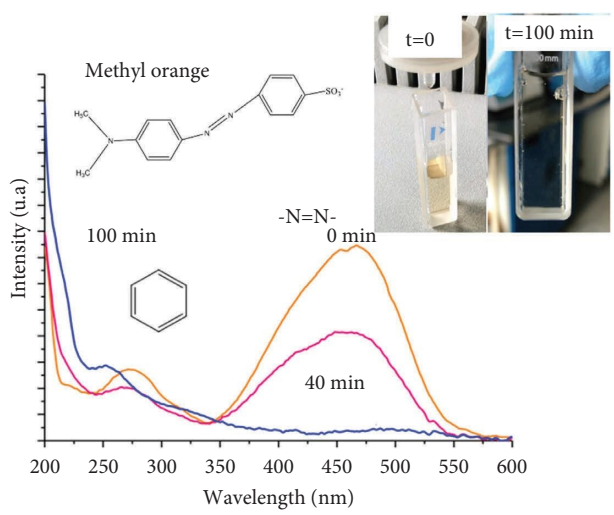

Figure 13: UV-vis spectra were obtained for the remnants of the sorption photodegradation of methyl orange, using CO-TiO_2 after 40 and 100 minutes of photodegradation.

Table 4: Comparison of different studies with the presence of TiO_2 synthesized with the *Cinnamomum verum* extract.

Photocatalyst	Synthesis method	Conditions	Removal efficiency (%)	Reference
$CuFeS_2$@ TiO_2	Mechanochemical route	Methyl orange visible light	Ca. 74% @ $t = 120$ min	[74]
Palygorskite/UiO-66- TiO_2	Wet chemical process	Methyl orange UV irradiation	100% @ $t < 120$ min	[75]
$ZnFe_2O_4$@TiO_2	Solvothermal-US assisted	Methyl orange UV irradiation	83.8% @ $t = 60$ min	[76]
Submicrometer TiO_2	Sol-gel/annealing	Methyl orange UV irradiation	Ca. 70% @ $t = 160$ min	[77]
TiO_2@CS-PANI	Process of polymerization	Methyl orange visible light	89.5% @ $t = 50$ min	[78]
Ag/TiO_2/carbon	Hydrothermal	Methyl orange visible light	94% @ $t = 100$ min	[79]
SnO_2/TiO_2	Hydrothermal	Methyl orange xenon lamp	91% @ $t = 120$ min	[80]
PTF- TiO_2	Composite solution with water spray	Methyl orange UVA irradiation	100% @ $t = 120$ min	[81]
C-TiO_2CO-TiO_2	Microwave irradiation	Methyl orange UV irradiation	100% @ $t = 40$ min 40% @ $t = 40$ min	This work

4. Conclusions

The optimization of the aqueous extract of *Cinnamomum verum* predicts a significant quadratic model, with an 82% prediction to the experimental variations.

It was feasible to synthesize nanocrystalline solids of the TiO_2 anatase phase by microwave irradiation for 10 minutes at 150 watts of power, with and without the aqueous extract of *Cinnamomum verum*, where the size of the particle is influenced by the bioactive during the synthesis (the aqueous extract of *Cinnamomum verum*) and the synthesis method (microwave irradiation), resulting in smaller size and crystallinity when synthesized with the aqueous extract of cinnamon.

The signals obtained in the FTIR spectrogram for the aqueous extract of *Cinnamomum verum* suggest the presence of terpenes, phenolic compounds, and flavonoids. For the samples A-TiO_2, C-TiO_2, and CO-TiO_2, the vibration modes of the Ti-O and Ti-O-Ti bonds are confirmed with the signal at 625 cm^{-1}. For the C-TiO_2 and CO-TiO_2 samples, the signal at 1104 cm^{-1} confirms the formation of TiO_2 nanoparticles in the anatase phase since this signal does not appear in the A-TiO_2 sample.

The use of the aqueous extract of *Cinnamomum verum* FIGURAS FIONALES promotes during the synthesis of TiO_2 that the value of the band gap decreases, affects the crystallinity, and decreases the size of the crystal, compared to the sample synthesized without the extract (CO-TiO_2) since both were prepared under the same synthesis conditions.

Raman spectroscopy confirms that the C-TiO_2 and CO-TiO_2 samples mostly contain the tetragonal crystallographic structure corresponding to the anatase phase. In both cases, the presence of traces of the face-centered cubic crystallographic structure of the rutile phase is also confirmed.

The commercial sample A-TiO_2 does not have a good particle size uniformity, where larger size particles predominate (50 nm). The sample synthesized by microwave irradiation without the extract promoted the formation of elliptical nanoparticles with good uniformity and sizes of approximately 20 nm in diameter. When using an aqueous extract of *Cinnamomum verum* during the synthesis, it generated a material with a uniform particle size (less than 15 nm in diameter), with a higher degree of crystallinity.

The use of the aqueous extract of cinnamon (*Cinnamomum verum*) during the synthesis of TiO_2 generated a semiconductor with a smaller crystal size, smaller particle size, higher crystallinity, smaller band gap, and greater adsorption capacity for the dye tested as a reaction model (methyl orange) than the one synthesized without cinnamon, which apparently promotes the total mineralization of methyl orange in 40 minutes of reaction, making it the best material of those evaluated in the adsorption-photodegradation.

Data Availability

The experimental data used to support the findings of this study are available from the corresponding author upon request.

Conflicts of Interest

The authors declare that they have no conflicts of interest.

Acknowledgments

The authors wish to thank the "Instituto Politécnico Nacional" for funding this research through the SIP 2022 1522, SIP 2022 0908, and SIP2022 1671 projects.

References

[1] S. K. Srikar, D. D. Giri, D. B. Pal, P. K. Mishra, and S. N. Upadhyay, "Green synthesis of silver nanoparticles: a review," *Green and Sustainable Chemistry*, vol. 06, no. 1, pp. 34–56, 2016.

[2] N. Jayarambabu, A. Akshaykranth, T. Venkatappa Rao, K. Venkateswara Rao, and R. Rakesh Kumar, "Green synthesis of Cu nanoparticles using Curcuma longa extract and their application in antimicrobial activity," *Materials Letters*, vol. 259, no. 15, Article ID 126813, 2020.

[3] J. M. Abisharani, S. Devikala, R. D. Kumar, M. Arthanareeswari, and P. Kamaraj, "Green synthesis of TiO2 nanoparticles using Cucurbita pepo seeds extract," *Materials Today: Proceedings*, vol. 14, no. 2, pp. 302–307, 2019.

[4] E. Tilahun Bekele, B. A. Gonfa, and F. K. Sabir, "Use of different natural products to control growth of titanium oxide nanoparticles in green solvent emulsion characterization, and their photocatalytic application," *Bioinorganic Chemistry and Applications*, vol. 2021, Article ID 6626313, 17 pages, 2021.

[5] S. Syamsol Bahri, Z. Harun, S. Khadijah Hubadillah et al., "Review on recent advance biosynthesis of TiO2 nanoparticles from plant-mediated materials: characterization, mechanism and application," *IOP Conference Series: Materials Science and Engineering*, vol. 1142, no. 1, p. 12005, 2021.

[6] P. Sathishkumar, F. L. Gu, Q. Zhan, T. Palvannan, and A. R. Mohd Yusoff, "Flavonoids mediated 'Green' nanomaterials: a novel nanomedicine system to treat various diseases current trends and future perspective," *Materials Letters*, vol. 210, no. 1, pp. 26–30, 2018.

[7] W. W. Andualem, F. K. Sabir, E. T. Mohammed, H. H. Belay, and B. A. Gonfa, "Synthesis of copper oxide nanoparticles using plant leaf extract of Catha edulis and its antibacterial activity," *Journal of Nanotechnology*, vol. 2020, Article ID 2932434, 10 pages, 2020.

[8] K. E. Rivas Mena, D. L. Muñoz, C. N. Pino Benítez, and N. Balcázar Morales, "Actividad antioxidante, contenido fenólico total y citotoxicidad de extractos polares obtenidos de plantas antidiabéticas colombianas Antioxidant activity, total phenolic content and cytotoxicity of polar extracts from Colombian antidiabetic plants," *Revista Cubana de Plantas Medicinales*, vol. 20, no. 3, pp. 277–289, 2015.

[9] A. Rana, K. Yadav, and S. Jagadevan, "A comprehensive review on green synthesis of nature-inspired metal nanoparticles: mechanism, application and toxicity," *Journal of Cleaner Production*, vol. 272, no. 1, Article ID 122880, 2020.

[10] H. Veisi, R. Ghorbani-Vaghei, S. Hemmati, M. H. Aliani, and T. Ozturk, "Green and effective route for the synthesis of monodispersed palladium nanoparticles using herbal tea extract (Stachys lavandulifolia) as reductant, stabilizer and capping agent, and their application as homogeneous and reusable catalyst in Suzuki coupling reactions water," *Applied Organometallic Chemistry*, vol. 29, no. 1, pp. 26–32, 2015.

[11] Y. Orooji, S. Mortazavi-Derazkola, S. M. Ghoreishi, M. Amiri, and M. Salavati-Niasari, "Mesopourous Fe3O4@SiO2 hydroxyapatite nanocomposite: green sonochemical synthesis using strawberry fruit extract as a capping agent, characterization and their application in sulfasalazine delivery and cytotoxicity," *Journal of Hazardous Materials*, vol. 400, no. 5, Article ID 123140, 2020.

[12] N. Singh, A. S. Rao, A. Nandal et al., "Phytochemical and pharmacological review of Cinnamomum verum J Presl-a versatile spice used in food and nutrition," *Food Chemistry*, vol. 338, no. 15, Article ID 127773, 2021.

[13] R. Pathak and H. Sharma, "A review on medicinal uses of Cinnamomum verum (cinnamon)," *Journal of Drug Delivery and Therapeutics*, vol. 11, no. 6, pp. 161–166, 2021.

[14] R. Souto da Rosa, R. Numata, and M. E. Marovic, "Análisis micrográfico y fitoquímico de muestras comerciales de "canela" - micrographic and phytochemical analysis of commercial samples of "Cinnamomum verum"," *Dominguezia*, vol. 31, no. 2, pp. 11–15, 2015.

[15] S. P. Goutam, G. Saxena, V. Singh, A. K. Yadav, R. N. Bharagava, and K. B. Thapa, "Green synthesis of TiO2 nanoparticles using leaf extract of Jatropha curcas L for photocatalytic degradation of tannery wastewater," *Chemical Engineering Journal*, vol. 336, no. 15, pp. 386–396, 2018.

[16] Y. C. Liu, Y. F. Lu, Y. Z. Zeng, C. H. Liao, J. C. Chung, and T. Y. Wei, "Nanostructured mesoporous titanium dioxide thin film prepared by sol-gel method for dye-sensitized solar cell," *International Journal of Photoenergy*, vol. 2011, Article ID 619069, 9 pages, 2011.

[17] I. Iavicoli, V. Leso, and A. Bergamaschi, "Toxicological effects of titanium dioxide nanoparticles a review of in vivo studies," *Journal of Nanomaterials*, vol. 2012, Article ID 964381, 36 pages, 2012.

[18] E. Mosquera, N. Rosas, A. Debut, and V. H. Guerrero, "Síntesis y caracterización de Nanopartículas de dióxido de titanio obtenidas por el método de Sol-Gel," *Revista Politécnica*, vol. 36, no. 3, pp. 1–7, 2015.

[19] C. P. Betancur Henao, V. Hernández Montes, and R. Buitrago Sierra, "Nanopartículas para materiales antibacterianos y aplicaciones del dióxido de titanio," *Revista Cubana de Investigaciones Biomédicas*, vol. 35, no. 4, pp. 387–402, 2016.

[20] B. Saha, S. Kumar, and S. Sengupta, "Green synthesis of nano silver on TiO2 catalyst for application in oxidation of thiophene," *Chemical Engineering Science*, vol. 199, no. 18, pp. 332–341, 2019.

[21] M. Atarod, M. Nasrollahzadeh, and S. Mohammad Sajadi, "Euphorbia heterophylla leaf extract mediated green synthesis of Ag/TiO2 nanocomposite and investigation of its excellent catalytic activity for reduction of variety of dyes in water," *Journal of Colloid and Interface Science*, vol. 462, no. 15, pp. 272–279, 2016.

[22] P. Barone, F. Stranges, M. Barberio, D. Renzelli, A. Bonanno, and F. Xu, "Study of band gap of silver nanoparticles - titanium dioxide nanocomposites," *Journal of Chemistry*, vol. 2014, Article ID 589707, 6 pages, 2014.

[23] J. Fei and J. Li, "Controlled preparation of porous TiO2-Ag nanostructures through supramolecular assembly for plasmon-enhanced photocatalysis," *Advanced Materials*, vol. 27, no. 2, pp. 314–319, 2015.

[24] I. N. Isnaeni, D. Indriyati, D. Sumiarsa, D. Sumiarsa, and I. Primadona, "Green synthesis of different TiO2 nanoparticle phases using mango-peel extract," *Materials Letters*, vol. 294, no. 1, Article ID 129792, 2021.

[25] G. V. Khade, M. B. Suwarnkar, N. L. Gavade, and K. M. Garadkar, "Green synthesis of TiO2 and its photocatalytic activity," *Journal of Materials Science: Materials in Electronics*, vol. 26, no. 5, pp. 3309–3315, 2015.

[26] I. S. Rodríguez-Clavel, S. P. Paredes-Carrera, S. O. Flores-Valle, E. J. Paz-García, J. C. Sánchez-Ochoa, and R. M. Pérez-Gutiérrez, "Effect of microwave or ultrasound irradiation in the extraction from feather keratin," *Journal of Chemistry*, vol. 2019, Article ID 1326063, 9 pages, 2019.

[27] E. J. Paz-García, S. P. Paredes-Carrera, S. O. Flores-Valle, I. S. Rodríguez-Clavel, J. C. Sánchez-Ochoa, and R. M. Pérez-Gutiérrez, "Synthesis of CuO for microwave-assisted pyrolysis of biomass," *Applied Sciences*, vol. 9, no. 24, pp. 5525–5613, 2019.

[28] M. Nüchter, B. Ondruschka, W. Bonrath, and A. Gum, "Microwave assisted synthesis – a critical technology overview," *Green Chemistry*, vol. 6, no. 3, pp. 128–141, 2004.

[29] K. Karthik, S. Dhanuskodi, S. Prabu Kumar, C. Gobinath, and S. Sivaramakrishnan, "Microwave assisted green synthesis of MgO nanorods and their antibacterial and anti-breast cancer activities," *Materials Letters*, vol. 206, no. 1, pp. 217–220, 2017.

[30] M. Tsuji, "Microwave-assisted synthesis of metallic nanomaterials in liquid phase," *ChemistrySelect*, vol. 2, no. 2, pp. 805–819, 2017.

[31] I. Bilecka and M. Niederberger, "Microwave chemistry for inorganic nanomaterials synthesis," *Nanoscale*, vol. 2, no. 8, pp. 1358–1374, 2010.

[32] T. A. Saleh and V. K. Gupta, "Photo-catalyzed degradation of hazardous dye methyl orange by use of a composite catalyst consisting of multi-walled carbon nanotubes and titanium dioxide," *Journal of Colloid and Interface Science*, vol. 371, no. 1, pp. 101–106, 2012.

[33] S. Al-Qaradawi and S. R. Salman, "Photocatalytic degradation of methyl orange as a model compound," *Journal of Photochemistry and Photobiology A Chemistry*, vol. 148, no. 1-3, pp. 161–168, 2002.

[34] E. A. Almaamary, S. R. S. Abdullah, H. A. Hasan, N. I. Ismail, R. A. A. Rahim, and M. Idris, "Plant-assisted remediation of wastewater contaminated with methyl orange using Scirpus grossus," *Journal of Environmental Biology*, vol. 40, no. 3, pp. 515–523, 2019.

[35] K. K. Karukstis, D. A. Savin, C. T. Loftus, and N. D. Angelo, "Spectroscopic studies of the interaction of methyl orange with cationic alkyltrimethylammonium bromide surfactants," *Journal of Colloid and Interface Science*, vol. 203, no. 1, pp. 157–163, 1998.

[36] P. Dinh Du, H. Thanh Danh, P. Ngoc Hoai, N. M. Thanh, V. Thang Nguyen, and D. Quang Khieu, "Heterogeneous UV/Fenton-Like degradation of methyl orange using iron terephthalate MIL-53 catalyst," *Journal of Chemistry*, vol. 2020, Article ID 1474357, 13 pages, 2020.

[37] S. Slassi, A. Fix-Tailler, G. Larcher, A. Amine, and A. El-Ghayoury, "Imidazole and azo-based schiff bases ligands as highly active antifungal and antioxidant components," *Heteroatom Chemistry*, vol. 2019, Article ID 6862170, 8 pages, 2019.

[38] J. R. Wagner, E. M. Mount, and H. F. Giles, "Design of experiments," in *Extrusion*Elsevier, Amsterdam, Netherlands, 2014.

[39] P. Sahoo and T. K. Barman, "ANN modelling of fractal dimension in machining," *Mechatronics and Manufacturing Engineering*, pp. 159–226, 2012.

[40] I. Savic, D. Gajic, S. Stojiljkovic, I. Savic, and S. di Gennaro, *Modelling and optimization of methylene blue adsorption from*

aqueous solution using bentonite clay, Vol. 33, Elsevier, Amsterdam, Netherlands, 2014.

[41] H. S. Kusuma and M. Mahfud, "Box Behnken design for investigation of microwave-assisted extraction of patchouli oil," *AIP Conference Proceedings*, vol. 1699, Article ID 050014, 2015.

[42] H. S. Kusuma, R. G. M. Sudrajat, D. F. Susanto, S. Gala, and M. Mahfud, "Response surface methodology (RSM) modeling of microwave-assisted extraction of natural dye from Swietenia mahagony: a comparation between Box-Behnken and central composite design method," *AIP Conference Proceedings*, vol. 1699, p. 50009, 2015.

[43] H. S. Kusuma, M. E. Syahputra, D. Parasandi, A. Altway, and M. Mahfud, "Optimization of microwave hydrodistillation of dried patchouli leaves by response surface methodology," *Rasayan Journal of Chemistry*, vol. 10, no. 3, pp. 861–865, 2017.

[44] A. Ansori, S. A. Wibowo, H. S. Kusuma, D. S. Bhuana, and M. Mahfud, "Production of biodiesel from nyamplung (Calophyllum inophyllum L.) using microwave with CaO catalyst from eggshell waste: optimization of transesterification process parameters," *Open Chemistry*, vol. 17, no. 1, pp. 1185–1197, 2019.

[45] H. S. Kusuma, A. N. Amenaghawon, H. Darmokoesoemo et al., "Evaluation of extract of Ipomoea batatas leaves as a green coagulant–flocculant for turbid water treatment: parametric modelling and optimization using response surface methodology and artificial neural networks," *Environmental Technology and Innovation*, vol. 24, Article ID 102005, 2021.

[46] H. S. Kusuma, A. N. Amenaghawon, H. Darmokoesoemo et al., "A comparative evaluation of statistical empirical and neural intelligence modeling of Manihot esculenta-derived leaves extract for optimized bio-coagulation-flocculation of turbid water," *Industrial Crops and Products*, vol. 186, Article ID 115194, 2022.

[47] O. D. Fagbemi, B. Sithole, and T. Tesfaye, "Optimization of keratin protein extraction from waste chicken feathers using hybrid pre-treatment techniques," *Sustainable Chemistry and Pharmacy*, vol. 17, Article ID 100267, 2020.

[48] A. P. Sarmento, A. C. Borges, A. T. D. Matos, and L. L. Romualdo, "Sulfamethoxazole and trimethoprim degradation by Fenton and Fenton-like processes," *Water (Switzerland)*, vol. 12, no. 6, p. 1655, 2020.

[49] S. Choudhary, K. Sharma, M. S. Bhatti, V. Sharma, and V. Kumar, "DOE-based synthesis of gellan gum-acrylic acid-based biodegradable hydrogels: screening of significant process variables and in situ field studies," *RSC Advances*, vol. 12, no. 8, pp. 4780–4794, 2022.

[50] E. O. Marson, V. A. B. de Paiva, B. R. Gonçalves et al., "Degradation of Direct Red 81 mediated by Fenton reactions: multivariate optimization, effect of chloride and sulfate, and acute ecotoxicity assessment," *Environmental Science and Pollution Research*, vol. 24, no. 7, pp. 6176–6186, 2017.

[51] M. Bagal, G. Kumbhar, S. Shukla, A. Tiwari, D. Gajbhiye, and A. Mohod, "Degradation of dye in a continuous zig-zag flow pattern photocatalytic reactor using a Doehlert matrix," *Chemical Engineering Research and Design*, vol. 188, pp. 315–329, 2022.

[52] J. Flores-Cantera, J. A. Cruz-Mérida, F. D. Velázquez-Herrera, S. P. Paredes-Carrera, and Y. Zarazua-Aguilar, "Synchronous microwave and ultrasound irradiation for the synthesis of SBA-15," *MRS Communications*, vol. 12, no. 3, pp. 388–393, 2022.

[53] M. N. Lakhan, R. Chen, A. H. Shar et al., "Eco-friendly green synthesis of clove buds extract functionalized silver nanoparticles and evaluation of antibacterial and antidiatom activity," *Journal of Microbiological Methods*, vol. 173, Article ID 105934, 2020.

[54] D. Raghunandan, P. A. Borgaonkar, B. Bendegumble et al., "Microwave-assisted rapid extracellular biosynthesis of silver nanoparticles using carom seed (Trachyspermum copticum) extract and in vitro studies," *American Journal of Analytical Chemistry*, vol. 02, no. 04, pp. 475–483, 2011.

[55] P. C. Nethravathi, Udayabhanu, G. Nagaraju, and D. Suresh, "TiO2 and Ag-TiO2 nanomaterials for enhanced photocatalytic and antioxidant activity: green synthesis using Cucumis melo juice," *Materials Today: Proceedings*, vol. 49, pp. 841–848, 2022.

[56] M. Michalska, J. Pavlovský, K. Lemański et al., "The effect of surface modification with Ag nanoparticles on 21 nm TiO2: anatase/rutile material for application in photocatalysis," *Materials Today Chemistry*, vol. 26, Article ID 101123, 2022.

[57] R. J. Kamble, P. V. Gaikwad, K. M. Garadkar, S. R. Sabale, V. R. Puri, and S. S. Mahajan, "Photocatalytic degradation of malachite green using hydrothermally synthesized cobalt-doped TiO2 nanoparticles," *Journal of the Iranian Chemical Society*, vol. 19, no. 1, pp. 303–312, 2022.

[58] N. Qutub, P. Singh, S. Sabir, S. Sagadevan, and W. C. Oh, "Enhanced photocatalytic degradation of Acid Blue dye using CdS/TiO2 nanocomposite," *Scientific Reports*, vol. 12, no. 1, pp. 5759–5818, 2022.

[59] A. K. Manna, S. R. Joshi, B. Satpati et al., "Influence of ion implantation on depth dependent phase transition in TiO2 films, anatase nanostructures and photo-absorption behavior," *Current Applied Physics*, vol. 43, pp. 1–8, 2022.

[60] T. Zhu and S.-P. Gao, "The stability, electronic structure, and optical property of TiO2 polymorphs," *Journal of Physical Chemistry C*, vol. 118, no. 21, pp. 11385–11396, 2014.

[61] X. Zhang, J. Zhao, A. V. Whitney, J. W. Elam, and R. P. van Duyne, "Ultrastable substrates for surface-enhanced Raman spectroscopy: Al 2O3 overlayers fabricated by atomic layer deposition yield improved anthrax biomarker detection," *Journal of the American Chemical Society*, vol. 128, no. 31, pp. 10304–10309, 2006.

[62] A. di Paola, M. Bellardita, and L. Palmisano, "Brookite, the least known TiO2 photocatalyst," *Catalysts*, vol. 3, no. 1, pp. 36–73, 2013.

[63] J. F. Li, X. D. Tian, S. B. Li et al., "Surface analysis using shell-isolated nanoparticle-enhanced Raman spectroscopy," *Nature Protocols*, vol. 8, no. 1, pp. 52–65, 2013.

[64] K. Vajda, K. Saszet, E. Z. Kedves et al., "Shape-controlled agglomeration of TiO2 nanoparticles. New insights on polycrystallinity vs. single crystals in photocatalysis," *Ceramics International*, vol. 42, no. 2, pp. 3077–3087, 2016.

[65] V. C. M. Rojas, L. Matejova, A. López Milla, and G. J. Cruz, "Obtención de partículas de TiO2 por sol-gel, asistido con ultrasonido para aplicaciones fotocatalíticas," *Revista de la Sociedad Quimica del Peru*, vol. 81, no. 3, pp. 201–211, 2015.

[66] E. I. Moreno Valencia, S. P. Paredes Carrera, J. C. Sánchez Ochoa, S. O. Flores Valle, and J. R. Avendaño Gómez, "Diclofenac degradation by heterogeneous photocatalysis with Fe_3O_4/Ti_xO_y /activated carbon fiber composite synthesized by ultrasound irradiation," *Materials Research Express*, vol. 4, no. 11, Article ID 115026, 2017.

[67] L. B. de Lima, W. A. Viturino da Silva, S. L. Silva et al., "Chemical and antibacterial analysis of Cinnamomum verum leaves extract and fractions against multidrug resistant

bacteria," *Natural Product Research*, vol. 36, no. 10, pp. 2559–2564, 2022.

[68] R. M. Pérez Gutiérrez, F. F. Martínez Jerónimo, J. G. Contreras Soto, A. Muñiz Ramírez, and M. F. Estrella Mendoza, "Optimization of ultrasonic-assisted extraction of polyphenols from the polyherbal formulation of Cinnamomum verum, Origanum majorana, and Origanum vulgare and their anti-diabetic capacity in zebrafish (Danio rerio)," *Heliyon*, vol. 8, no. 1, p. 08682, 2022.

[69] A. D. Assefa, Y. S. Keum, and R. K. Saini, "A comprehensive study of polyphenols contents and antioxidant potential of 39 widely used spices and food condiments," *Journal of Food Measurement and Characterization*, vol. 12, no. 3, pp. 1548–1555, 2018.

[70] S. Xie, P. Huang, J. J. Kruzic, X. Zeng, and H. Qian, "A highly efficient degradation mechanism of methyl orange using Fe-based metallic glass powders," *Scientific Reports*, vol. 6, no. 1, p. 21947, 2016.

[71] C. C. Wang, J. R. Li, X. L. Lv, Y. Q. Zhang, and G. Guo, "Photocatalytic organic pollutants degradation in metal-organic frameworks," *Energy & Environmental Science*, vol. 7, no. 9, pp. 2831–2867, 2014.

[72] C. J. Knill and J. F. Kennedy, "CRC handbook of data on organic compounds," *Carbohydrate Polymers*, vol. 26, no. 3, p. 243, Jan. 1995.

[73] F. M. Arrazola-Dominguez, J. T. Ávila Salazar, C. G. Gomez Sierra, and S. Hernández Garrido, *Química orgánica experimental a escala semimicro y fundamentos de la espectroscopía*, Vol. 2, Instituto Politécnico Nacional, Mexico, 2016.

[74] E. Dutkova, M. Baláž, N. Daneu et al., "Properties of CuFeS2/TiO2 nanocomposite prepared by mechanochemical synthesis," *Materials*, vol. 15, no. 19, p. 6913, 2022.

[75] T. Ioannidou, M. Anagnostopoulou, D. Papoulis, K. C. Christoforidis, and I. A. Vasiliadou, "UiO-66/Palygorskite/TiO2 ternary composites as adsorbents and photocatalysts for methyl orange removal," *Applied Sciences*, vol. 12, no. 16, p. 8223, 2022.

[76] R. Chen, S. Ding, B. Wang, and X. Ren, "Preparation of ZnFe2O4@TiO2 novel core-shell photocatalyst by ultrasonic method and its photocatalytic degradation activity," *Coatings*, vol. 12, no. 10, p. 1407, 2022.

[77] W. Ko, B. J. Cha, Y. D. Kim, and H. O. Seo, "Sub-micro photocatalytic TiO2 particles for a water depollution: comparable removal efficiency to commercial P25 and easy separation via a simple sedimentation," *Catalysis Today*, vol. 403, no. 1, pp. 47–57, 2022.

[78] S. Palliyalil, R. K. V. Chola, S. Vigneshwaran, N. C. Poovathumkuzhi, B. M. Chelaveettil, and S. Meenakshi, "Ternary system of TiO2 confined chitosan–polyaniline heterostructure photocatalyst for the degradation of anionic and cationic dyes," *Environmental Technology and Innovation*, vol. 28, Article ID 102586, 2022.

[79] Y. Jin, W. Tang, J. Wang et al., "High photocatalytic activity of spent coffee grounds derived activated carbon-supported Ag/TiO2 catalyst for degradation of organic dyes and antibiotics," *Colloids and Surfaces A: Physicochemical and Engineering Aspects*, vol. 655, no. 5, Article ID 130316, 2022.

[80] H. Huang, S. Zhao, Y. Yang et al., "Axially wrinkled tubular SnO2/TiO2 heterostructures for effective degradation of organic pollutants," *Materials Science in Semiconductor Processing*, vol. 152, Article ID 107065, 2022.

[81] S. Ramasundaram, A. Balasankar, S. Arokiyaraj, P. Sumathi, and T. Hwan Oh, "Multi-useable titanium dioxide and poly(vinylidene fluoride) composite foam photocatalyst for degradation of organic pollutants," *Applied Surface Science*, vol. 609, no. 30, Article ID 155264, 2023.

Hindawi
Journal of Chemistry
Volume 2023, Article ID 3971686, 10 pages
https://doi.org/10.1155/2023/3971686

Research Article

Biologically Reduced Zinc Oxide Nanosheets Using *Phyllanthus emblica* Plant Extract for Antibacterial and Dye Degradation Studies

Awais Khalid,[1] Pervaiz Ahmad,[2] Mayeen Uddin Khandaker,[3,4] Yosra Modafer,[5] Hanadi A. Almukhlifi,[6] Abdulrahman S. Bazaid,[7] Abdu Aldarhami,[8] Abdulaziz M. Alanazi,[9] Ohoud A. Jefri,[10] Md. Mohi Uddin,[11] and Husam Qanash[7,12]

[1]*Department of Physics, Hazara University Mansehra, Mansehra, Khyber Pakhtunkhwa 21300, Pakistan*
[2]*Department of Physics, University of Azad Jammu and Kashmir, Muzaffarabad 13100, Pakistan*
[3]*Center for Applied Physics and Radiation Technologies, School of Engineering and Technology, Sunway University, Bandar Sunway 47500, Selangor, Malaysia*
[4]*Department of General Educational Development, Faculty of Science and Information Technology, Daffodil International University, DIU Rd, Dhaka 1341, Bangladesh*
[5]*Department of Biology, College of Science, Jazan University, Jazan 45142, Saudi Arabia*
[6]*Department of Chemistry, Faculty of Science, University of Tabuk, Tabuk 71491, Saudi Arabia*
[7]*Department of Medical Laboratory Science, College of Applied Medical Sciences, University of Ha'il, Hail 55476, Saudi Arabia*
[8]*Department of Medical Microbiology, Qunfudah Faculty of Medicine, Umm Al-Qura University, Al-Qunfudah 21961, Saudi Arabia*
[9]*Department of Chemistry, Faculty of Science, Islamic University of Madinah, Madinah 42351, Saudi Arabia*
[10]*Department of Biological Science, Faculty of Science, King Abdulaziz University, Jeddah 21589, Saudi Arabia*
[11]*Department of Physics, Chittagong University of Engineering and Technology (CUET), Chattogram 4349, Bangladesh*
[12]*Medical and Diagnostics Research Centre, University of Ha'il, Hail 55476, Saudi Arabia*

Correspondence should be addressed to Pervaiz Ahmad; pervaiz_pas@yahoo.com and Mayeen Uddin Khandaker; mayeenk@diu.edu.bd

Received 14 December 2022; Revised 10 February 2023; Accepted 18 April 2023; Published 29 April 2023

Academic Editor: Ashanul Haque

The nanostructures synthesized using the green chemistry method have recently attracted the attention of scientists due to their significance in many scientific domains. This work provides an overview of the biosynthesis of zinc oxide (ZnO) nanosheets (NSs) using *Phyllanthus emblica* plant (PEP) extract. X-ray diffraction analysis (XRD), X-ray photoelectron spectroscopy (XPS), scanning electron microscopy (SEM), and Fourier transform infrared (FTIR) were used to analyze the synthesized ZnO-NSs. Evaluation of the antibacterial activity of biosynthesized ZnO-NSs was performed. ZnO-NSs exhibit effective antibacterial activity against Gram-positive (*S. pyogenes* and *S. aureus*) and Gram-negative (*S. typhi* and *E. coli*) bacterial strains. *S. typhi* is the most sensitive microbe towards ZnO-NSs and formed a 21 mm zone of inhibition (ZOI). ZnO-NSs are also tested as a photocatalyst in the degradation of methyl orange (MO) and rhodamine B (RB). The degradation rate of MO was 90%, and RB was 96% after being exposed to UV light for 120 min. The as-synthesized ZnO-NSs exhibited selective dye degradation and showed relatively better photocatalytic activity for positively charged (cationic) dyes. This work could lead to the fabrication of high-yield photocatalysts, which have the potential to degrade textile dyes from aqueous solution.

1. Introduction

Nanotechnology is considered a developing field in science and technology. It has been playing a crucial role in the development of various nanomaterials in recent years. Numerous advantages of pharmaceutical nanoparticles have grabbed the attention of many researchers for innovations [1]. The prevalence of infections that are resistant to antibiotic treatment has prompted a constant quest for new substitutes [2]. Water-borne bacteria species constitute a serious hazard to public health among drug-resistant pathogens because they cause the spread of illnesses such as diarrhea [3]. A variety of pathogenic bacterial species have shown inorganic nanoparticles to be poisonous [4, 5]. The bactericidal impact of inorganic nanoparticles is poorly understood, even though their broad-spectrum biocidal action is well documented [6, 7]. It has been suggested that when ions are released into a solution, reactive oxygen species are generated that are harmful to bacteria [8]. Other studies indicated that due to their small size, nanoparticles could enter the cell wall of bacteria and damage organelles, which results in cell death [9, 10]. In contrast to their organic counterparts, inorganic antibiotics have multiple targets [11, 12].

Zinc oxide is considered a quite interesting material because of its application in areas such as optical, endodontics, and gas sensing. In addition, zinc oxide has been considered an antifungal agent which has no toxicity and harmful environmental effects [13–15]. Due to the safety of zinc oxide nanoparticles and their compatibility with human skin, it is accepted as an additive for textiles and surfaces that meet human skin [16]. ZnO nanoparticles express high photocatalytic properties, which enhances their antifungal activity [17, 18]. ZnO nanoparticles produce ROS under UV light. The primary uses of zinc oxide in the chemical, cosmetics, and pharmaceutical sectors are for its photocatalytic and antibacterial properties [19]. Zinc oxide nanoparticles' antibacterial capabilities have been widely investigated [20, 21], and the development of oxidative stress linked to the particles' photocatalytic activity is thought to be the main cause of toxicity [22]. ZnO is a potential water purification product due to its antiseptic characteristics [23–27].

The plant *Phyllanthus emblica,* commonly identified as Indian gooseberry, grows in areas of Indonesia, India, China, and the Malay Peninsula that are tropical and subtropical. Emblica is one of the most significant herbs in the conventional Ayurvedic medical system and has excellent antioxidant properties. Other conventional medical systems employ it for its immunomodulatory, hepatoprotective, antiulcer, anti-inflammatory, and anticancer effects. Flavonoids, gallic acid [24], kaempferol, pyrogallol, ellagic acid, elaeocarpusin, nor sesquiterpenoids, geraniin, corilagin, and prodelphinidins B1 and B2 are some of this plant's chemical components. Plants that have been reported to produce ZnO NPs through biosynthesis are *Citrus aurantifolia* [28], *Calotropis gigantea* [29], *Ocimum tenuiflorum* [30], *Tamarindus indica* [31], Maple leaf [32], *Phyllanthus niruri* [23], *Solanum nigrum* [21], and *Anisochilus carnosus* [22]. Green synthesis of nanomaterials has recently been performed using microbes and plant extract that have been reported to produce ZnO-NSs due to their accessibility, affordability, nontoxic nature, biodegradability, and environmentally friendly qualities.

In this study, ZnO with nanosheets (NSs) like morphology has been synthesized using a green approach. Zinc nitrate and *Phyllanthus emblica* leaves extract were used to prepare ZnO-NSs. XRD, XPS, SEM, FTIR, and UV spectrophotometer were used to analyze the prepared NSs. Studies have also been carried out to analyze the antibacterial and photocatalytic efficiency of ZnO-NSs. Several methods were reported to synthesize ZnO, but no one in the literature claims to synthesize ZnO-NSs using *Phyllanthus emblica* plant leaves extract.

2. Material and Methods

2.1. Preparation of Zinc Oxide Using Phyllanthus emblica Leaves Extract. Freshly collected PE leaves were washed using distilled water to eliminate any dust, and after that, they were dried at room temperature. A mortar and pestle were used to convert the dried leaves into fine powder. 10 grams of fine powdered PE were added to 100 ml of deionized water under stirring. The subsequent mixture was poured into 0.05 M $ZnCl_2$ solution under continuous stirring on a magnetic hot plate at 90°C for 2 hours. The yellow-colored precipitate was obtained and cooled down to room temperature. To remove the impurity contents, this extract was then centrifuged for 15 minutes at 1000 rpm. The precipitate was continually washed in methanol and distilled water before being dried at 80°C. Finally, at 650°C, the product was calcined for roughly 3 hours in a muffle furnace. The complete synthesis procedure of ZnO using PE extract is shown in Figure 1.

2.2. Characterization. The authors used SEM (MAIA3 TESCAN) to study the physical appearance of ZnO, XRD (Bruker D8 (Germany) was employed to study crystallographic structure, FTIR (Nicolet Avatar 370) was used to analyze the attached functional groups, and chemical composition of synthesized material is studied using XPS Kratos Axis Ultra DLD apparatus (Manchester, UK).

2.3. Antimicrobial Assay. The efficiency of the prepared nanomaterials to inhibit human pathogens was evaluated against microorganisms using the disc diffusion method [26]. Gram-negative pathogenic strains of *E. coli* (ATCC® 33876), *S. typhimurium* (ATCC® 14028), and Gram-positive pathogenic strains of *S. aureus* (ATCC® 11632) and *S. pyogenes* (ATCC® 19615) were employed. To ensure that the nanoparticles were distributed uniformly, 20 mg of the prepared samples were used to make dilution in 1 ml of deionized water. After adding nutrient agar and allowing it to settle, the sterilized Petri plates were inoculated with Gram-negative and Gram-positive bacteria. The solid agar was covered with discs of Whatman filter paper, size 6 mm. At 37°C, nutritional broth was added to all the strains for 18 to 24 hours. The sterile cotton swabs were used to make

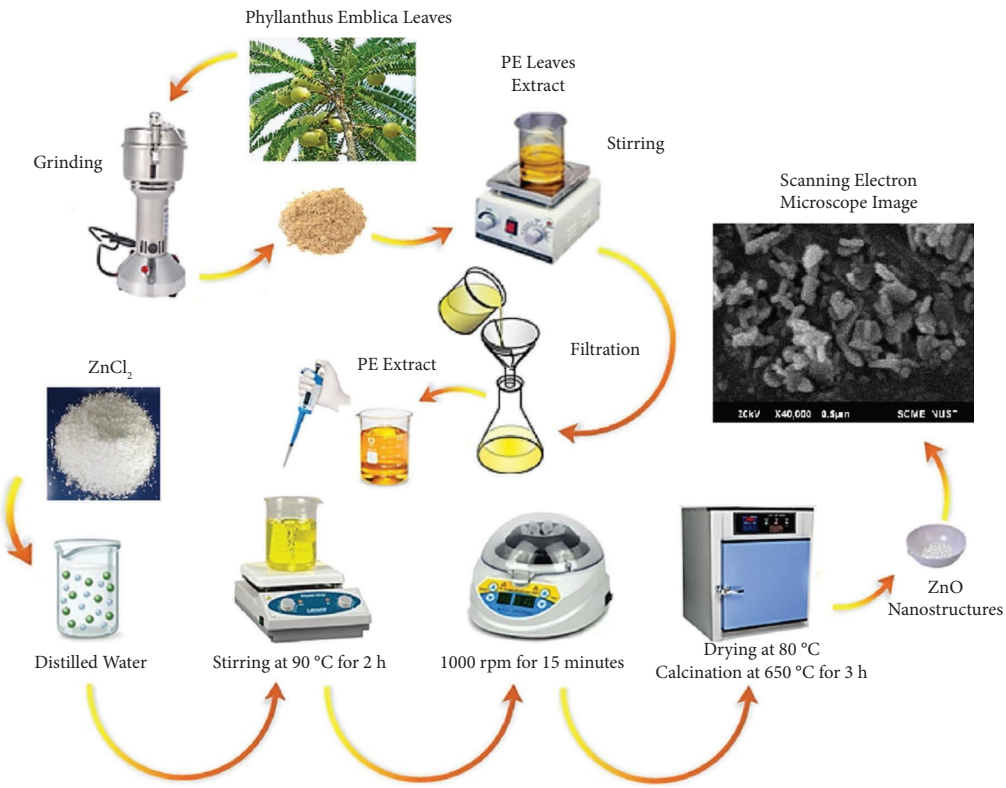

Figure 1: The schematic diagram for the complete synthesis procedure of ZnO-NSs.

streaks across the Muller Hinton agar (MHA) surface. The extract (20 μL) was pipetted onto a sterile paper disc 6 mm in diameter. As a standard reference antibiotic/control, discs containing 40 μl/mL of ciprofloxacin, were employed. Moreover, the plates were placed in an incubator and subjected to incubation at 37°C for 24 h after the solvent had evaporated. The development of a clean zone around the discs is proof that the test sample has antibacterial properties. Using an antibiotic zone scale, the diameter of the inhibition zones was assessed. There were three repetitions for each experiment.

2.4. Photocatalytic Activity Measurement. ZnO nanoparticles' photocatalytic activity was calculated based on the rate at which methylene orange (MO) and rhodamine B (RB) was oxidized when exposed to UV light. Before illumination, both MO and RB dyes (10 ppm) were mixed for 30 min in the dark with the required amount of catalyst (0.5 g). UV-visible spectrophotometer was used at various time intervals to observe the reaction's progress. The color of reaction mixtures progressively faded until it eventually became colorless. An indication of the successful catalytic activity of ZnO was the absorbance for MO and RB measured with a UV-vis spectrometer.

3. Result and Discussion

3.1. Scanning Electron Microscopy (SEM). The morphological features of the synthesized material were investigated through SEM. The obtained images of the ZnO sample showed square-shaped nanosheets with significant particle aggregation, as shown in Figure 2. ZnO-NSs are comparatively homogeneous due to the regular dispersal of Zn cations within a three-dimensional structure. The cluster (agglomeration) in the sample is a result of increased density carried on by the small gap between the particles, while it may also be related to the rapid grain development and nucleation at higher temperatures.

3.2. Structural Analysis. Phase and structural analysis of ZnO NPs prepared using *Phyllanthus emblica* is carried out by XRD analysis and shown in Figure 1. All marked diffraction peak positions in Figure 3 are well matched with the standard JCPDS Card: 36-1451. The corresponding X-ray diffraction peaks at observed planes (100), (002), (101), (102), (110), (103), (200), (112), (201), and (004) confirm the formation of hexagonal wurtzite structure of ZnO. The diffraction peaks' observed line broadening is proof that the produced ZnO NPs are in the nanoscale range. Major peaks' increasing full width at half maxima (FWHM) supports the decline in crystallite size. Using the Scherrer formula, the average crystallite size of ZnO-NSs is determined from the X-ray line broadening.

$$D = \frac{k\lambda}{\beta \cos \theta}. \quad (1)$$

D and λ represent the crystallite size and radiation's wavelength (1.5406 for Cu $k\alpha$), β is the peak intensity width at half maximum, θ is the peak position, and k is a constant

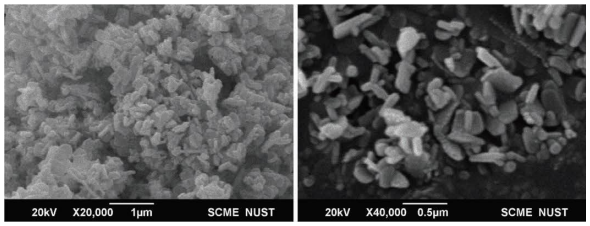

Figure 2: SEM micrographs for ZnO nanosheets synthesized using *Phyllanthus emblica* extract.

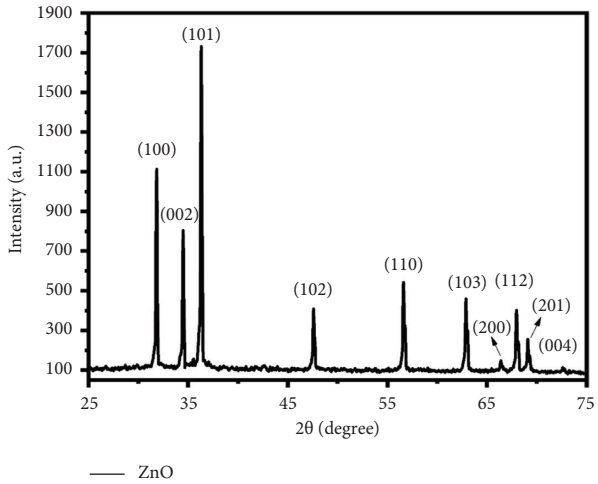

Figure 3: Structural analysis of ZnO-NSs using X-ray photoelectron spectroscopy.

(0.94). The synthesized ZnO-NSs have an average crystallite size of 31 nm.

The Williamson–Hall method was used to determine the lattice strain and crystallite size of ZnO, as shown in Figure 4.

$$\beta \cos \theta = k\lambda D + 4\varepsilon \operatorname{Sin} \theta, \quad (2)$$

where β, D, and ε in the above equation represent full width at half maximum (FWHM), crystallite size, and strain, respectively. The strain is obtained from the linear fit of the data while plotting $\beta \cos \theta$ against $4 \sin \theta$. In comparison to the Williamson–Hall method, which measures crystallite sizes using microstrain, the Scherrer method measures crystallite sizes using the X-rays cohesion length. Any vacancies and defects will make the observed size to be smaller than the actual size.

3.3. Elemental and Chemical State Analysis. To identify the constituent elements of the compound synthesized and examine the sample's surface, a surface-sensitive XPS analysis was conducted. Surface scanning was performed to get the survey spectrum, which provides information about the elemental content of the sample surface, as shown in Figure 5(a). Zn and O are recognized with their corresponding distinctive peaks in a low-resolution spectrum (survey analysis). All samples underwent charge shift correction using the adventitious carbon peak binding energy (284.6 eV). High-resolution spectra of the relevant elements

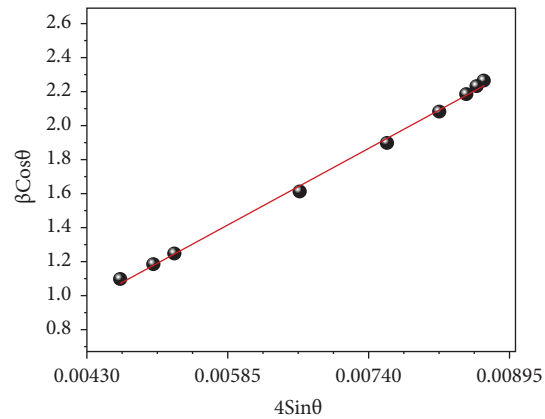

Figure 4: Williamson–Hall plot for ZnO-NS.

were examined in the chemical state study. After laser fragmentation, we carried out high-resolution scanning of the sample. Due to spin-orbital coupling, high-resolution spectra of transition metals such as zinc will exhibit a doublet. Zn thus had doublets for the sample examined in this study. These doublets, which are known as $2p_{3/2}$ and $2p_{1/2}$, represent 2p orbitals. Figures 5(b) and 5(c) show the high-resolution spectra of the materials following laser fragmentation, namely the ZnO sample for Zn 2p and O 1s. The binding energies that are displayed are those that match the primary peak, $Zn2p_{3/2}$. The energy difference between the Zn 2p doublets was 23.1 eV for all samples, which is consistent with previous research [33]. The Zn^{2+} oxidation state is indicated by Zn 2p binding energies in the range of 1022 eV [34]. Pure metallic oxides were chemically represented in the ZnO XPS spectra.

3.4. Fourier Transform Infrared. FTIR spectra of ZnO-NSs produced using the green method were captured in the 500–4000 cm^{-1} range, as shown in Figure 6. The vibrations of the H-O-H bending and O-H stretching were believed to be responsible for the peaks in 1734 and 3418 cm^{-1}, respectively. This demonstrates that the nanocrystalline ZnO contains a little amount of H_2O. The sample was calcined at 400°C for 3 hours, although not all the adsorbed OH groups were removed. The peak in the range of 1451–1734 cm^{-1} was linked to the stretching mode of the C=O group, whereas the band at 847 cm^{-1} corresponds to the vibrations of deformation and elongation of the vibratory Zn-O in ZnO [35].

3.5. Antibacterial Activity. According to numerous studies [36, 37], varying particle morphologies have a considerable impact on ZnO's antibacterial efficacy. This morphology-dependent behavior can be addressed considering the percentage of active aspects on the NPs. Nanomaterial studies have been encouraged, to produce specific nanosized ZnO for antibacterial measurements [38]. The antibacterial activity is also significantly influenced by the concentration and particle size. Research findings have shown that the harmful effect of NPs on microorganisms increases with

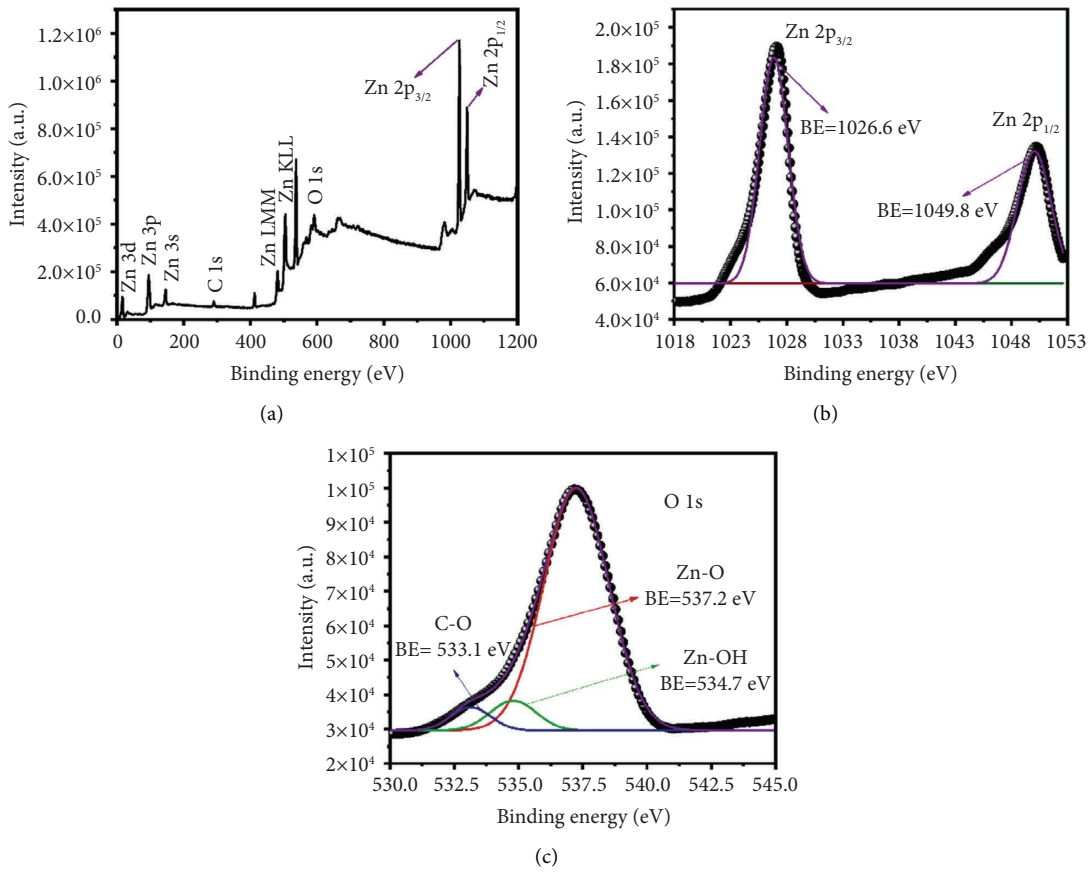

Figure 5: X-ray photoelectron spectroscopic micrographs for (a) survey scan and (b, c) high-resolution spectra for Zn 2p and O 1s.

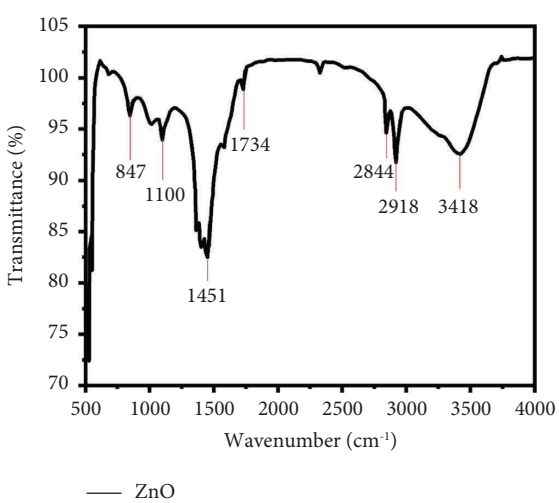

Figure 6: FTIR spectra of ZnO-NSs using *Phyllanthus emblica* extract.

decreasing NP size [39, 40]. Smaller NPs are more effective in penetrating bacterial membranes due to their smaller size and larger contact area [41–43]. The ZnO-NSs employed in this study were prepared using a green chemistry approach and shaped like nanosheets with an average length of 97.2 nm.

The microbial sensitivity of ZnO-NSs fluctuates with the microorganisms and the concentrations of the ZnO-NSs. A zone of inhibition is formed for measured values of 30 μg/mL, 50 μg/mL, and 100 μg/mL. The disc diffusion method was used to test the antibacterial activity of ZnO-NSs against diverse microbes, as shown in Figure 7. Antibacterial activity of pure ZnO shows 18 mm, and 21 mm of inhibition zone for *E. coli* (ATCC® 33876) and *S. Typhimurium* (ATCC® 14028) while for *S. aureus* (ATCC® 11632), *S. pyogenes* (ATCC® 19615) ZnO shows 17 mm and 18 mm of inhibition zone as demonstrated in Table 1 and Figure 8. The inhibition zone indicates the sensitivity of the bacteria to toxic substances, resulting in large inhibition diameters for disinfectant-sensitive pathogens and smaller or even no inhibition diameters for resistant pathogens. Our findings demonstrate that ZnO-NSs can only effectively inhibit bacteria at concentrations of 100 μg/mL or above. This validates that greater volume and concentration result in improved antibacterial action.

3.6. Dye Degradation Study. The factors that affect the photocatalytic dye degradation efficiency of ZnO-based materials are large surface area, particle size, and the presence of functional groups on the surface [44, 45]. ZnO's surface area and photodegradation abilities are improved when its size is reduced. Figures 9(a) and 9(b) show the degradation of MO and RB over time under UV light

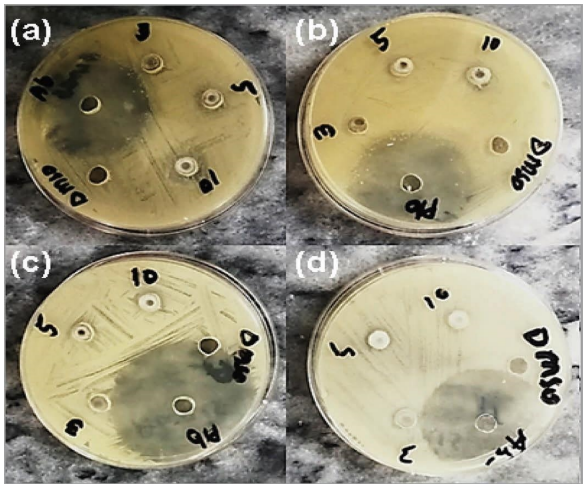

Figure 7: Petri plates containing ZnO-NSs employed against microorganisms using disc diffusion method (a) *S. typhi*, (b) *E. coli*, (c) *S. pyogenes*, and (d) *S. aureus*.

Table 1: Information zone of inhibition formed against bacterial isolates.

Bacteria		30 μg/mL	50 μg/mL	100 μg/mL
E. coli	Inhibition zone (mm)	14 ± 0.28	15 ± 0.36	18 ± 0.34
S. typhimurium		15 ± 0.3	16 ± 0.34	21 ± 0.38
S. aureus		13 ± 0.26	14 ± 0.48	17 ± 0.3
S. pyogenes		9 ± 0.18	12 ± 0.4	18 ± 0.32

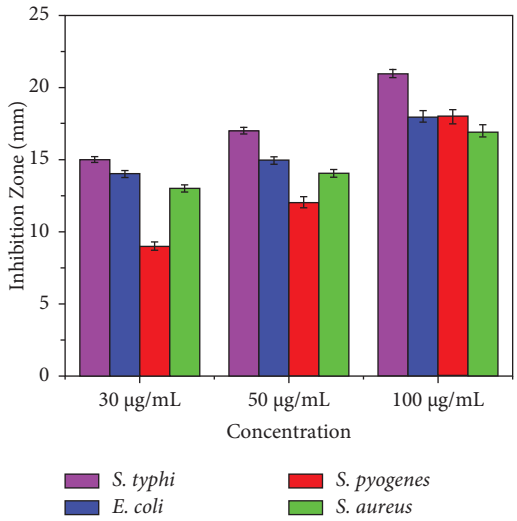

Figure 8: Inhibition zone of microorganisms formed using ZnO-NSs synthesized by PE extract.

irradiation in the presence of ZnO-NSs. The relative intensity of UV-visible spectra was used to determine the amount of dye degradation. The MO and RB dyes were kept in the dark for 20 min before exposure to UV light. No change was observed in the absorption behavior of the dyes in the dark before exposure to UV light. The findings showed that the maximum absorbance of MO and RB dye solution occurs at 481 nm and 563 nm, and constantly decreases when the UV irradiation time is increased. This indicates that ZnO may have accelerated dye degradation with increasing UV exposure time. The degradation % of RB and MO is shown in Figures 10(a) and 10(b); it is observed that the degradation % progressively increased, and about 96% of RB dye and 90% of MO dye degraded within two hours. The kinetics of the photodegradation of organic dyes using ZnO-NSs photocatalyst can be described by several models,

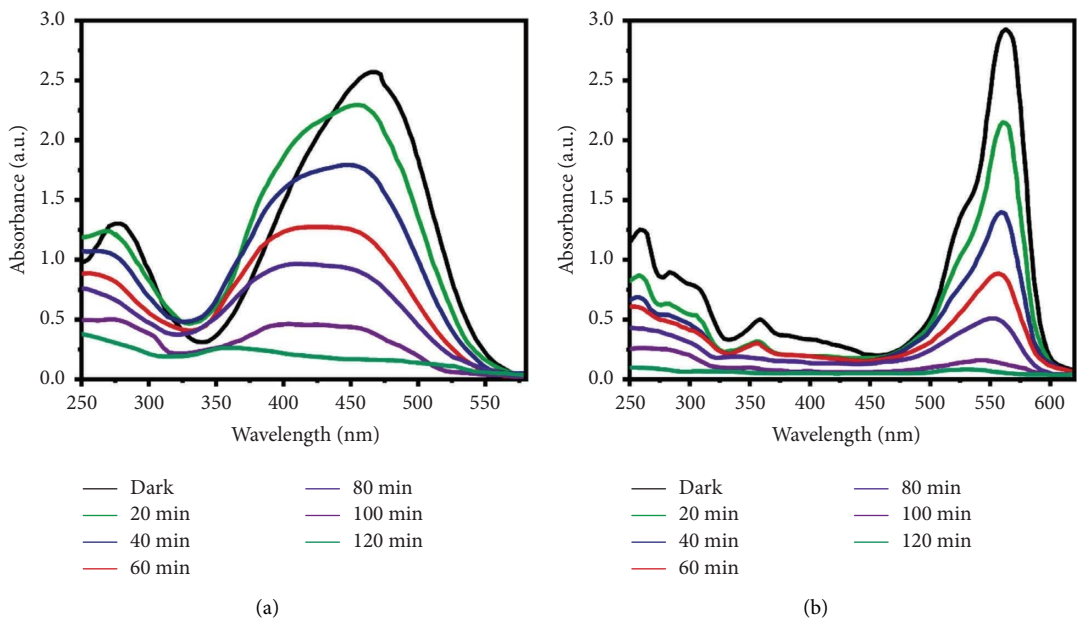

Figure 9: The photocatalytic dye degradation efficiency of ZnO-NSs against (a) methyl orange (MO) and (b) rhodamine B (RB) dyes.

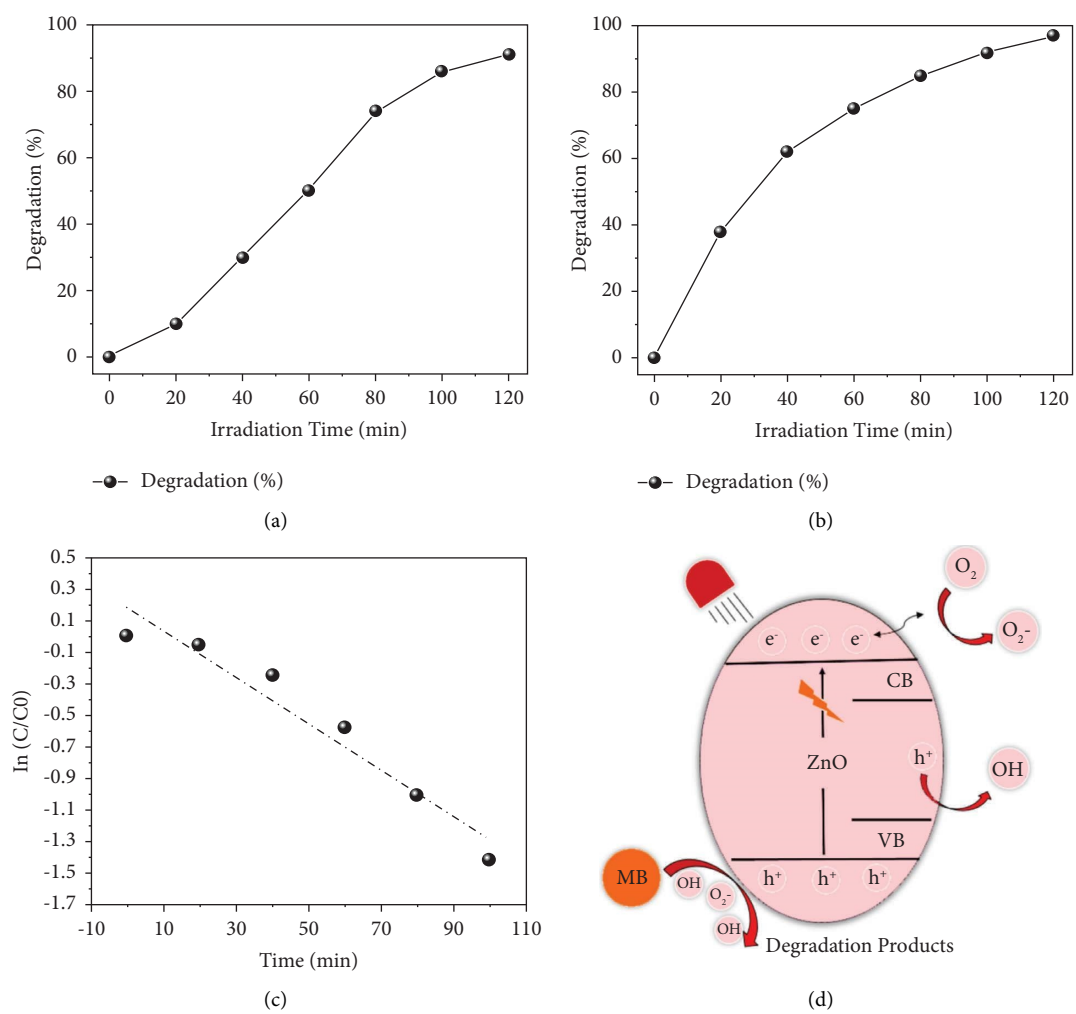

Figure 10: Degradation time versus time of exposure graph for (a) MO, (b) RB dyes using ZnO-NSs, (c) pseudo-first-order kinetics, and (d) schematic illustration for charge transportation process of ZnO-NSs.

including the pseudo-first-order kinetics model and the pseudo-second-order kinetics model [46]. These models are based on the observation that the rate of degradation of RB is dependent on the concentration of both RB and ZnO-NSs. By understanding the kinetics of the photo degradation process, it is possible to optimize the conditions for the efficient removal of MB using ZnO photocatalyst. The rate of degradation calculated using the pseudo-first-order kinetics and schematic illustration for the charge transportation process of ZnO-NSs is shown in Figures 10(c) and 10(d).

4. Conclusion

Green leaf extract from the *Phyllanthus emblica* plant was used to successfully prepare ZnO-NSs, which demonstrates its efficiency as an environmentally friendly, nontoxic, and cost-effective technique to synthesize nanomaterials. The PE extracts employed in the production of nanoparticles act as capping and reducing agents. By using the disc diffusion method, the antibacterial activity of produced nanomaterial was analyzed. It was discovered that ZnO-NSs had a larger zone of inhibition for *S. typhi* (21 mm) than all other tested microbes. The growth and survival curves found in this study help us better understand how ZnO NPs work to kill microorganisms over time. Finally, the findings of this study indicate that some of the most severe and prominent food-borne pathogens can be successfully inhibited when ZnO-NSs prepared from PE extract are used as an antibacterial agent in food systems. The comparative dye degradation studies revealed that the catalysts were able to degrade both rhodamine B (cationic) and methyl orange (anionic) dyes. Rhodamine B (RB) and methyl orange (MO) were degraded by ZnO photocatalyst with the highest efficiency of 96% and 90%, respectively, in 120 minutes. Results suggest that many other hazardous organic compounds that are present in both commercial and residential water resources can also be photodegraded using a ZnO photocatalyst.

Data Availability

All data used in the findings of this study are included within the manuscript.

Conflicts of Interest

The authors declare that they have no conflicts of interest.

Acknowledgments

The authors extend their appreciation to the Higher Education Commission of Pakistan (HEC) for providing funds for our research work under the National Research Program for Universities (NRPU) Project no. 10928. Sunway University International Research Networks Grant Scheme 2.0, STR-IRNGS-SET-CAPRT-01-2022 is acknowledged.

References

[1] H. Agarwal, S. Soumya, and S. Rajeshkumar, "Mechanistic study on antibacterial action of zinc oxide nanoparticles synthesized using green route," *Chemico-Biological Interactions*, vol. 286, pp. 60–70, 2018.

[2] P. Pandey, M. S. Packiyaraj, H. Nigam, G. S. Agarwal, B. Singh, and M. K. Patra, "Antimicrobial properties of CuO nanorods and multi-armed nanoparticles against B. anthracis vegetative cells and endospores," *Beilstein Journal of Nanotechnology*, vol. 5, no. 1, pp. 789–800, 2014.

[3] I. A. Ahmed, H. S. Hussein, Z. A. Alothman, A. G. Alanazi, N. S. Alsaiari, and A. Khalid, "Green synthesis of Fe–Cu bimetallic supported on alginate-limestone nanocomposite for the removal of drugs from contaminated water," *Polymers*, vol. 15, no. 5, p. 1221, 2023.

[4] S. Kar, B. Bagchi, B. Kundu et al., "Synthesis and characterization of Cu/Ag nanoparticle loaded mullite nanocomposite system: a potential candidate for antimicrobial and therapeutic applications," *Biochimica et Biophysica Acta (BBA) - General Subjects*, vol. 1840, no. 11, pp. 3264–3276, 2014.

[5] T. Zhang, X. Wu, S. M. Shaheen et al., "Improving the humification and phosphorus flow during swine manure composting: a trial for enhancing the beneficial applications of hazardous biowastes," *Journal of Hazardous Materials*, vol. 425, Article ID 127906, 2022.

[6] G. Franci, A. Falanga, S. Galdiero et al., "Silver nanoparticles as potential antibacterial agents," *Molecules*, vol. 20, no. 5, pp. 8856–8874, 2015.

[7] A. A. Abdellatif, H. N. Alturki, and H. M. J. Tawfeek, "Different cellulosic polymers for synthesizing silver nanoparticles with antioxidant and antibacterial activities," *Scientific Reports*, vol. 11, no. 1, pp. 84–18, 2021.

[8] A. A. Abdellatif, "Green synthesis of silver nanoparticles incorporated aromatherapies utilized for their antioxidant and antimicrobial activities against some clinical bacterial isolates," *Bioinorganic Chemistry and Applications*, vol. 2022, Article ID 2432758, 14 pages, 2022.

[9] O. Bondarenko, K. Juganson, A. Ivask, K. Kasemets, M. Mortimer, and A. Kahru, "Toxicity of Ag, CuO and ZnO nanoparticles to selected environmentally relevant test organisms and mammalian cells in vitro: a critical review," *Archives of Toxicology*, vol. 87, no. 7, pp. 1181–1200, 2013.

[10] A. Khalid, P. Ahmad, A. I. Alharthi et al., "Structural, optical, and antibacterial efficacy of pure and zinc-doped copper oxide against Pathogenic bacteria," *Nanomaterials*, vol. 11, no. 2, p. 451, 2021.

[11] A. A. Abdellatif, "Silver nanoparticles stabilized by poly (vinyl pyrrolidone) with potential anticancer activity towards prostate cancer," *Synthesis, Characterization, and Applications of Bioinorganic-Based Nanomaterials for Environmental Pollution Hazards*, vol. 2022, Article ID 6181448, 12 pages, 2022.

[12] A. A. Abdellatif, "Green synthesis of silver nanoparticles for enhancing wound healing activity in rats," *Saudi Pharmaceutical Journal*, vol. 10, 2022.

[13] M. Srinisha, "Amla fruit mediated synthesis of zinc oxide nanoparticles and its antifungal activity," *International Journal of Research in Pharmaceutical Sciences*, vol. 10, 2019.

[14] A. Naveed Ul Haq, "Synthesis approaches of zinc oxide nanoparticles: the dilemma of ecotoxicity," *Journal of Nanomaterials*, vol. 2017, Article ID 8510342, 14 pages, 2017.

[15] R. J. I. J. Saraf, "Cost effective and monodispersed zinc oxide nanoparticles synthesis and their characterization," *International Journal of Advances in Applied Sciences*, vol. 2, no. 2, pp. 85–88, 2013.

[16] Q. Liu, M. Zhang, Z. Fang, and X. Rong, "Effects of ZnO nanoparticles and microwave heating on the sterilization and product quality of vacuum packaged Caixin," *Journal of the Science of Food and Agriculture*, vol. 94, no. 12, pp. 2547–2554, 2014.

[17] J. W. Rasmussen, E. Martinez, P. Louka, and D. G. Wingett, "Zinc oxide nanoparticles for selective destruction of tumor cells and potential for drug delivery applications," *Expert Opinion on Drug Delivery*, vol. 7, no. 9, pp. 1063–1077, 2010.

[18] A. Khalid, P. Ahmad, R. Memon et al., "Structural, optical, and renewable energy-assisted photocatalytic dye degradation studies of ZnO, CuZnO, and CoZnO nanostructures for wastewater treatment," *Separations*, vol. 10, no. 3, p. 184, 2023.

[19] R. A. Basit, Z. Abbasi, M. Hafeez et al., "Successive photocatalytic degradation of methylene blue by ZnO, CuO and ZnO/CuO synthesized from coriandrum sativum plant extract via green synthesis technique," *Crystals*, vol. 13, no. 2, p. 281, 2023.

[20] P. K. Stoimenov, R. L. Klinger, G. L. Marchin, and K. J. Klabunde, "Metal oxide nanoparticles as bactericidal agents," *Langmuir*, vol. 18, no. 17, pp. 6679–6686, 2002.

[21] T. Jin, D. Sun, J. Su, H. Zhang, and H. J. Sue, "Antimicrobial efficacy of zinc oxide quantum dots against Listeria monocytogenes, Salmonella enteritidis, and *Escherichia coli* O157: H7," *Journal of Food Science*, vol. 74, no. 1, pp. M46–M52, 2009.

[22] A. Baranwal, "Prospects of nanostructure materials and their composites as antimicrobial agents," *Frontiers In Microbiology*, vol. 9, p. 422, 2018.

[23] A. Khalid, P. Ahmad, A. I. Alharthi et al., "Enhanced optical and antibacterial activity of hydrothermally synthesized cobalt-doped zinc oxide cylindrical microcrystals," *Materials*, vol. 14, no. 12, p. 3223, 2021.

[24] A. Khalid, P. Ahmad, A. Khan et al., "Effect of Cu doping on ZnO nanoparticles as a photocatalyst for the removal of organic wastewater," *Bioinorganic Chemistry and Applications*, vol. 2022, Article ID 9459886, 12 pages, 2022.

[25] A. Sharma, D. Mangla, A. Choudhry, M. Sajid, and S. Ali Chaudhry, "Facile synthesis, physico-chemical studies of Ocimum sanctum magnetic nanocomposite and its adsorptive application against Methylene blue," *Journal of Molecular Liquids*, vol. 362, Article ID 119752, 2022.

[26] A. Sharma, D. Mangla, M. Chaudhry, and S. A. Chaudhry, "Recent advances in magnetic composites as adsorbents for wastewater remediation," *Journal of Environmental Management*, vol. 306, Article ID 114483, 2022.

[27] A. Choudhry, "Origanum vulgare manganese ferrite nanocomposite: An advanced multifunctional hybrid material for dye remediation," *Environmental Research*, vol. 220, Article ID 115193, 2023.

[28] N. A. Samat and R. M. J. C. I. Nor, *Sol–gel synthesis of zinc oxide nanoparticles using Citrus aurantifolia extracts*, vol. 39, pp. S545–S548, 2013.

[29] S. P. J. B. Patil and A. Sciences, "Calotropis gigantea assisted green synthesis of nanomaterials and their applications: a review," vol. 9, no. 1, pp. 1–9, 2020.

[30] S. Sharma, K. Kumar, N. Thakur, and M. S. Chauhan, "Ocimum tenuiflorum leaf extract as a green mediator for the synthesis of ZnO nanocapsules inactivating bacterial pathogens," *Chemical Papers*, vol. 74, no. 10, pp. 3431–3444, 2020.

[31] D. Thatikayala, V. Banothu, J. Kim, D. S. Shin, S. Vijayalakshmi, and J. Park, "Enhanced photocatalytic and antibacterial activity of ZnO/Ag nanostructure synthesized by *Tamarindus indica* pulp extract," *Journal of Materials Science: Materials in Electronics*, vol. 31, no. 7, pp. 5324–5335, 2020.

[32] S. Vivekanandhan, M. Schreiber, C. Mason, A. K. Mohanty, and M. Misra, "Maple leaf (Acer sp.) extract mediated green process for the functionalization of ZnO powders with silver nanoparticles," *Colloids and Surfaces B: Biointerfaces*, vol. 113, pp. 169–175, 2014.

[33] A. Khalid, "Synthesis of boron-doped zinc oxide nanosheets by using phyllanthus emblica leaf extract: a sustainable environmental applications," *Frontiers in Chemistry*, vol. 10, 2022.

[34] A. Khalid, P. Ahmad, A. I. Alharthi et al., "Synergistic effects of Cu-doped ZnO nanoantibiotic against Gram-positive bacterial strains," vol. 16, no. 5, p. e0251082, 2021.

[35] X. Bai, L. Li, H. Liu, L. Tan, T. Liu, and X. Meng, "Solvothermal synthesis of ZnO nanoparticles and anti-infection application in vivo," *ACS Applied Materials & Interfaces*, vol. 7, no. 2, pp. 1308–1317, 2015.

[36] A. Stanković, S. Dimitrijević, and D. Uskoković, "Influence of size scale and morphology on antibacterial properties of ZnO powders hydrothemally synthesized using different surface stabilizing agents," *Colloids and Surfaces B: Biointerfaces*, vol. 102, pp. 21–28, 2013.

[37] N. Talebian, S. M. Amininezhad, and M. Doudi, "Controllable synthesis of ZnO nanoparticles and their morphology-dependent antibacterial and optical properties," *Journal of Photochemistry and Photobiology B: Biology*, vol. 120, pp. 66–73, 2013.

[38] A. Sirelkhatim, S. Mahmud, A. Seeni et al., "Review on zinc oxide nanoparticles: antibacterial activity and toxicity mechanism," *Nano-Micro Letters*, vol. 7, no. 3, pp. 219–242, 2015.

[39] S. Nair, A. Sasidharan, V. V. Divya Rani et al., "Role of size scale of ZnO nanoparticles and microparticles on toxicity toward bacteria and osteoblast cancer cells," *Journal of Materials Science: Materials in Medicine*, vol. 20, no. S1, pp. 235–241, 2009.

[40] O. J. Yamamoto, "Influence of particle size on the antibacterial activity of zinc oxide," *International Journal of Inorganic Materials*, vol. 3, no. 7, pp. 643–646, 2001.

[41] M. Ramani, S. Ponnusamy, C. Muthamizhchelvan, and E. Marsili, "Amino acid-mediated synthesis of zinc oxide nanostructures and evaluation of their facet-dependent antimicrobial activity," *Colloids and Surfaces B: Biointerfaces*, vol. 117, pp. 233–239, 2014.

[42] Z. Razzaq, A. Khalid, P. Ahmad et al., "Photocatalytic and antibacterial potency of titanium dioxide nanoparticles: a cost-effective and environmentally friendly media for treatment of air and wastewater," *Catalysts*, vol. 11, no. 6, p. 709, 2021.

[43] P. Ahmad, A. Khalid, M. U. Khandaker et al., "The antibacterial and antioxidant efficacy and neutron sensing potency of 10B enriched hexagonal boron nitride nanoparticles,"

Materials Science in Semiconductor Processing, vol. 141, Article ID 106419, 2022.

[44] M. Hafeez, S. Afyaz, A. Khalid et al., "Synthesis of cobalt and sulphur doped titanium dioxide photocatalysts for environmental applications," *Journal of King Saud University Science*, vol. 34, no. 4, Article ID 102028, 2022.

[45] A. Khalid, P. Ahmad, A. Khan et al., "Cytotoxic and photocatalytic studies of hexagonal boron nitride nanotubes: a potential candidate for wastewater and air treatment," *RSC Advances*, vol. 12, no. 11, pp. 6592–6600, 2022.

[46] S. Shakeel, F. N. N. Talpur, M. A. Iqbal et al., "Xanthan gum-mediated silver nanoparticles for ultrasensitive electrochemical detection of Hg2+ ions from water," *Catalysts*, vol. 13, no. 1, p. 208, 2023.

Hindawi
Journal of Chemistry
Volume 2023, Article ID 2554098, 12 pages
https://doi.org/10.1155/2023/2554098

Research Article

Study of Microstructure and Wear Resistance of AA5052/B_4C Nanocomposites as a Function of Volume Fraction Reinforcement to Particle Size Ratio by ANN

D. Dinesh Kumar,[1] A. Balamurugan,[2] K. C. Suresh,[3] R. Suresh Kumar,[4] N. Jayanthi,[5] T. Ramakrishnan,[6] S. K. Hasane Ahammad,[7] S. Mayakannan,[8] and S. Venkatesa Prabhu[9]

[1]*Department of Electronics and Instrumentation Engineering, St. Joseph's College of Engineering, OMR Road, Chennai, Tamilnadu, India*
[2]*Department of Physics, Government Arts and Science College, Avinashi, Tamil Nadu, India*
[3]*Department of Physics, Government First Grade Women's College, Tumkur, Karnataka, India*
[4]*Department of Mechanical Engineering, R. M. K. Engineering College, Chennai, Tamilnadu, India*
[5]*Department of Physics, R. M. K College of Engineering and Technology, Chennai, Tamilnadu, India*
[6]*Department of Mechanical Engineering, Sri Eshwar College of Engineering, Coimbatore, Tamilnadu, India*
[7]*Department of Electronics and Communication Engineering, Koneru Lakshmaiah Education Foundation, Guntur, Andhra Pradesh, India*
[8]*Department of Mechanical Engineering, Vidyaa Vikas College of Engineering and Technology, Tiruchengode, Namakkal, Tamilnadu, India*
[9]*Center of Excellence for Bioprocess and Biotechnology, Department of Chemical Engineering, College of Biological and Chemical Engineering, Addis Ababa Science and Technology University, Addis Ababa, Ethiopia*

Correspondence should be addressed to S. Venkatesa Prabhu; venkatesa.prabhu@aastu.edu.et

Received 14 October 2022; Revised 29 January 2023; Accepted 5 April 2023; Published 18 April 2023

Academic Editor: B. R. Ramesh Bapu

The effects of the percentage volume of reinforcement, the ratio of reinforcement, and the matrix size of particles on the wear behavior of AA5052/B_4C metal matrix composites (MMCs) examine. This research examines a model function developed from an artificial neural network (ANN). AA5052/B_4C composites bent using a powder metallurgy technique to hardness and ball-on-disc wear testing. There are two exemptions such as (1) when the percentage volume of reinforcement is less than 8% and (2) when the ratio of reinforcement particle size (Rs) and matrix particle size (Ms) increases before decreasing. The results show that wear loss decreases with increasing percentage volume of reinforcement and ratio of Rs and Ms. In the second case, wear loss is increased at high levels of percentage volume (14%) since the proportion of reinforcement and matrix size of the particle is close to 1. When the volume percentage of reinforcement is high (14%) and the matrix and reinforcement particle sizes are substantial (120 m), the reinforcement particles become dislodged and break. Because these broken-up particles are easily removed from the surface, the material's wear resistance is reduced. In this case, raising the volume fraction yields a uniformly higher hardness for all Rs/Ms values; hence, composites with lower reinforcement volume percentages show better wear resistance. Hardness and wear resistance have no relationship with one another.

1. Introduction

MMCs are an emerging material class with a wide range of desirable properties, including low weight, high strength, specific modulus, low density, low elongation, and high stiffness [1]. Excellent operating performance, wear resistance, thermal stabilization, minimal thermal extension, and maximum flexibility to experience the distortion process by conventional methods such as powder metallurgy and casting have contributed to the increase in emerging of AMMC strengthened with ceramics in both the industry and academia. As a result of its compatibility with a wide variety of metallic and ceramic substrate plating materials, AA5052/B_4Cp is useful in microelectronic packing for aviation, automation, and microapplications.

Because of its unique qualities, including the lack of undesired reaction products and less processing cost, solid-state powder metallurgy (PM) is frequently employed as a production method for Al-based MMCs [2, 3]. However, this approach also has drawbacks, such as a lack of homogeneity and a low density from the pores [4].

Sintering, pressing, mixing settings (external factors), and material aspects all influence the qualities of particulate-reinforced MMCs made through solid-state powder metallurgy. Material factors (internal factors) considered in this investigation include Ms and Rs and the percentage volume of reinforcement particles.

Wear resistance in Al-based MMCs has been found to increase with both Rs and volume percentage of reinforcement [5]. Although internal parameters have a significant bearing on tribological features and reinforcement particle clustering, the impact of the matrix size of the particle and the ratio of Rs/Ms has not been extensively studied.

Analysts frequently resort to analytical approaches to investigate the effects of MMCs' material features [6]. The use of an ANN is currently one of the most widely adopted and successful approaches. Characterizing the material and providing insight into the effective manufacturing material and processing parameters are two additional benefits of using ANN [7]. Thickness, porous, and stiffness predictions for AA5052/B_4C MMC were investigated by authors [8]. Their analysis took a Cu-weight percentage and a B_4C volume fraction as input parameters. A maximum inaccuracy of 5.99% was determined.

Researchers [9]employed an artificial neural network to examine the relationship between the axial stress and strain of AA5052/B_4Cp MMCs and the thickness, size of the particle, percentage volume of particles, and load. The authors [10] also used an artificial neural network to examine the results of particle size, percentage of volume, and milling duration on the density, hardness, and tensile strength of Al2024/B_4C MMCs. The authors examined the bending strength and stiffness of aluminium-silicon-magnesium-based MMC [11] using ANN to see if they varied with the Rs. The B_4C particle was the only input during ANN. Researchers found that B_4C's hardness and bending strength improved along with its particle size [11].

The wear resistance of MMCs was studied using ANN in specific research. To examine wear behavior, authors [12] used ANN on AA5052/B_4C MMCs. The wear behavior of AA5052/B_4C MMCs was studied to determine the impact of load and testing temperature. At the same time, in investigating the wear rate of aluminium/Al_2O_3 MMCs, authors [13] employed an ANN technique, with a wear rate as output and percentage volume of reinforcement, applying pressure, sliding speed, and testing temperature as input factors. Clustering, an undesirable phenomenon, is reported to increase the volume percentage of reinforcement. Authors [14] also investigated the impact of the reinforcing volume fraction. The researchers discovered that squeeze-cast AA5052/B_4C MMCs with a higher volume proportion of B_4C particles had better wear resistance [15–17]. They also found that an increase in percentage volume led to a higher critical transition temperature between the moderate and severe regimes of wear loss [17]. Additional instances of the successful application of ANN to the characterization of MMCs can be found in the scholarly literature [18].

This research looked at how the Rs/Ms ratio affected the wear behavior of AA5052/B_4Cp MMCs. The studies relied on a model function determined with the help of a neural network simulator and the data collected in the experiments. Micrographs of the microstructures were acquired before and after the wear testing, allowing for a comparison of the two data sets. To get a more in-depth look at AA5052/B_4Cp MMCs to wear, an ANN was used with wear loss and hardness as input factors and percentage volume of reinforcement, Ms and Rs as output parameters.

2. Materials and Experimental Procedure

Production of AA5052-B_4C composites was achieved through powder metallurgy. Five different volume fractions of B_4C particles were used to strengthen the aluminum particles (99.5% purity). Matrix and reinforcement particle sizes of 70, 95, 120, 145, and 170 μm were tested and found to be optimal. In a triaxial mixer, particles of aluminum and B_4C of varying sizes were mixed for a one-hour cold compact at a pressure 450 MPa. After compacting, the particle mixes were sintered at 600 C for 8 hours.

The hardness of the composite specimen was evaluated using a Brinell hardness tester (DM-AKB-3000, Navin Engineering) outfitted with a ball indenter measuring 2.5 mm in diameter and a 62.5 kgf force. The wear tests were conducted in the ball-on-disc-type machine with dry sliding circumstances. Steel ball bearings with a diameter of 6 mm and a hardness of 62HRC were employed as the counter-face material. Normal loads of 10 N were applied for the wear testing, and the sliding velocity was held constant at 0.421 ms^{-1}, with the sliding distance set at 550 m. The starting and ending weights of every sample were recorded to calculate wear.

Table 1 displays the wear loss and hardness test results for all the specimens tested, including those with a wide variety of matrix particle sizes, reinforcement particle sizes, and reinforcement volume fractions.

Table 1: Data for various process parameters.

Sample no. Unit	Reinforcement volume fraction (%)	Size of reinforcement particle (R_s) (μm)	Size of matrix particle (M_s) (μm)	Rs/Ms proportion	Wear loss (g)	Hardness (HB)	Clustering rate (%)
1	6	120	120	1.20	0.049891	35.2	No cluster
2	8	95	145	0.75	0.013212	38.3	3.72
3	8	95	95	1.20	0.030286	39.7	2.63
4	8	145	145	1.20	0.025552	37.2	1.98
5	8	145	95	1.80	0.044321	39.3	0.93
6	12	70	120	0.73	0.008251	41.3	9.15
7	12	120	170	0.84	0.003065	42.4	8.06
8	12	120	120	1.20	0.006964	40.8	6.45
9	12	170	120	1.45	0.020632	40.3	4.81
10	12	120	70	1.78	0.027553	39.2	3.93
11	18	95	145	0.75	0.002255	41.6	13.46
12	18	95	95	1.20	0.003668	44.2	8.21
13	18	145	145	1.20	0.002815	40.3	10.81
14	18	145	95	1.74	0.003793	43.1	6.36
15	20	120	120	1.20	0.001894	44.7	15.53

3. Artificial Neural Network

Digital models of the nervous systems and artificial neural networks are based on the biology of intelligence [19]. They are typically depicted as networks of neurons that can calculate values from inputs when data are fed into the system. The ability of artificial neural network models to infer a function from observation is often cited as proof of their usefulness. This is especially helpful when it would be impractical to design such a function by hand, as is the case when working with complex data or tasks. This means that ANNs can provide meaning for the interrelationships between the variables of a high-dimensional space. When asked to represent intricate linear and nonlinear connections, ANNs have excelled well. Compared to statistical approaches, ANNs provide a radically new way to describe materials and manage their processing.

Neural networks can be programmed to do a variety of tasks. The neural network is seen in Figure 1. The weight matrices (w), bias vectors (b), transfer function (f), reinforcement (R), and outputs (a) in this network are R, f, w, and a, respectively.

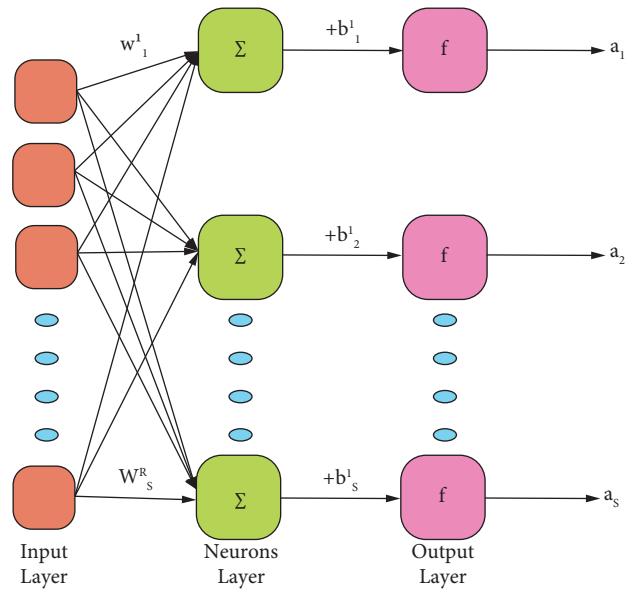

Figure 1: Single layer network with R/S neurons.

Training a neural network needs to receive examples of data that may be used as inputs. Each input is multiplied by a variant known as the weight and added to a variant known as the bias beforehand, incoming the neuron; the preliminary range of both variations can be specified in advance if the neural network has only one layer [18]. The experimental output value is compared with the neuron's output, which is the functional transfer input. The input is the total of the values received from each input. If the resulting error value exceeds the allowed error value, the result is sent back to the network to adjust the weights and biases until the intended effect is achieved. Figure 2 depicts the iterative process of network training and evaluation, with various techniques used to explore the resulting model's performance.

3.1. Implementation of the Neural Network. Numerous parameters can be adjusted during installation to optimize the performance, speed, and accuracy of an ANN [20]. Parameters include the network learning rate, the number of layers, the number of neurons in each layer, and many others. In this research, the neural network was trained using abrasive resistance and hardness as input factors and the Rs, Ms, and the reinforcement volume fraction. The network was educated using the most popular and effective approach for training, backpropagation error. According to authors [21], the Pearson correlation coefficient is the other artificial neural network metric that demonstrates how successfully a network is trained. The research shows that Pearson correlation coefficient values greater than 0.9 are considered satisfactory for this parameter [22].

Dispersion in the training data can significantly affect the number of layers and neurons; similarly, variation in the input and output factors might cause difficulties in the network learning process. Data are normalized to reduce the variation in such circumstances. Similar to the method used by authors [23], all parameter values were normalized in this study by dividing them by the most significant value of the relevant parameter to place them in a uniform range from 0 to 1. The optimal PCC (postclassification comparison) value was found by trial and error. Table 2 provides the artificial neural network's specific architecture and the relevant factors' values. There were three distinct layers to the network. The ANN structure gave nominal values for the sum of neurons in the input, hidden, and output layers. Authors [24] indicate that growing the number of neurons, being the minor process units, does not result in enhanced network performance and accuracy. This is something to remember while choosing the number of layers and neurons. The rate at which a network learns is another crucial variable that must be considered during deployment. Authors [25] discussed that a low value for this parameter results in slow network convergence, which slows down the time it takes to obtain the desired response. In that case, there is a risk that the training process may become unstable, increasing the amount of inaccuracy in the response from cycle to cycle.

3.2. Model Function. The values of w, f, p, and b parameters can be acquired upon successful training of the neural network. Figure 3 indicates the overall structure of the neural network used in this research. Using these values, one may determine the function that connects the manufacturing process parameters as inputs to the measured outcomes (wear loss and hardness) as outputs. The model function can be derived as follows:

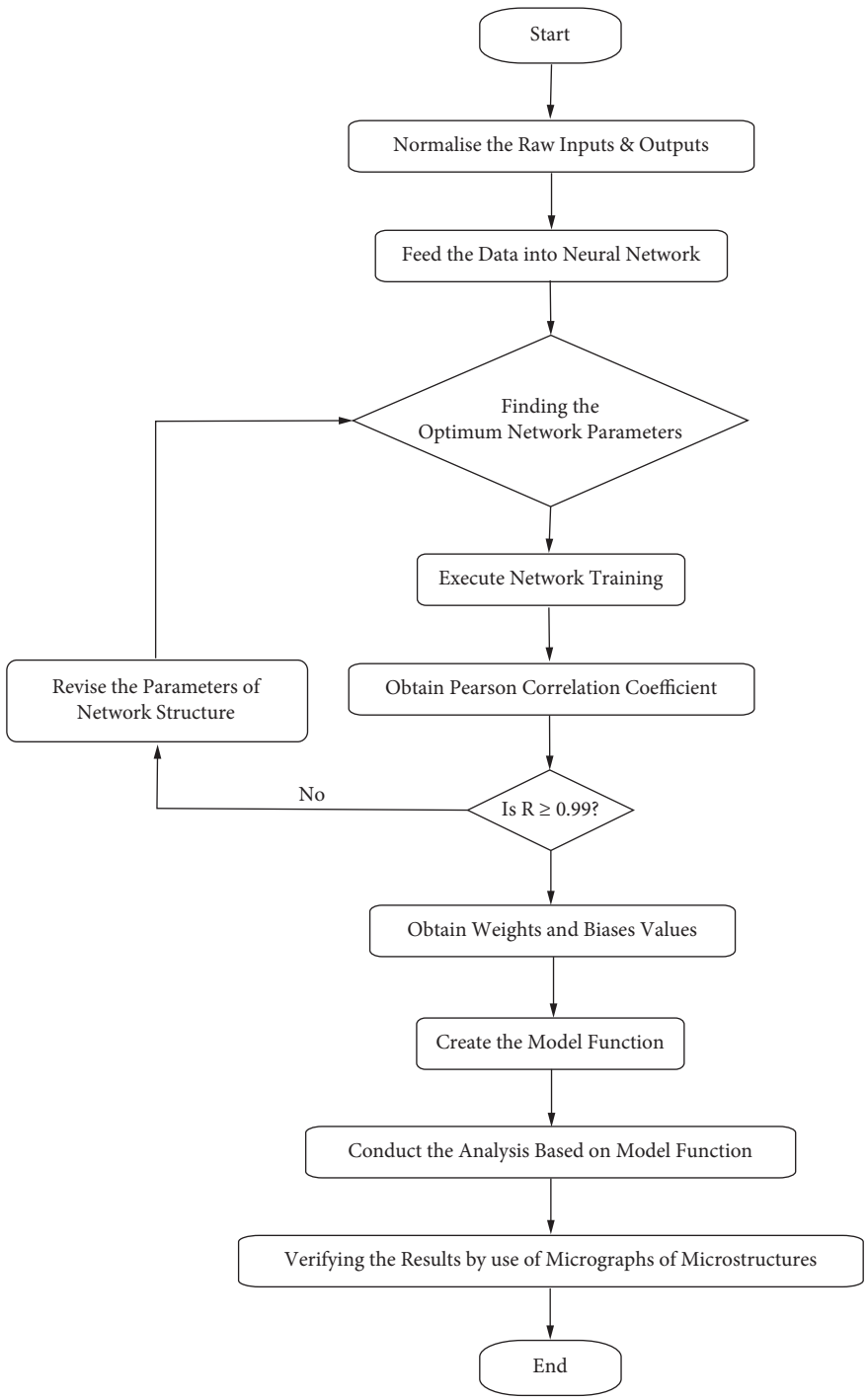

Figure 2: Network training, exploration of ANN training results, and evaluation of result composition of the technique.

Table 2: Assembly and the factors of ANN.

ANN framework	PCC	Rate of learning	Number of epochs	Mean error (%)
$3 \times 8 \times 2$	0.9991	0.094	150000	0.096

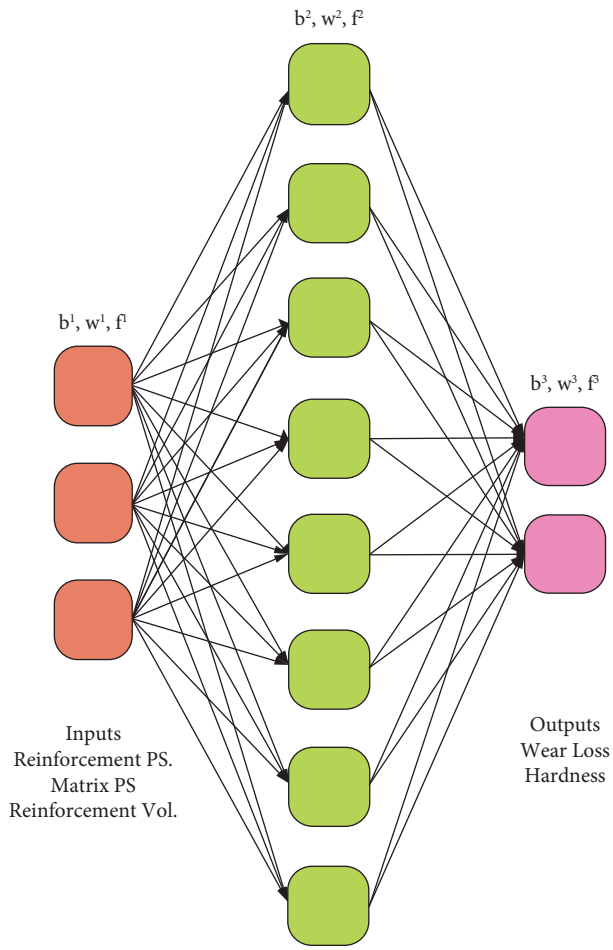

Figure 3: Framework of the functional ANN.

$$\begin{aligned} a^1 &= f^1\left(W^1 p + b^1\right), \\ a^2 &= f^2\left(W^2 a^1 + b^2\right), \\ a^3 &= f^3\left(W^3 a^2 + b^3\right), \\ G(g(1), g(2)) = a^3 &= f^3\left(W^3 f^2\left(W^2 f^1\left(W^1 p + b^1\right) + b^2\right) + b^3\right), \end{aligned} \tag{1}$$

a^3 is the output of the third layer, which is equivalent to the function G ($g(1)$, $g(2)$), and a^1 and a^2 are the outputs of the first and second layers, respectively. $G(g(1)$ and $g(2))$ are the resultant factors for measured values. Ms, Rs is used in the function G to calculate wear loss and hardness.

4. Results and Discussions

4.1. Artificial Neural Network. For wear loss as well as hardness, as can be shown in Figures 4(a) and 4(b), the ANN predictions are close to the experimental results. The ANN model has a 1% margin of error for making predictions (Table 2). This means that the projected findings agree well with the experimented data. The results show that an artificial neural network is a valuable tool for predicting the wear behavior of particle-strengthened MMCs and can be utilized in conjunction with experimental results.

4.2. Analysis of Microstructure. Figure 5 shows the optical microstructures of AA5052-B_4Cp MMCs. Microscopically, 8% volume fraction composites have a homogeneous distribution of reinforcing particles (Figures 5(a) and 5(b)). In these composites, the reinforcement (Rs) and the matrix (Ms) particle size ratio is more than one or equal to 1. While the reinforcement volume percentage is less, Figure 5(c) shows that few particle clusters arise in the microstructure when the reinforcement size is lesser than the matrix size of the particle (Rs/Ms < 1) (8%). However, particle clusters are more numerous in composites with a large volume fraction

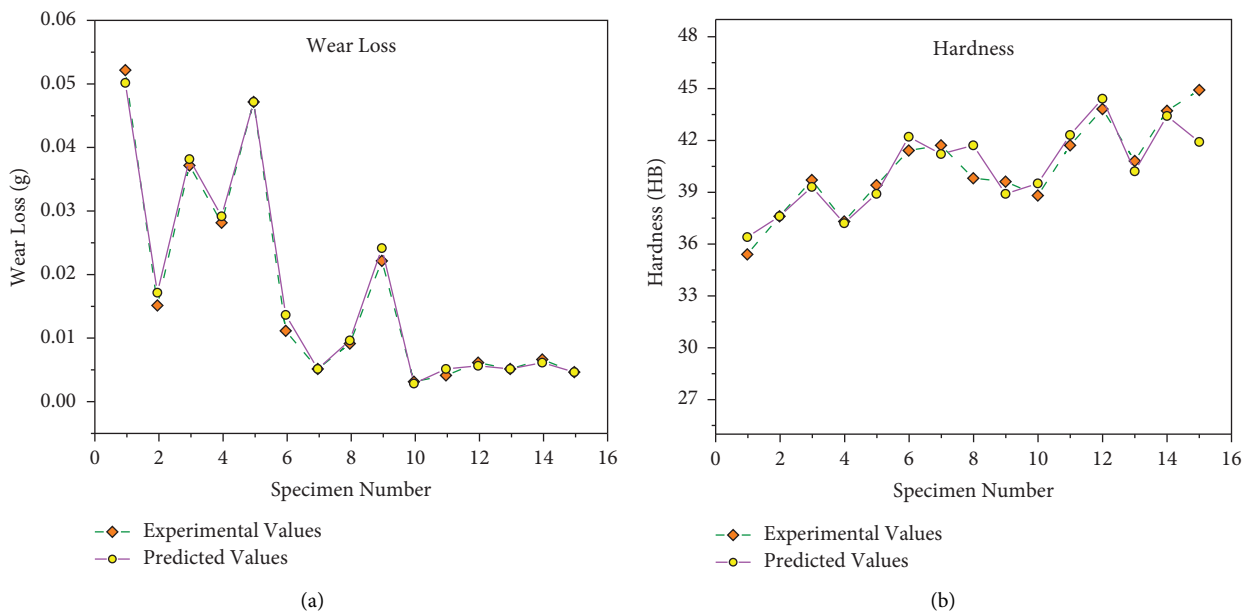

Figure 4: Evaluation of the experimented values and theoretical values (a) wear loss and (b) hardness.

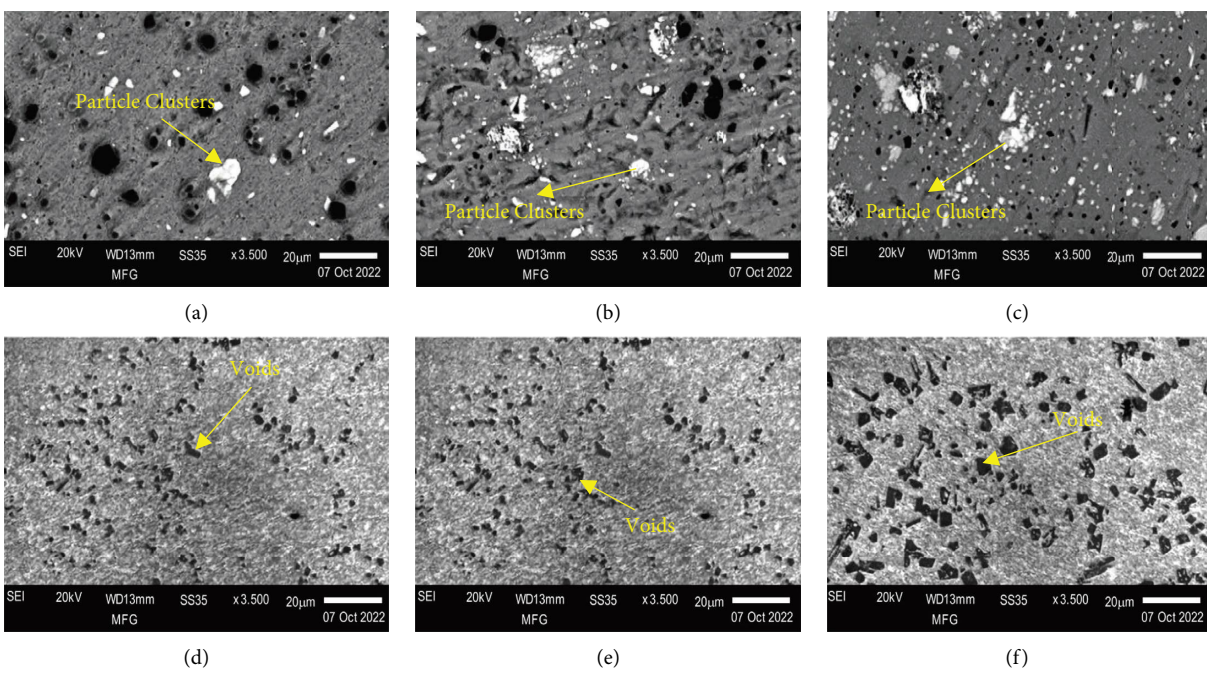

Figure 5: Microstructure images of AA5052-B_4Cp MMCs: (a) 8% AA5052/95-B_4C/145; (b) 8% AA5052/95-B_4C/95; (c) 8% AA5052/95-B_4C/95; (d) 18% AA5052/95-B_4C/145; (e) 18% AA5052/95-B_4C-95; (f) 18% AA5052/145-B_4C/95.

(18%), which is true regardless of the Rs/Ms (Figures 5(d)–5(f)). This research determined the clustering rate of reinforcement particles by comparing the cluster area to the total microstructure area. Seven micrographs were obtained from each sample, the parameter value was determined for each, and the average was used to determine the clustering rate. Comparing only specimens with 18% of reinforcement reveals that the clustering of strengthening particles becomes less severe with an increasing Rs/Ms ratio.

It can also be seen clearly from Table 1 and Figure 5 that when the volume proportion rises and the Rs/Ms ratio falls, the degree of reinforcement particle clustering increases. These findings suggest that reinforcement particles' distribution and cluster formation are controlled by the Rs/Ms ratio in addition to the volume fraction. The dashed arrows represent particle clusters with space in Figure 5. There are two distinct ways these gaps can emerge. Inefficient bonding between the groups of reinforcement particles makes them

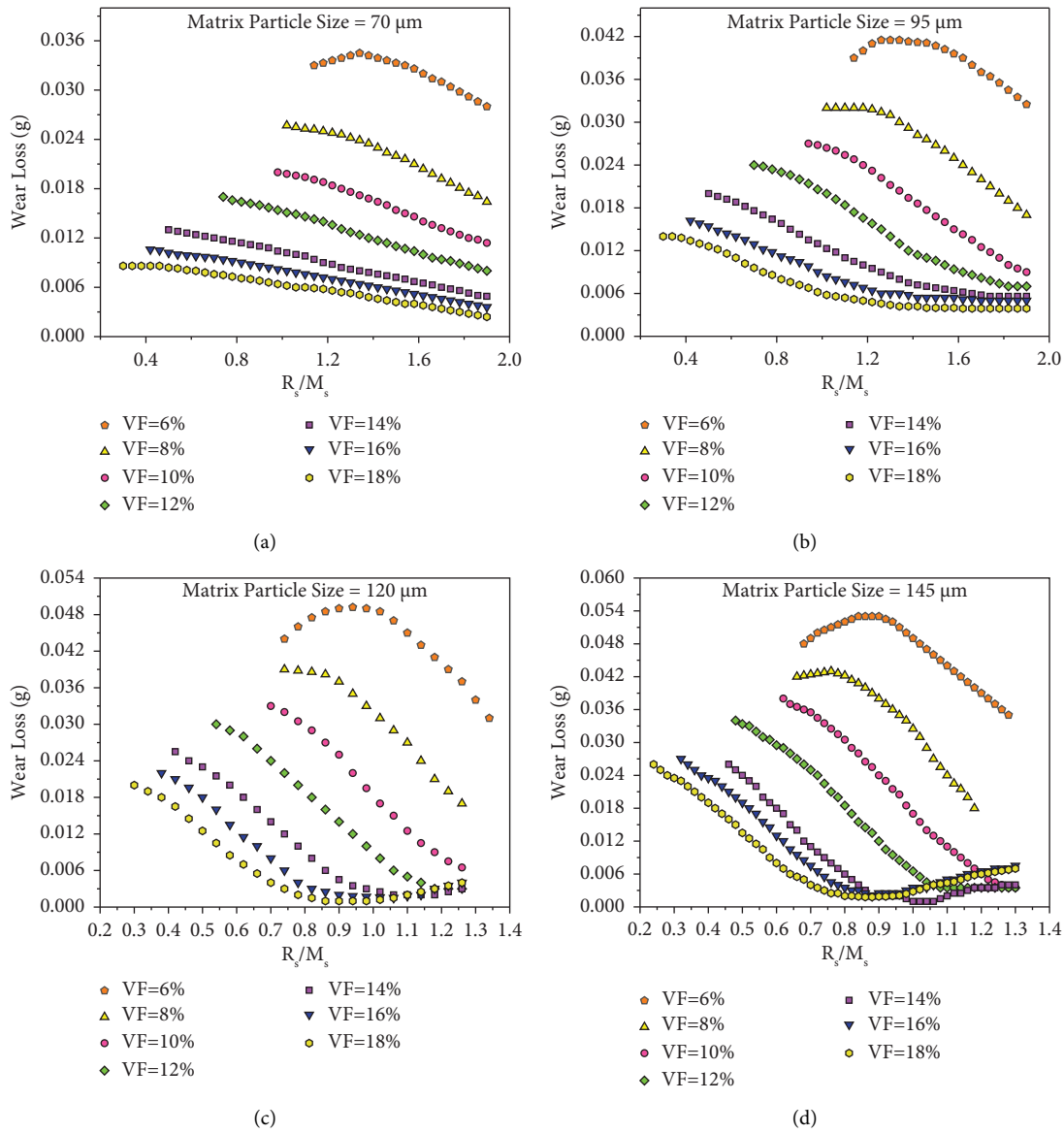

Figure 6: Predicted wear loss for various matrix particle sizes (a) 70 μm, (b) 95 μm, (c) 120 μm, and (d) 145 μm.

easy to dislodge or remove from the matrix. In this case, sliding wear tests have not yet been conducted. Second, when deformed plastically, the matrix material has difficulty filling the gaps between the reinforcement particles. This is because the reinforcing particles are clustered too closely together, which impedes the flow of the matrix material during the pressing and sintering processes. It explains how the reinforcement particle clustering affects the AA5052/B_4Cp MMCs' wear behavior.

4.3. Wear Behavior. Figure 6 shows that AA5052/B_4Cp composites' wear behavior is affected by reinforcement volume percentage and the Rs/Ms factors. The percentage of reinforcement volume in a material's total volume is essential in determining its wear resistance. As the volume fraction of reinforcement rises, wear loss falls. However, as seen in Figures 6(a)–6(d), wear loss rises with the increasing matrix size of the particle. The impact of particle size reinforcement on wear resistance is complex and cannot be analyzed in isolation. Once the strengthening volume percentage is more significant than 12% and the Rs is less than half that of the Ms (Rs/Ms 0.5), the wear loss appears to decrease slightly. However, wear loss starts to diminish as the relative Rs increases drastically. There is a minimum in the wear loss's lowering trend at high reinforcement volume fraction and Rs, which then starts to climb again. The wear behavior of AA5052/B_4Cp MMCs can be better examined and comprehended if a second parameter is defined to account for the size of the reinforcement particles. This study developed a new metric, Rs/Ms, to accomplish this.

The model function (Figure 6, Table 1) and experimented data show wear loss reductions as the ratio of Rs and Ms increases. Previously established, this ratio demonstrates

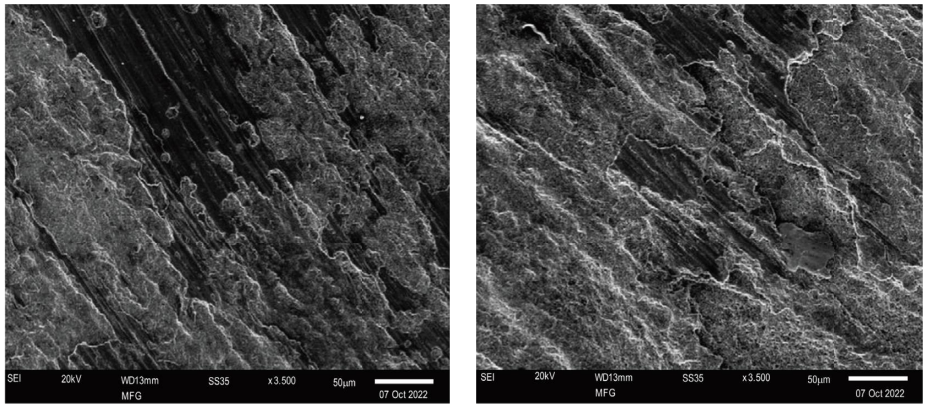

(a) (b)

Figure 7: SEM morphologies of worn surfaces of (a) 8% AA5052/145-B_4C95 μm and (b) 18% AA5052/145-B_4C/145 μm.

how many reinforcement particles there are for every hundred matrix particles [26]. As the mixture is stirred, the smaller matrix particles can more effectively fill the spaces between the larger reinforcement particles. Wear resistance improves as the ratio of Rs/Ms increases. With just two exceptions, wear loss reduces with increasing Rs/Ms. In the first scenario, the volume fraction is between 6 and 8%. As shown in Figure 6, the wear rate decreases after reaching a maximum. In this second scenario, the volume percentage of reinforcement is more than 14%, the reinforcement and matrix particle size proportion is close to 1, and the matrix particle size is more than 120 μm. When the particle size of the matrix increases, the wear loss falls until a minimum is attained, and then the minimum moves to a lesser range of the ratio of Rs and Ms (Figures 6(c) and 6(d)).

Figure 7(a) demonstrates that the reinforcement particles cannot prevent substantial plastic distortion in the first situation, while the sample surface is in metal-metal contact when the testing load is relatively high. Larger reinforcement particles induce extensive plastic deformation and wear loss, which may be attributed to their poorer strength due to harboring more defects, as observed by authors [27, 28]. In addition, low Rs/Ms can cause particle clusters, resulting in a significant amount of wear loss. But after wear loss has plateaued at a given reinforcing particle size, further increases in particle size reduce the rate of wear (Figure 6). Because larger reinforcement particles are lodged so profoundly in the matrix, they are better able to shield the matrix from damage and hence prevent the plastic distortion of the specimen's surface.

As shown in Figure 5, the volume proportion of reinforcement particles and the number of particle clusters raise the reinforcement and matrix size particle ratio to a specific fixed maximum value of volume percentage. Authors [29–31] conducted a few other study teams that have come to similar conclusions. Wear loss decreases initially despite an increase in Rs/Ms in another case when the percentage volume of reinforcement is more significant than 14% and the Ms is > 120 μm (Figures 6(c) and 6(d)). A maximum volume proportion of reinforcement (>14%) is responsible for the

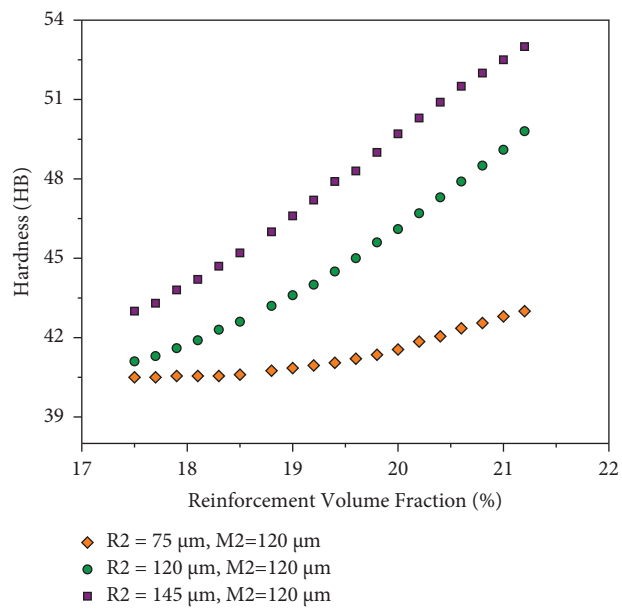

Figure 8: Composites with varied Rs/Ms ratios with varying hardness.

observed upward trend in wear loss. The minimum process temperature of the MMC prevents diffusion between the B_4C and AA5052 particles, resulting in weak bonding in the clustered particles that make up the microstructure of MMCs [32, 33]. Because of this, particles are easily knocked off the sample's surfaces during the wear test [34]. The spaces left behind by considerable dislodged particles are not always filled. Depending on the particle cluster, the voids created in the present investigation may be noticed in Figure 5 well before the wear test was performed. As shown in Figure 7(b), the wear loss increases because the dislodged particles become imprisoned among the sample surface and counter-face, breaking apart (Figures 6(c) and 6(d)). When the percentage volume of reinforcement (14%) and the percentage volume of the matrix (120 μm) are both high, the high Rs/Ms cannot improve the wear resistance of MMCs.

4.4. Hardness. Hardness increases with increasing volume fraction, as demonstrated by investigations by the authors [35–37]. Dislodging and fracturing of reinforcing particles diminish wear resistance, as seen in Figure 8. In contrast to the wear loss trends, which show an increase as a function of rising volume fraction, it is clear that hardness improves for all ranges of Rs/Ms. This suggests an inverse relationship between hardness and wear resistance in this region.

5. Conclusions

Using a numerical model derived from a trained ANN, this research examined the wear resistance as well as hardness of AA5052/B_4Cp metal matrix composites and found the following:

(1) Percentage volume of reinforcement, followed by the ratio of particle size reinforcement to particle size matrix, is the essential factor in defining the wear resistance of AA5052/B_4Cp MMCs, and more accurate results can be obtained

(2) Except in two situations, wear resistance improves with an increase in the Rs/Ms ratio: for (a), the reinforcement volume fraction must be less than 8%. Here, (a) the percentage volume is greater than 14%, (b) the Rs/Ms is close to 1, and (c) the Ms is more significant than 120 μm; wear loss diminishes as the Rs/Ms ratio increases. The lost wear reduces until it reaches a minimum and then rises again.

(3) Reinforcing particle clustering has a significant impact on wear loss. The wear resistance goes down with the number of clusters. The proportion of reinforcement volume to particle volume and the strengthening stiffness to particle stiffness are essential factors in particle clustering. Wear resistance is inversely proportional to the Rs/Ms ratio, which means that raising the volume percentage increases the particle clustering.

(4) The reinforcement particles become dislodged and break when the volume percentage of reinforcement is high (14%) and when the particle sizes of both the reinforcement and the matrix are significant (120 μm). The material's wear resistance is decreased because these fragmented particles can be readily cleaned off the surface. Here, increasing the volume fraction results in a greater hardness across the board for all Rs/Ms values; hence, composites with lower reinforcement volume percentages exhibit more excellent wear resistance. There is no correlation between wear resistance and hardness.

(5) Through the use of a qualified ANN, the wear behavior of particle-reinforced metal matrix composites was successfully characterized for the first time. The network took as input parameters the particle size and volume fraction of the reinforcement in the matrix, and the network output factors were the wear loss and hardness of the composite.

Data Availability

All data supporting the findings of this study are included within the manuscript.

Ethical Approval

All procedures performed in this study involving human participants were by the ethical standards of the institutional and/or national research committee and its later amendments or comparable ethical standards.

Disclosure

The funders had no role in the study design, data collection, and analysis, publication decision, or manuscript preparation.

Conflicts of Interest

The authors declare that they have no conflicts of interest.

References

[1] M. Patel, M. K. Singh, and S. K. Sahu, "Abrasive wear behaviour of sand cast B4C particulate reinforced AA5052 metal matrix composite," in *Innovative Product Design and Intelligent Manufacturing Systems*, B. Deepak, D. Parhi, and P. Jena, Eds., Springer, Singapore, pp. 359–369, 2020.

[2] Q. T. Pham, "A machine learning–based methodology for identification of the plastic flow in aluminum sheets during incremental sheet forming processes," *International Journal of Advanced Manufacturing Technology*, vol. 120, no. 5–6, pp. 3559–3584, 2022.

[3] B. Girinath and N. S. Shanmugam, "A modified version of MATLAB application window for predicting the weld bead profile and stress–strain plot of AA5052 CMT weldment using ER4043," *Simulation*, vol. 98, no. 3, pp. 221–234, 2022.

[4] A. Mulay, B. S. Ben, S. Ismail, and A. Kocanda, "Prediction of average surface roughness and formability in single point incremental forming using artificial neural network," *Archives of Civil and Mechanical Engineering*, vol. 19, no. 4, pp. 1135–1149, 2019.

[5] S. S. Panicker, K. S. Prasad, S. Basak, and S. K. Panda, "Constitutive behavior and deep drawability of three aluminum alloys under different temperatures and deformation speeds," *Journal of Materials Engineering and Performance*, vol. 26, no. 8, pp. 3954–3969, 2017.

[6] B. N. Guniputi, P. R. T, and V. K. Mamidi, "Effect of in-situ reaction time on the strength of AA5052/ZrAl3 metal matrix nanocomposites," *Advances in Materials and Processing Technologies*, pp. 1–12, 2022.

[7] Z. J. Kadhim, H. J. M. Alalkawi, and A. H. Reja, "Evaluation the magnetic and microstructure properties of Al/TiO2nanocomposites using various stir casting temperature," *Journal of Physics: Conference Series*, vol. 1973, no. 1, Article ID 012115, 2021.

[8] F. Khodabakhshi, M. Nosko, and A. P. Gerlich, "Effects of graphene nano-platelets (GNPs) on the microstructural characteristics and textural development of an Al-Mg alloy during friction-stir processing," *Surface and Coatings Technology*, vol. 335, pp. 288–305, 2018.

[9] F. Khodabakhshi, S. M. Arab, P. Švec, and A. P. Gerlich, "Fabrication of a new Al-Mg/graphene nanocomposite by multi-pass friction-stir processing: dispersion, microstructure, stability, and strengthening," *Materials Characterization*, vol. 132, pp. 92–107, 2017.

[10] M. Bodaghi and K. Dehghani, "Friction stir welding of AA5052: the effects of SiC nano-particles addition," *International Journal of Advanced Manufacturing Technology*, vol. 88, no. 9–12, pp. 2651–2660, 2017.

[11] F. Khodabakhshi, A. Simchi, A. H. Kokabi, and A. P. Gerlich, "Friction stir processing of an aluminum-magnesium alloy with pre-placing elemental titanium powder: in-situ formation of an Al3Ti-reinforced nanocomposite and materials characterization," *Materials Characterization*, vol. 108, pp. 102–114, 2015.

[12] B. N. Sharath, C. V. Venkatesh, A. Afzal et al., "Multi ceramic particles inclusion in the Aluminium matrix and wear characterization through experimental and response surface-artificial neural networks," *Materials*, vol. 14, pp. 2895–2911, 2021.

[13] B. N. Sharath, C. Venkatesh, A. Afzal, M. Ahmed Ali Baig, and A. Praveen Kumar, "Study on effect of ceramics on dry sliding wear behaviour of Al-Cu-Mg based metal matrix composite at different temperature," *Materials Today: Proceedings*, vol. 46, pp. 8723–8733, 2021.

[14] K. Trinath, R. Aepuru, A. Biswas, M. Ramalinga Viswanathan, and R. Manu, "Study of self-lubrication property of Al/SiC/Graphite hybrid composite during Machining by using artificial neural networks (ANN)," *Materials Today: Proceedings*, vol. 44, pp. 3881–3887, 2021.

[15] V. Jagota and R. K. Sharma, "Wear volume prediction of AISI H13 die steel using response surface methodology and artificial neural network," *Journal of Mechanical Engineering and Sciences*, vol. 14, no. 2, pp. 6789–6800, 2020.

[16] T. K. Kandavel, T. Ashok Kumar, and E. Varamban, "Prediction of tribological characteristics of powder metallurgy Ti and w added low alloy steels using artificial neural network," *Indian Journal of Engineering and Materials Sciences*, vol. 27, no. 3, pp. 503–517, 2020.

[17] X. Qi, Y. Wang, C. Wang, and R. Zhang, "Microstructure and performance of nano-WC particle-strengthened Ni coatings by electro-brush plating," *Journal of Materials Engineering and Performance*, vol. 27, no. 11, pp. 6069–6079, 2018.

[18] F. B. Marin, M. Marin, G. Gurău, C. Gurău, and A. Petrică, "Application of an artificial neural network for prediction of the wear resistance of sintered iron alloys," *SGEM International Multidisciplinary Scientific GeoConference EXPO Proceedings*, vol. 18, no. 1, pp. 55–60, 2018.

[19] S. Kim, J. Hong, Y. Joo, and M. Kang, "Synergistic effect of SiC nano-reinforcement and vibrator assistance in micro-friction stir welding of dissimilar AA5052-H32/AA6061-T6," *Journal of Manufacturing Processes*, vol. 82, pp. 860–869, 2022.

[20] N. A. Liyakat and D. Veeman, "Improvement of mechanical and microstructural properties of AA 5052-H32 TIG weldment using friction stir processing approach," *Journal of Materials Research and Technology*, vol. 19, pp. 332–344, 2022.

[21] P. Samal, P. R. Vundavilli, A. Meher, and M. M. Mahapatra, "Reinforcing effect of multi-walled carbon nanotubes on microstructure and mechanical behavior of AA5052 composites assisted by in-situ TiC particles," *Ceramics International*, vol. 48, no. 6, pp. 8245–8257, 2022.

[22] J.-W. Choi, W. Li, K. Ushioda, M. Yamamoto, and H. Fujii, "Microstructure evolution and hardness distribution of linear friction welded AA5052-H34 joint and AA5083-O joint," *Journal of Materials Research and Technology*, vol. 17, pp. 2419–2430, 2022.

[23] J. Sarvaiya and D. Singh, "Influence of hybrid pin profile on enhancing microstructure and mechanical properties of AA5052/SiC surface composites fabricated via friction stir processing," *Canadian Metallurgical Quarterly*, pp. 1–14, 2022.

[24] J. T. Chinna Rao, V. Harikiran, K. S. S. Gurudatta, and M. V. D. Kumar Raju, "Temperature and strain distribution during friction stir welding of AA6061 and AA5052 aluminum alloy using deform 3D," *Materials Today: Proceedings*, vol. 59, pp. 576–582, 2022.

[25] S. H. Jo, B. B. Park, and S. H. Lee, "Microstructure and mechanical properties of cold roll-bonded layered aa6061/aa5052/aa6061/aa5052 aluminum alloy sheet," *Korean Journal of Materials Research*, vol. 32, no. 3, pp. 161–167, 2022.

[26] S.-H. Jo and S.-H. Lee, "Microstructural evolution of a cold roll-bonded multi-layer complex aluminum sheet with annealing," *Korean Journal of Materials Research*, vol. 32, no. 2, pp. 72–79, 2022.

[27] P. K. Arya, N. K. Jain, and M. Jayaprakash, "Optimization of process parameters for friction stir welding of Aluminium alloy AA5052-H32 by using taguchi method," *Springer Proceedings in Materials*, vol. 12, pp. 71–81, 2022.

[28] X.-Q. Ren, C. Chen, X.-K. Ran, Y.-X. Li, and X.-G. Zhang, "Microstructure evolution of AA5052 joint failure process and mechanical performance after reconditioning with tubular rivet," *Transactions of Nonferrous Metals Society of China*, vol. 31, no. 11, pp. 3380–3393, 2021.

[29] A. Rajesh Kannan, S. Mohan Kumar, R. Pramod, N. Siva Shanmugam, Y. Palguna, and M. Vishnukumar, "Microstructure and mechanical properties of dissimilar aluminum alloys AA5052-H32 and aa2219-T31 welded using cold metal transfer process," *Materials Performance and Characterization*, vol. 10, no. 1, pp. 20210043–20210657, 2021.

[30] Y. Sai Ratnakar, P. Srinivasa Reddy, M. Gangadhar Rao, and D. Appanna, "Experimental investigation and optimization on microstructure & mechanical properties of AA5052 in comparison with AA2024 and AA8090 using friction stir welding," *International Journal of Performability Engineering*, vol. 17, no. 8, pp. 686–694, 2021.

[31] Z. Chang, M. Yang, and J. Chen, "Experimental investigations on deformation characteristics in microstructure level during incremental forming of AA5052 sheet," *Journal of Materials Processing Technology*, vol. 291, Article ID 117006, 2021.

[32] B. M. Nagarajan and M. Manoharan, "Influence of cooling conditions on tensile lap shear strength and microstructure of friction stir welded aluminum alloy 5052-H32 and polycarbonate light weight hybrid joint," *Journal of Manufacturing Processes*, vol. 82, pp. 390–402, 2022.

[33] L. Song, Z. Xie, H. Gao, C. Kong, and H. Yu, "Microstructure and mechanical properties of ARB-processed AA1050/AA5052 multi-layer laminate sheets during cryorolling," *Materials Letters*, vol. 307, Article ID 130998, 2022.

[34] J. Das, P. S. Robi, and P. K. Sahu, "Influence of process parameters on mechanical and microstructural properties of friction stir welded AA5052," *Advances in Materials and Processing Technologies*, pp. 1–17, 2022.

[35] H. Zhou, P. Yao, Y. Xiao et al., "High energy braking behaviors and tribo-map constructions of Cu metal matrix composites with different Cr volume contents," *Wear*, vol. 496–497, Article ID 204275, 2022.

[36] A. B. Kheradmand, M. R. Fattahi, M. Tayebi, and B. Hamawandi, "Tribological characterization of reinforced Fe matrix composites with hybrid reinforcement of C, Cu, and SiC particulates," *Crystals*, vol. 12, no. 5, p. 598, 2022.

[37] S. S. Kumar, S. D. Kumar, U. Magarajan, and S. Divya, "Study of mechanical and wear behaviour of AA5083 graphene reinforced composites," *Kovove Materialy-Metallic Materials*, vol. 60, no. 2, pp. 121–129, 2022.